# FABRICATION AND CHARACTERIZATION OF METAL OXIDE NANOPARTICLES BY ARC-DISCHARGE IN WATER

Thesis submitted in accordance with the requirements of the
University of Liverpool for the degree of Doctor in Philosophy

by

Dimitrios Delaportas

September 2011

*To my parents*

*Ioannis and Maria Delaportas*

*And to my brother*

*George Delaportas*

*Στους γονείς μου*

*Ιωάννη και Μαρία Δελαπόρτα*

*Και στον αδερφό μου*

*Γιώργο Δελαπόρτα*

# *Acknowledgments*

*I would like to offer my sincere thanks to my supervisor Dr. I. Alexandrou who introduced me to the world of science. I was very lucky to be supervised by a man who really cared about our work. In addition, a huge thank you has to be devoted to Professor S. Hall who welcomed me to his group and guided me every time it was needed.*

*A major part of the experimental work was carried out in the Material Science Department in the University of Liverpool and Cambridge and in King's Abdullah University of Science and Technology. Their hospitality enabled me to get important data for this study.*

*Last, but not least, I offer, from the bottom of my heart, my thanks to my family, who are extremely supportive, emotionally and financially, to any decisions I make.*

## *Publications*

• "Variant shape growth of nanoparticles of metallic Fe–Pt, Fe–Pd and Fe–Pt–Pd alloys" D. Ung , L. D. Tung, G. Caruntu, D. Delaportas, I. Alexandrou, I. A. Prior and N. T. K. Thanh, Cryst. Eng. Comm. 11, 7, p. 1309-1316 (2009).

• "Monitoring Charge Exchange in P3HT-Nanotube Composites Using Optical and Electrical Characterisation" I. Alexandrou, E. Lioudakis, D. Delaportas, C. Z. Zhao, A. Othonos, Nanoscale Res Lett. 4, 7, p. 635-639 (2009).

• "$\gamma$-$Al_2O_3$ nanoparticle production by arc-discharge in water: in situ discharge characterization and nanoparticle investigation" D. Delaportas, P. Svarnas, I. Alexandrou, A. Siokou, K. Black and J. W. Bradley, J. Phys. D: Appl. Phys. 42, 24 (2009).

• "$Ta_2O_5$ Crystalline Nanoparticle Synthesis by DC Anodic Arc in Water", D. Delaportas, P. Svarnas, and I. Alexandrou, J Electrochem Soc. 157, 6, p. K138-K143 (2010).

• "$CuO/Ta_2O_5$ core/shell nanoparticles produced by arc-discharge in water" D. Delaportas, P. Svannas, I. Alexandrou, S. N. Georga, C. A. Krontiras, N. I. Xanthopoulos, A. Siokou, P. R. Chalker, Mater. Lett. 65, 15-16, p. 2337-2340 (2011).

• "Plasma of arc-discharge in water for the formation of diverse nanostructures dependent on the anode material", D. Delaportas, P. Svarnas, I. Alexandrou, and S. Hall, IEEE Trans. Plasma Sci. 39, 11, p. 2628 (2011).

## *Conferences:*

• D. Delaportas, P. Aden, C. Muckle, S Yeates, R. Treutlein, S Haq and I. Alexandrou (2007) "Cross section high resolution imaging of polymer-based materials". Microscopy of Semiconducting Materials, Churchill College, Cambridge (UK) Institute of Physics.

• D. Delaportas, P. Svarnas and I. Alexandrou (2008) "Fabrication of high-k dielectric nanoparticles using the arc-discharge method", Nanoparticles 2008: Synthesis, properties and applications of nanoparticles, Bradford (UK).

• D. Delaportas, P. Svarnas, J. W. Bradley and I.Alexandrou (2009) "Arc Discharge in Water for Dielectric Nanoparticle Production". XXIX International conference on Phenomena in ionized gases Cancun (Mexico)

• D. Delaportas, S. Haq and I. Alexandrou (2009) "$Al_2O_3$ and $Ta_2O_5$ nanoparticle production by arc-discharge in water for flexible dielectrics". Nanoparticles 2009: Synthesis, properties and applications of nanoparticles, Liverpool (UK).

• D. Delaportas, P.K. Karahaliou, N.I. Xanthopoulos, P. Svarnas, S.N. Georga, C.A. Krontiras, I. Alexandrou (2011) "Broadband Dielectric Spectroscopy Response of $CuO/Ta_2O_5$ Core-shell Nanoparticles" 3rd International Conference from Nanoparticles and Nanomaterials to Nanodevices and Nanosystems (IC4N 2011), Hersonissos, Crete. (Oral Presentation) (GR).

• P. K. Karahaliou, N.I. Xanthopoulos, D. Delaportas, P. Svarnas, S.N. Georga, C.A. Krontiras, I. Alexandrou (2011) "Dielectric Behavior of $CuO/Ta_2O_5$ Core/Shell Nanoparticles Produced by Arc-discharge in Water" Panhellenic Conference on Solid State Physics and Materials Science (CY)

# *ABSTRACT*

***Author*: Dimitrios Delaportas**

## *Thesis title*: Fabrication and characterization on metal oxide nanoparticles by arc discharge in water.

The aim of this project was to establish the arc discharge in water method as a valid method of producing metal oxide nanoparticles (NPs) with dielectric properties. A vertical arc discharge system was designed and fabricated and several diagnostic tools were attached to the system in order to monitor in situ the propagation of the plasma. Electrical measurements, high speed imaging, optical emission spectroscopy and electrode mass reduction measurements were employed to three different anode materials; aluminum and tantalum rods as well as a mixture of copper-tantalum compressed powder grains. The cathode of the DC arc was in all cases was a carbon rod. The product of the discharge was collected in powder form and examined by means of electron microscopy, x-ray diffraction (XRD), x-ray photoelectron spectroscopy (XPS) and broadband dielectric spectroscopy (BDS).

The experiments showed that, during discharge, the physical processes occurring between the electrodes, force the anode material to evaporate in the atomic level. While atomization takes place, the water molecules surrounding the plasma region gets vaporized due to the localized high temperature resulting in the division of oxygen and hydrogen atoms. Metal and oxygen atoms bond, becoming the seeds for nanoparticle formation. The particle growth stops when quenching occurs due to the continuous condensation and expansion of the plasma.

High-Resolution Transmission Electron Microscopy (HR-TEM) examination revealed that spherical crystalline nanoparticles are formed, with an average size of 40 nm when using either aluminum or tantalum rod. XRD and XPS analyses concluded that high purity $Al_2O_3$ and $Ta_2O_5$ NPs are produced by using the arc discharge method respectively. HR-TEM was also employed to the nano-product of the composite anode showing a peculiar core-shell NP structure (mean size 20 nm). Scanning Transmission Electron Microscopy (STEM) was used in High Angle Annular Dark Field (HAADF) imaging and Energy Dispersive X-ray Spectroscopy (EDX) modes to identify the atomic arrangement resulting in the formation of an oxidized copper core with an oxidized tantalum shell. The nano-powder was tested via BDS showing a capacitive behavior.

Throughout this work it was been proven that arc discharge in water is a cost-effective and easy to implement method of preparing dielectric NPs. A methodology for studying both the process as well as the product has been described. High purity $Al_2O_3$ and $Ta_2O_5$ have been successfully produced. CuO-$Ta_2O_5$ core-shell NPs were synthesized for the first time and were characterized structurally and electrically. Adjustments in order to improve the efficiency of the system were proposed and new ideas for the formation of composite metal oxides have emerged.

# 1. INTRODUCTION

## 1.1. NANOTECHNOLOGY

Nowadays, the technological advances are so rapid that the need for new nano-materials with enhanced properties has become a necessity. Since 1959, when for the first time the term "nanotechnology" was mentioned by Richard Phillips Feynman, scientists have invested both funds and time on exploring new ways to produce electronic building blocks in the nanoscale region.

Nanotechnology is defined as the study of controlling matter at an atomic/molecular scale, dealing with structures, either materials or devices, below 100 nanometres (nm). Structures that have one or more dimensions in the order of 100 nm or less are called nanoparticles (NPs) and usually differentiate from the bulk material in terms of material properties. Several different shapes have been fabricated such as spheres [1], tubes [2], cubes [3], octopod-cubes [3], rods [3, 4], horns [5], wires [1] etc. all to serve different applications and needs.

## 1.2. NANOPARTICLE APPLICATIONS

Currently, the use of NPs in many technological applications such as biology and electronic devices is widespread. Scientists around the globe are putting a lot of effort into creating, or sometimes altering the size, shape and chemical composition of NPs to give them desirable properties. The two main fields in which nanotechnology finds greatest interest are biology and electronics. A few recent advances in these two fields, of relevance to the work of the thesis, are presented below.

### 1.2.1. NANOPARTICLES IN BIOLOGY

Drug Delivery Systems (DDS), gene therapy, biodetection, cancer treatment, medical imaging probe design, and biosensors are just a few applications that have drawn the attention of many research groups.

The formation of core-shell NPs consisting of silica as an outer layer and a magnetic core was reported by a research group from China in collaboration with the

University of Florida in 2004 [6]. These particles were highly luminescent and photo-stable and as a result, were considered to be prime candidates for biosensors and biomarkers. Since silica NPs are easily modified by many bio-molecules for added biochemical functionality, the versatility of the silica surface was used to immobilize various functional groups as needed for biosensor work. The group demonstrated the biochemical modification of silica based NPs. Both pure and dye-doped silica NPs were prepared and their surfaces were modified with enzymes and biocompatible chemical reagents that allowed them to function as biosensors and biomarkers.

NPs were shown to be ideal for bio-conjugation with bio-molecules such as antibody for cellular membrane binding and imaging. In the new imaging method based on bio-conjugated NPs, each NP encapsulates tens of thousands of fluorescent dye molecules in a protective silica matrix, providing highly amplified and reproducible signal for fluorescence-based bacterium bioassays. Compared to a conventional immunoassay, where an antibody–antigen binding event brings only a few dye molecules for signaling, the bio-conjugated NPs enabled significant amplification of the analytical signal because of the many dye molecules inside each NP. The use of the NPs for bio-marking applications was demonstrated to recognise leukemia cells using mouse human antibody using CD10 surface modified NPs. The control experiments with bare Rubpy-doped NPs did not show any labeling of the cells. A method that allows bio-conjugation of highly stable luminophores was demonstrated by doping metallorganic molecules in a silica matrix. By taking advantage of surface modification chemistry available for silica, the resulting NPs were modified and immobilized with antibodies for bio-marking applications. The particles were highly stable and effective in the recognition process.

In 2005, Neuberger et al. used superparamagnetic iron oxide nanoparticles as a contrast agent in magnetic resonance imaging (MRI), for tumor therapy and cardiovascular disease [7]. Based on the NP properties, they studied the following systems: distribution of radioactivity within different tissues using a special indicator for Feisotopes, the relaxation time of liver and spleen in MRI, the capability to treat a previously induced iron deficit anemia, pathology of several organ systems by means of histology, chem.-screen of blood and urine and the mutagenicity by means of a special test. Even though their use was considered experimental, except in MRI, new

technologies for particle synthesis, coating and functionalisation will render them even more attractive for all kinds of medical applications in the near future.

Carbon Nanotubes (CNTs), a tube-like structure that results from a special arrangement of carbon atoms [8] is a great example of nanoparticles that has been widely studied for biological applications. Since the year 2000 there has been a significant increase of CNT publications as shown in Figure 1-1, where scientists are trying to explore and exploit the unique electrical and physical properties of CNTs [9]. Cell tracking and labeling, sensing cellular behavior, augmenting cellular behavior and enhancing tissues matrices are four areas where nanotubes have been examined and used.

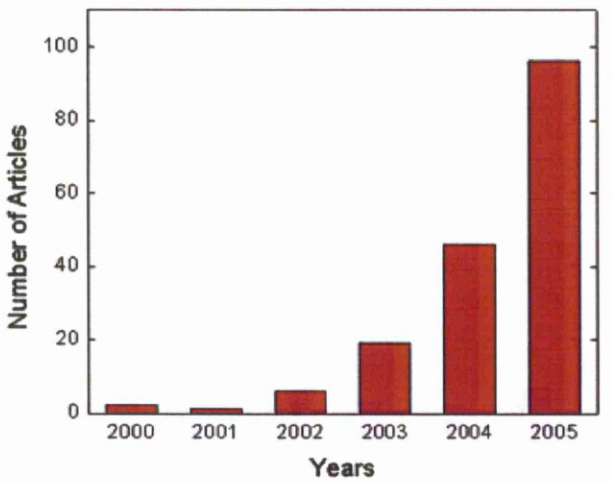


*Figure 1-1: Number of articles per year published regarding carbon nanotubes for biomedical applications[8].*

Raman spectroscopy was used in the study of optical labeling, whereby nucleic-acid encapsulated SWNTs were shown to be stable for weeks when ingested by 3T3 fibroblasts and murine myoblast stem cells [10]. The nanotubes remained in the cells during repeated cell divisions suggesting that such probes could be used for studying cell proliferation and stem-cell differentiation. The reason they remain relatively unaffected in the cell may be due to their hydrophobic nature.

Another domain where carbon nanotubes can make an impact in tissue engineering is the control of the production or delivery of tissue-inducing substances such as growth factors. Carbon nanotubes have already been used for a number of cell-altering applications including localized drug delivery [11] and transfection [12].

They have also been proposed as ion channel blockers [13]. Many of these methods take advantage of the large aspect ratio and ease of functionalisation of carbon nanotubes. Thus, carbon nanotubes could be components of drug delivery systems.

Of great importance also is the field of drug delivery systems in bio-nanotechnology research. For many biologists, it would be advantageous to create more binding sites for targeted delivery in a tumor, particularly if they are within the vascular space. Ruoslahti et al. recently constructed a system that leverages a biological cascade in-vivo to increase the available binding sites for targeted delivery [14]. Plasmonic nanomaterials, such as gold nanorods, presented exciting opportunities for such targeting combinations. These materials were metallic structures that were shown to be efficiently convert optical radiation into heat by coupling into one or more plasmon modes [15], [16]. They showed that photothermal heating mediated by tumor-targeted gold nanorods can increase binding sites for targeted delivery with thermo-sensitive drug carriers [17].

Imaging of tumors provides another good example of where the combined properties of tumor-targeted nanodevices can potentially improve the treatment of cancer patients. A tumor-targeting nanosystem that possesses both superparamagnetic and fluorescent quantum dot domains offers the possibility to provide a low resolution anatomical reference to guide surgical procedure, by magnetic resonance imaging. High resolution mapping can be visualized during surgery to identify surgical margins. They have also designed iron oxide nanoparticles [18] with improved properties and nontoxic silicon-based quantum dots for such purposes.

In conclusion, biology and nanotechnology are sharing much common ground. The increasing demand for new technologies in diagnostics and therapeutic tools leads to new developments. The unique properties of nanomaterials offer great expectations in the hands of specialists thus, a precise characterization and controlled use is essential. It is certain that several challenges remain to be overcome however; nanotechnology gives great promise to many biology and biomedical scientists for more effective and breakthrough treatments in the near future.

### 1.2.2. NANOPARTICLES IN ELECTRONICS

In the field of electronics, the three main categories of nanoparticles that draw the attention of scientists are conducting, insulating and semiconducting NPs. In this introduction, the focus is on the recent advances concerning insulating NPs and specifically, metal oxides. When a material is referred to as a high-k dielectric material that means that its dielectric constant is higher that silicon dioxide. The "k" shows the ability of a material to polarize in an electric field and it is given by the ratio of the field without the dielectric to the net filed with the dielectric. The higher the "k" the more charge can be stored and that is the reason why high-k materials are prime candidates for capacitors and gate dielectrics in transistors.

Several scientific attempts and breakthroughs from different research groups around the globe are highlighted, focusing in the fabrication and characterization of their novel materials. While research becomes more intense a wide range of applications comes in light about the usage of Organic Thin-Film Transistors (OTFTs). Flexible displays [19, 20], smart cards and radio frequency identification tags [21, 22], nonvolatile memories [23], sensors [24, 25], smart skins [26], smart textiles [27] and "invisible electronics" [28], are some of the more important areas that have been reported.

Rao and Wong [29] investigated the properties of a polymer-ceramic composite which is a prime candidate for embedded capacitor technology. The manufacturability of a polymer combined with the electrical properties of a ceramic shows great potential. In addition, embedded capacitors have been shown to have improved electrical performance as well as reduced assembly cost compared with traditional discrete capacitor technology. Their work was based on a high-k epoxy system with a dielectric constant of 6.4 and the addition of two ceramic fillers, PMN-PT and $BaTiO_3$. Polymer-ceramic composites were developed by employing the ball-milling process. The average particle radius of PMN-PT and $BaTiO_3$ were 0.9 and 0.050 $\mu$m, respectively. The embedded capacitors were fabricated into a parallel-plate configuration, with the material thickness being 3.75 μm. Capacitance-voltage measurements showed that the dielectric constant ($\varepsilon_r$) was 150 and remained constant for frequencies varied from 10 kHz to 1.8 GHz. Also, the composite had a very high breakdown voltage, low leakage current and capacitance density of 35 $nF/cm^2$; making this system attractive for RF applications.

Another very significant application of a high-k dielectric material is used as a gate insulator in organic electronics FETs. In general, organic materials have received great interest as a new approach to low cost, large area flexible electronics [30-32]. Intense efforts have focused on improving mobility in organic semiconductors [33]. Another way of enhancing device performance is by increasing the dielectric constant of the gate dielectric material while properties such as flexibility and printability should be maintained. A dielectric with higher permittivity serves to increase the on-current of the FET for a given gate voltage, thereby permitting the device to operate at lower voltage.

Chen et.al. [34] proposed a OTFT structure with enhanced dielectric properties of the gate insulator, compared to $SiO_2$. The dielectric composite layer consisted of PVP and $TiO_2$ nanoparticles. Due to the nanoscale size of the $TiO_2$ there was uniform dispersion in the organic solvent and the OTFTs showed enhanced field-induced current indicative of the higher gate capacitance. Figure 1-2 illustrates a cross section of the OTFT. ITO patterned on a glass substrate was used as a gate electrode. A 30 nm additional layer of PEDOT was deposited on top of the ITO to decrease the surface roughness. The dielectric composite layer was added and the pentacene was then deposited, via spin coating, as the semiconducting layer. The gold source and drain electrodes were obtained by evaporation through a shadow mask. The dielectric constant of the dielectric film was increased with increasing concentration of $TiO_2$ nanoparticles. For a 7% $TiO_2$ mass loading the dielectric layer showed a dielectric constant of 5.4; almost 40 % higher than $SiO_2$.

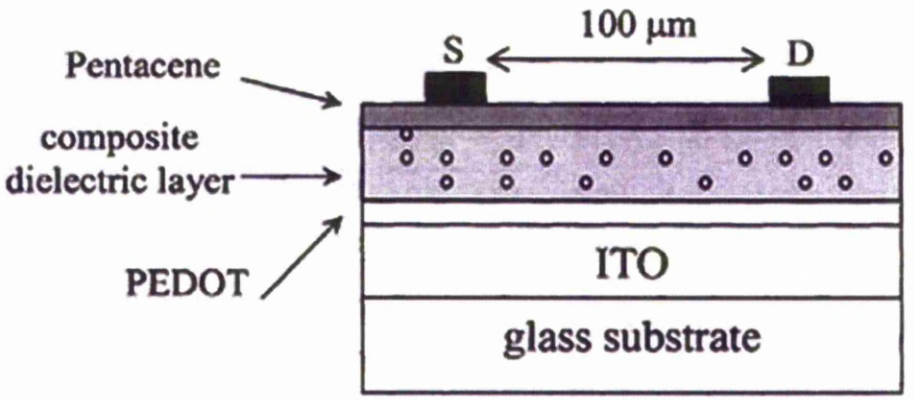


*Figure 1-2: The device structure of OTFTs*

Maliakal et. al. at Bell Laboratories reported the design and synthesis of a novel core-shell nanoparticle based gate dielectric using titanium oxide as the core and polystyrene as the flexible shell [35]. This material was easy to process and formed transparent continuous thin films, which exhibited a dielectric constant enhancement of over 3 times that of bulk polystyrene. The reason why TiO was chosen is that it is easily processible in contrast to $TiO_2$ or $SrTiO_3$ that have dielectric constants higher than TiO.

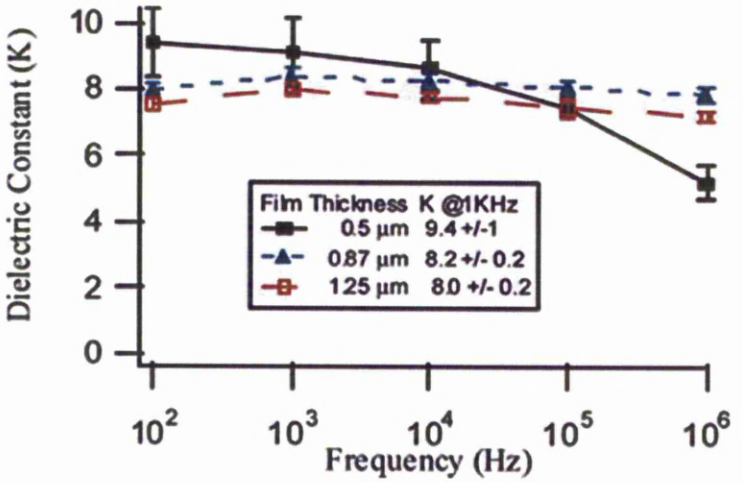


*Figure 1-3: Frequency dependence of k for films of TiO-PS (18.2 vol %TiO) of varying thickness [35].*

The dielectric constant ($k$) was measured in metal-insulator-metal (MIM) capacitors and exhibited up to a 3.6 times enhancement in $k$ compared to polystyrene at only 18.2 volume % loading. Figure 1-3 illustrates the frequency dependence of k for thin films of TiO of varying thickness. Pentacene TFTs exhibit mobility approaching 0.2 $cm^2/V_s$.

In 2005 the dielectric properties of in-situ formed silver (Ag) incorporated carbon black (CB)/polymer composites were studied by Lu et.al [36]. In-situ formed Ag nanoparticles in the Ag/CB/epoxy composites illustrated in Figure 1-4, increased the dielectric constant value and decreased the dissipation factor (*Df*) compared to CB/epoxy. The sample with 3.7 wt% Ag showed a $k$ of 2259 while the *Df* was maintained at around 0.45, which was much lower than the sample without Ag nanoparticles ($k$: 1600, *Df*: 0.7). The remarkable increase of $k$ was explained by the

possibility of pilling up of charges at the extended interface and/or more conducting particles based on the percolation theory.

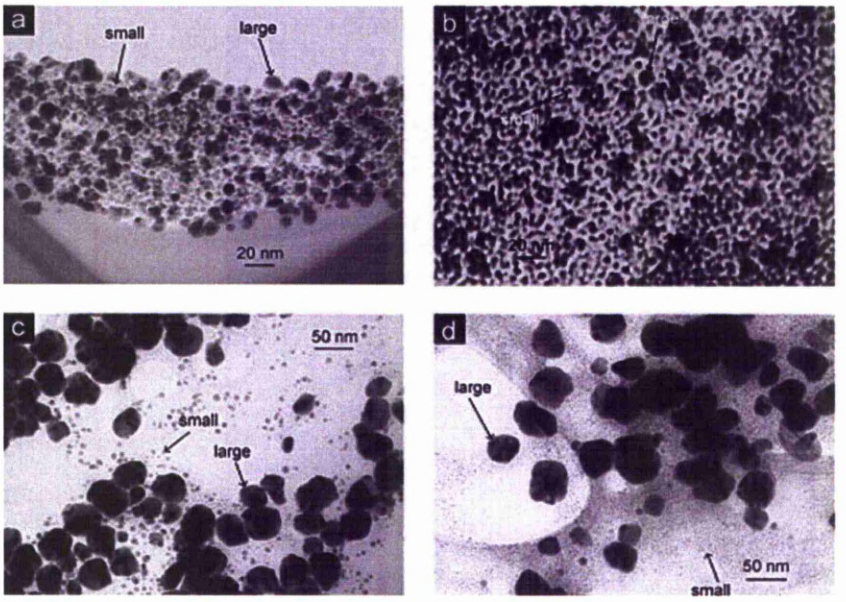


*Figure 1-4: TEM micrographs of uncured Ag/epoxy mixtures in the presence of a capping agent with [CA]/[AgNO3] ratios (a) R = 1, (b) R = 0.6, (c) R = 0.4 and (d) R = 0.2.*

It was suggested that the reduced dielectric loss might be due to the Coulomb blockade effect of the Ag nanoparticles. The Coulomb blockade effect is one of the well-known quantum effects of metal nanoparticles. If the size of the metal nanoparticle or so-called Coulomb island is small, the tunneling electron creates an additional barrier due to the charging energy $e^2/2C$ (where $e$ is the electron charge unit, and $C$ is the capacitance of the metal island) to the transfer of further electrons. When the charging energy exceeds the thermal fluctuation energy $k_BT$, where $k_B$ is the Boltzmann constant and T is the absolute temperature, the Coulomb blockade will occur, which inhibits the charge transfer through the small island below a certain voltage threshold and leads to an increase in resistance [37-39]. They also concluded that the size distribution and loading level of Ag nanoparticles in the nanocomposite may have significant influence on the dielectric properties of the composite system and describe other effects likely to be evident in different frequency ranges as well.

Facchetti et. al. reported the fabrication of high-k nanocomposite gate dielectrics for low voltage organic thin film transistors [40]. They explained that the key to low voltage operation is the reduction of the inverse sub-threshold slope and hence the threshold voltage. These transistor parameters are controlled by the gate dielectric as well as the semiconductor doping level. They used $CeO_2$-$SiO_2$ nano-composite films as the gate dielectric in organic thin film transistors OTFTs with pentacene as the active semiconductor. The $CeO_2$-$SiO_2$ composite films exhibited a high capacitance density of 57 nF/cm$^2$ with exceptionally low leakage current (see Figure 1-5). Good device characteristics were obtained with saturation at low operating voltages (≈ 2V) and with a field effect mobility of 0.84 cm$^2$ V$^{-1}$s$^{-1}$, a threshold voltage of ≈ 0.25 V, an on/off current ratio of 103, whereas the gate leakage current density was considerably lower.

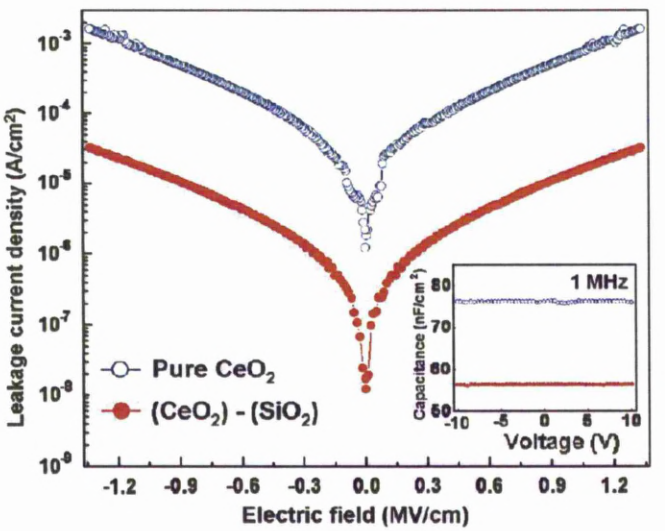


*Figure 1-5: Plots of J-E and high-frequency 1 MHz C-V characteristics, inset measured from the Au/dielectrics/ITO structure.*

The same concept was applied for the fabrication of gate dielectrics consisting of benzocyclobutene (BCB) and Barium Titanate nanoparticles. Electrical and dielectric properties were investigated [32]. To characterize the dielectric properties of the nanocomposite, parallel plate capacitors of the high-k composite materials were fabricated on a glass substrate with both gold top and bottom electrodes formed by coating with a DC sputtering. The capacitance was measured over the frequency

range from 10 kHz to a few MHz. The thickness of the dielectric films was measured directly and was used to calculate the dielectric constant and dielectric strength of the sample. They achieved values of $k$ just above 50 and capacitance density of 19 nF/cm$^2$ for a barium titanate loading of 50 % volume. The dielectric breakdown strength could be maintained at 1.65 MV/cm which is higher than some other polymers. Figure 1-6 (a) depicts the electrical output characteristics of the OFET prototype and Figure 1-6 (b) shows the schematic view of the transistor.

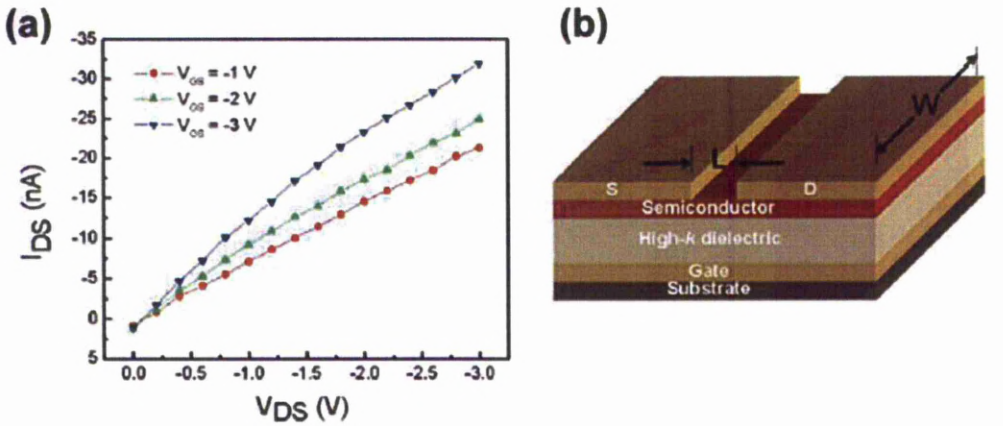


*Figure 1-6: (a). Electrical output characteristics (drain current, $I_{DS}$ vs. drain voltage, $V_{DS}$) of OFET prototype and (b) the schematic structure of a top contact OFET prototype with a high-k nanocomposite gate insulator [30].*

In 2007, Zirkl et.al, developed an opto-thermal capacitive sensor element [28]. They fabricated a low-voltage organic transistor with high-$k$. Gate dielectrics $Al_2O_3$ and $ZnO_2$ combined with poly(a-methyl styrene) (PaMS) or poly(vinyl cinnamate) (PVCi) to form a smooth and dense nanocomposite. Pentacene was used as the organic semiconductor material, the gate electrode was Al, while Au source and drain electrodes were employed. The interface quality of various organic and nanocomposite gate dielectrics with pentacene resulted in superior low-voltage operating OTFTs, suitable for advanced sensor applications with low power consumption. In a transducer configuration, the transistor devices were integrated with pyroelectric polymer sensors and acted as an optothermally activated switch and as a sensitive infrared detector. In matrix arrays of such transducers, OTFTs were shown to be promising elements in high performance sensor systems.

Choi et.al, reported embedded capacitors [43]. The dielectric properties of polymer/ceramic composite films were shown to be largely influenced by the dispersion and loading of the ceramic in the polymer matrix. In order to increase the effective dielectric constant of polymer/ceramic composite films, a larger loading volume with homogeneous dispersion of ceramic fillers was shown to be important. However, the composite films comprised of ferroelectric fillers with high volume content generally suffered from high dielectric losses in the microwave frequency region due to the intrinsic capacitive hysteresis of the ferroelectric materials employed. Therefore, it was concluded that new ceramic fillers with low losses that could still retain a high dielectric constant at a high frequency regime were required. High dielectric constant and low loss polyimide/$Bi_2O_3$-$ZnONb_2O_5$ (BNZ) composite films pyromellitic dianhydride (PMDA) and 4,4'-oxydiamiliane-(ODA)-based polyimide were prepared. Homogeneous dispersion of pyrochlore structure BNZ particles was obtained. The polyimide composite with BZN particles (BZN content at 50 vol %) treated by INAAT showed a reduced dielectric loss of 0.0369 at 12 MHz while retaining a reasonably good dielectric constant of 15. These results demonstrated the potential of employing BZN ceramic fillers for low dielectric loss, relatively high dielectric constant capacitors using polyimide/BZN composite for application in a RF embedded capacitor suitable for microwave frequency regime.

The results provide encouragement that high-*k* composite dielectrics show promise for commercial applications. Reports are being published with increasing frequency and new ideas for applications are put forward. Because of the fact that the demand in the electronic industry is huge and many new needs have emerged, high dielectric constant composites are a domain that is worth examining.

Usually, the formation of metal oxide nanoparticles, with enhanced dielectric properties, is a complex procedure that is time-consuming and expensive. Various methods have been proposed in the past, not only to improve NP efficiency or NP properties but also to minimize time and cost in order to have industrial interest. Towards that direction, this study presents a gas-phase method, named as arc-discharge in water, which combines high yield of NP production as well as low cost. This eco-friendly method takes advantage of several physical and chemical processes that occur without the need of sophisticated vacuum systems or other complicated experimental arrangements.

## 1.3. FABRICATION METHODS OF NANOPARTICLES

Nanoparticles of a wide range of materials can be produced by two main methods; liquid and vapour phase (also known as "gas phase") synthesis. The formation method plays a significant role on the NP size, chemical composition, as well as surface and charge properties. The nature of the production methods is also critical for its integration into existing production process lines. Liquid phase is considered to be the appropriate route to achieve a narrow size distribution and in most cases with a low agglomeration index. However, gas phase synthesis is preferred in industry since it can provide large quantities of particles with high throughput. The most common fabrication methods are mentioned briefly below:

### 1.3.1. LIQUID PHASE SYNTHESIS

#### *1.3.1.1. Sol-gel method*

The sol-gel approach is a cheap and low temperature technique for fine control of chemical composition. It is the most common method of producing NPs in the liquid phase and it is widely used in the fields of materials science and ceramic engineering. It involves a chemical precursor 'sol' and a gel of particles or network polymers. The precursor sol can be either deposited on a substrate to form a film, cast into a suitable container with the desired shape, or used to synthesize powders [44].

The solid nanoparticles are dispersed in a liquid (sol) agglomerate together to form a continuous three-dimensional network extending throughout the liquid (gel). The NPs of the sol can be grown directly in the liquid by mixing ingredients that contain molecules which then interconnect to form bigger molecules and eventually nanoparticles. These NPs then agglomerate to form a gel network. Another route is to synthesize the NPs and then disperse them in a liquid.

A sol can become a gel when the solid nanoparticles dispersed in it can join together to form a network of particles that spans the liquid. For some nanoparticles

this is almost automatic, since they contain reactive surface groups that condense together to form bonds. For other nanoparticles, however, this can be problematic and requires an additive to "glue" the particles together either through modification of the particle surface or by electrostatic attraction. As a sol becomes a gel, its viscosity approaches infinity and the constituents finally become immobile.

The formation of structures in the nanoscale was reported by Farag et.al [45]. Alumina, titania and alumina-titania in an ionic liquid were fabricated by sol-gel synthesis using aluminium isopropoxide and titanium isopropoxide as precursors. For alumina synthesis, a solution of 1 M $Al(OPr\text{-}i)_3$ in $[Py_{1,4}]$TFSA was prepared and then hydrolysed by dropwise addition of an appropriate amount of water. An emulsion was formed and then aged at 90 °C for about 12 h to form a gel under stirring. Afterwards, approximately a twofold volume of acetone was added into the reaction system and stirring maintained with refluxing at 50 °C for about 12 h. Then the mixture was centrifuged to reclaim the hydrolysis product. Finally, the hydrolysis product was left to dry in dry air for about 24 h, before calcination.

The same procedure was employed for the synthesis of titania using 1 M $Ti(OPr\text{-}i)_4$ in $[Py_{1,4}]$TFSA. Alumina–titania was synthesized by co-hydrolysis of a mixture of 1 M $Al(OPr\text{-}i)_3$ and 1 M $Ti(OPr\text{-}i)_4$ in $[Py_{1,4}]$TFSA. The synthesized samples were calcined in a muffle oven at the desired temperature for 2 h and were cooled down to the ambient temperature in the oven.

### *1.3.1.2. Spray Pyrolysis method*

Spray pyrolysis is a widely-used method since it does not require quality targets or substrates, no UHV system is needed and it has high throughput. One of the unique characteristics of spray pyrolysis is that the chemical reaction occurs within the micron to sub-micron sized liquid droplets; it constituents, a so-called microcapsule reactor.

Thin films are deposited by spraying a solution on a heated surface, where the constituents react to form a chemical compound. The chemical reactants are selected such that the waste products are volatile at the temperature of deposition. The process is particularly useful for the deposition of oxides and has long been a production method for growing a transparent electrical conductor of SnOx on glass [46]. There have been many studies in this area since the pioneering paper by Chamberlin &

Skarman [47] on CdS films for solar cells [48, 49] in 1966, among them a review of transparent conductors [50] and a bibliography Pamplin [51].

Viguie & Spitz [52] classified chemical spray deposition processes according to the type of reaction. Initially, the droplet resides on the surface as the solvent evaporates, leaving behind a solid that may further react in the dry state. The solvent evaporates before the droplet reaches the surface and the dry solid impinges on the surface, where decomposition occurs. The solvent vapourizes as the droplet approaches the substrate; the solid then melts and vapourizes, and the vapour diffuses to the substrate, there to undergo a heterogeneous reaction. They identified this process as true chemical vapour deposition. In the last stage, the entire reaction takes place in the vapour state.

When spraying areas of a few square centimeters, liquid flows of 1-20 ml/min have been reported [53]. Sufficiently low-flow commercial pneumatic spray heads are not readily available, and a needle valve is needed to restrict the flow. Acidic solutions attack stainless steel to the extent that iron contamination of the deposit is a problem. Air is the usual propellant, typically at 20 psi with a flow rate of 20 litres/min. When oxygen contamination is a problem, an inert gas within an enclosure is used. Because spray patterns are inevitable and result in uneven deposition thickness, a random motion of the spray head, the substrate, or both is useful for uniform deposition [54-57]. Several variables can affect the final product such as solute concentration, atomization technique, temperature, residence time in furnace and carrier gases.

#### *1.3.1.3. Co-precipitation method*

Another route for the formation of nanoparticles using a liquid phase synthesis is the co-precipitation method. The procedure involves a solid which contains various ionic species precipitating out of a solution. The resulting precipitates are heated to appropriate temperature in suitable atmospheres to produce the desired compound. The co-precipitation method is a simple and rapid preparation with easy control of particle size and composition. It offers various possibilities to modify the particle surface state and overall homogeneity.

The synthesis process of indium tin oxide (ITO) nanoparticles by liquid phase co-precipitation was reported [58] with indium chloride and tin chloride as the main

raw materials. The experimental procedure involved indium chloride ($InCl_3 \cdot 4H_2O$ 99%, Aldrich) and tin chloride ($SnCl_4 \cdot 5H_2O$ 99%, Aldrich) which were dissolved in pure de-ionized water or ethanol, keeping the ratio of $In_2O_3$ : $SnO_2$ = 9 : 1. The particle size distribution was between 30 and 90 nm.

### 1.3.2. GAS PHASE SYNTHESI

#### *1.3.2.1. Inert Gas Condensiation*

One of the most straightforward methods of creating the right environment (supersaturation) for nanoparticles to evolve is by heating a solid until it evaporates into a background gas. The mixture of the vapour with a cold gas will ultimately reduce the temperature leading to vapour condensation and formation of nanoparticles. Depending of the form of cold gas, the properties of the particles can be controlled; for example if the heated solid is a metal and the cold gas is oxygen then the result will be metal oxides.

Gracia-Pinilla et.al.used this method for the formation of copper nanoparticles and their deposition on a substrate [59]. The size-selected Cu nanoparticle deposition takes place through four main processes: sputtering, aggregation, filtering, and deposition. It was found that both the nature and the flow rate of the background gas (herein Argon and Helium) affected the size distribution. Additionally, the sputtering power but most importantly the aggregation length along with the vapour was found to interact with the background gas to affect the size of the resulting particles. Typically the pressure in the condensation zone was 1-20 mbar.

#### *1.3.2.2. Pulsed Laser Ablation*

Pulsed laser ablation is a similar route to the evaporation of a material by sputtering. However, the difference in this case is that by using a laser pulse, a plume of material vapourizes spatially. Depending on the laser beam intensity the target material can evaporate, sublimate or even convert to plasma. Laser ablation refers to removing material with a pulsed laser, but it is possible to ablate material with a continuous wave laser beam if the laser intensity is high enough. This method does not require solvents, is easy to automate, is more gentle than abrasive techniques and

the heating of the target is minimal. Although it is mainly used for elements that are not easily evaporated, in terms of production rate, it is not the most effective one.

Controlling the average particle size was described by Knang and Lee [60]. Hot-pressed 1 mm-sized Si powder (purity 99.99%) was used as a target. A 248-nm KrF excimer laser with pulse duration 25 ns was used for irradiation. The incident beam, of fluence 2–10 J/cm$^2$, was focused on the surface of the target by a convex lens having a focal length of 124 mm. The laser ablation was done in a vacuum system, the base pressure of which was $10^{-3}$ torr. The target was rotated at a speed range of 8–10 rpm during irradiation. Ar with a flow rate of 0.1–1 L per min (l pm) was used as a background gas. Pressure was maintained at 3–20 torr during irradiation. The nanoparticles were passivated by thermal oxidation of their surface. Oxidation and deposition of Si nanoparticles onto a wafer was performed in-situ following the ablation process. The particles were oxidised ex-situ in $O_2$ atmosphere at 1,050 °C in a tube furnace. The oxidized Si nanoparticles were then electrostatically deposited onto a wafer. The outcome of the study showed that this technique can produce not only high purity silicon nanoparticles but also narrow size dispersion (mean size 4-5 nm) by applying positive voltage.

#### *1.3.2.3. Ion beam sputtering*

Another fabrication method that was been widely used to vapourize solids is through sputtering with a beam of inert gas ions. Several metals have been reported to form nanoparticles when employing magnetron sputtering of metal targets. This procedure forms nanostructured films which in turn, are deposited on substrates (usually silicon) and requires low pressures (~1 mTorr); a fact that makes the processing of particles difficult.

Unrban et.al. tested a large number of source metals using this ion sputtering technique [61]. There were three vacuum chambers which communicated by low conductance connections and maintained at three successively lower pressures by differential pumping. The chapters had pressures of approximately 1 Torr, $1x10^{-3}$ Torr, and $1x10^{-5}$ Torr. The right-hand side was the source chamber into which an adjustable mixture of ultrahigh purity Ar and He could be admitted under computer control. A 75 mm diameter magnetron sputtering gun is mounted in this chamber to provide a source of sputtered species. The walls of the source chamber are liquid

nitrogen cooled and the temperature monitored and controlled using two thermocouples. A computer data acquisition system was also fitted to the system.

A low velocity beam of the gas and nanoparticles was formed as they escaped through the converging–diverging exit nozzle, which was 3 mm in diameter at the throat. The middle region was cryo-pumped and normally operateed at $5x10^{-4}$ torr. Large heavy species (nanoparticles) would, in principle, go straight through this region. Most of the lighter inert and background gasses would be scattered in random directions and pumped out. Thus, the middle chamber was where most of the separation of process gas and nanoparticles takes place. The beam of nanoparticles and a small amount of gas entered the diffusion-pumped deposition chamber through an aligned aperture, 1 cm in diameter. The beam impinged on the substrate upon which a thin film then grows. The beam could be manipulated by an ionizer as well as by deflection and acceleration electrode structures that were mounted within the deposition chamber. Films were deposited onto 75 mm diameter Si(001) wafers which were shadowed by 1 mm wide mechanical masks to produce steps for thickness measurements.

#### *1.3.2.4. Arc-discharge in liquids*

Arc-discharge in water [62-70] or other liquids [64, 71, 72 (solid–liquid arc), 73] has extensively been used as a gas-phase technique for the production of a variety of NPs: $WO_3$ [66], Si [66], Au [68, 71], Ag [69, 70], CuO [70], Cu [72], $Cu_2O$ [72], core-shell $MoS_2$ [65], nanocomposites [73], nanotubes [64, 74, 75], 'onions' [62-64, 74, 75] and nanowires [67].

This method is eco-friendly and easy to implement compared to the previous mentioned gas phase methods since the only equipment necessary is a power supply (DC or AC). A schematic diagram of the basic experimental set-up of the arc discharge in water is shown in Figure 1-7. Two electrodes are connected at the edges of the power supply, positive and negative pole. The process takes place inside the beaker filled with a liquid chosen according to the experiment needs and both electrodes are submerged in it. As the electrodes are brought into contact, minor arcs take place creating a high temperature plasma environment. The localized high energy melts the anode (atomization) and sends away, from the core of the plasma to the surrounded liquid, the suspended particles. This phenomenon is called quenching and

it is the reason why the nanoparticles are formed. As free atoms of various species are in the plasma area and start to reassemble particles the cold liquid instantly stops the crystal growth resulting in particles which are only a few nanometers in diameter. Since the anode is the one that is consumed, the user can define the kind of particles desired. In the case of arc discharge in water, $H_2O$ bonds break into oxygen and hydrogen which in turn, allows the oxidization of metallic atoms of the anode. Detailed description of the system used in the present work, together with the diagnostic devices attached to it, will be discussed in later chapters.

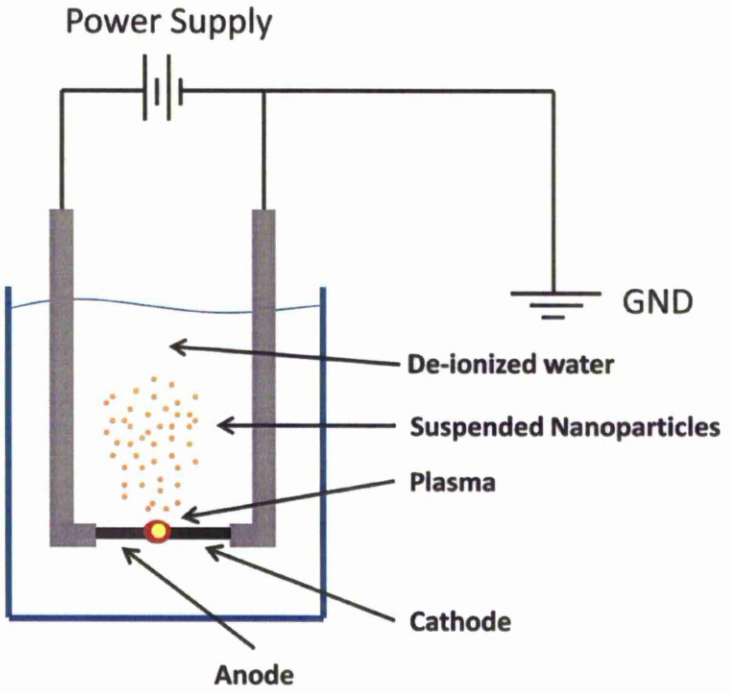


*Figure 1-7: Schematic diagram of arc-discharge in water.*

A significant breakthrough that regenerated the use of this method was the formation of carbon nano-onions by arc discharge in water [63]. Instead of using expensive vacuum systems to generate plasmas, this simple method used two graphite electrodes immersed in de-ionized water and produced high yields of scientifically interesting nano-materials at low cost. With average particle size of 25-30 nm and a production rate of 3 mg $min^{-1}$ carbon nano-onions appeared to be prime candidates for many lubrication applications.

Similar experiments were performed using essentially the same apparatus for the formation of $MoS_2$ core-shell nanoparticles [65]. The two electrodes, a conical

graphite cathode and a hollow Mo rod anode packed with $MoS_2$ powder (99.9% purity) of about 44 $\mu$m particle size, were immersed in de-ionized water, about 5 cm below the surface, and an arc of 30 A (DC) was generated between them. This nano-powder widened the scope for the use of arc in liquids for producing a variety of catalysts.

Uniformed and monodispersed CuO nanorods were also synthesized from a solid-liquid arc discharge process [71]. High purity 1.5 mm in diameter filaments were used as electrodes. After being dipped in $NaNO_3$ solution, they were brought into contact while 150 V AC voltage formed the instantaneous circulation between the two electrodes. This resulted in the continuous dissolution of the copper electrode into the solution due to the great exothermic heat released during the arc discharge, and the newly formed Cu clusters will rapidly be oxidized and form a CuO colloidal solution. To synthesize $Cu_2O$ and Cu nanoparticles, 0.1 mol/L ascorbic acid and 1 mL of hydrazine hydrate (35 wt %) were added, respectively, into the initial solution. This method enabled the controlled oxidization of Cu nanoclusters.

Tungsten trioxide ($WO_3$) is a wide band gap semiconductor known for its unique characteristics such as photocatalytic activity, gas sensing effects, electrochromic coatings and microelectronic applications. Ashkarran et. al. prepared $WO_3$ NPs from pure tungsten via one step electrical arc-discharge [66]. Tungsten electrodes, 1.5 mm in diameter, were immersed in de-ionized water and the circuit was fed by a 10 V DC voltage with a high current of 25 A. The results showed $WO_3$ nanoparticles with average diameters of 30 nm whereas the size was increased as the arc current was increased.

## 1.4. OBJECTIVES OF THIS WORK

In this project, the arc discharge in de-ionized water method was used in the formation of metal oxide nanoparticles with dielectric properties. A new vertical arc discharge system has been designed and fabricated and three different anode materials have been tested; aluminium rod, tantalum rod and a mixture of tantalum-copper powder grains. The cathode in all cases was a carbon rod. The experiments included the in-situ monitoring of the electrical and optical characteristics of the arc-plasma in

order to observe the production mechanism of the product and the nanoparticle characterization in various techniques to study their chemical and structural composition. The data appears to confirm that arc discharge in water can be established as a method of producing high purity metal oxide NPs.

## 1.5. ORGANISATION OF THIS THESIS

Chapter 2 is devoted to a brief review to the main experimental techniques employed in the nanoparticle characterization as well as the arc system. High Resolution Transmission Electron Microscopy (HRTEM), Scanning Transmission Electron Microscopy (STEM), X-Ray Diffraction (XRD) and X-Ray Photoelectron Spectroscopy are the main techniques used in the NP characterization. The main principles of HREM and the factors influencing the clarity of an HREM image are discussed. Similarly, the individual techniques such as Energy-dispersive X-ray spectroscopy (EDX) and high-angle annular dark-field imaging (HAADF) of STEM are described. The information that XRD and XPS analysis can provide in terms of chemical composition are also mentioned. All the diagnostic tools attached to the arc-discharge system to monitor the process; Optical Emission Spectroscopy and electrical measurements are briefly reviewed and the experimental configuration, as used in this study, is presented in detail. Initial data that led to the idea of producing dielectric metal oxide NPs using this method are finally mentioned.

Chapter 3 includes the results from the arc-discharge in water using an aluminium rod as an anode electrode. The discharge behaviour is monitored by electrical (voltage, current, power) and optical (using a photomultiplier) measurements. High speed imaging and OES are employed to record several arc-runs and identify the active species within the plasma. The electrode mass reduction rate is also measured. The product of the discharge is characterized by HRTEM, XRD and XPS.

The justification that the arc-discharge method can be used for the formation of metal oxides is presented in chapter 4, where a tantalum rod, instead of aluminium, is used. The measurements on the tantalum arc are identical with that of the aluminium, in order to compare how the arc responds in different anodes. As in

chapter 3, particle characterization techniques, HRTEM, XRD and XPS, are employed in tantalum product.

The results from a composite metal arc discharge are given in chapter 5. Tantalum and copper powder grains have been mixed and compressed to form a solid tablet and the mixture was used as an anode. Electrical characteristics, high-speed imaging, optical emission spectroscopy and electrode mass reduction measurements have been applied to the system. In terms of nanoparticle characterization, apart from HRTEM, EDX maps and HAADF imaging has been employed to characterize structurally this new core/shell nano-product. The chemical composition of the nano-powder has been examined using XRD and XPS analysis. Since this core/shell structure has not been mentioned anywhere in the literature, Broadband Dielectric Spectroscopy (BDS) has been employed to derive the relative permittivity and dielectric loss behaviour in a wide range of temperatures and frequencies.

The main results from this thesis are concluded in Chapter 7. Summarising and comparing the data of this work, the arc discharge has been to be a viable method for the production of metal oxide nanoparticles with dielectric properties. Finally, suggestions for future work are stated, recommending new composite materials to be tested as well as ideas for modifications to the experimental configuration that will increase the efficiency and quality of the nanoparticles.

## 1.6. REFERENCES


[1] J. L. Gole, J. D. Stout, W. L. Rauch and Z. L. Wang, *App. Phys. Lett.,* 76, 17 (2000).

[2] Y. Sua, Z. Yanga, H. Weia, E. S.-W. Konga and Y. Zhang, *App. Surf. Sci.* 257, 3123 (2011).

D. Ung, L. D. Tung, G. Caruntu, D Delaportas, I. Alexandrou, I.A. Prior, N. T. K. Thanh, *Cryst. Eng. Comm.* 11, 7, 1309 (2009).

[4] H. A. Dabbagh, E. Rasti, M. S. Yalfani, F. Medina, *Mater Res Bull,* 46, 271 (2011).

[5] R. Yuge, T. Ichihashi, Y. Shimakawa. Y. Kubo, M. Yudasaka and S. Iijima, *Adv. Mater.,* 16, 16 (2004).

[6] W. Tan, K. Wang, X. He, X. J. Zhao, T. Drake, L. Wang, R. P. Bagwe, *Med. Res. Rev*, 24, 621 (2004)

[7] T. Neuberger, B. Schopf, H. Hofmann, M. Hofmann and B. von Rechenberg, *J. Magn. Magn. Mater.* 293, 483 (2005).

[8] R. Saito, G. Dresslhaus, M. S. Dresselhaus, 'Physical Properties of Carbon Nanotubes', Imperial College Press (London), ISBN 1-86094-093-5, 2000.

[9] B. S. Harrison and A. Atala, *Biomaterials*, 28, 344 (2007).

[10] D. A. Heller, S. Baik, T. E. Eurell, M.S. Strano,. *Adv. Mater.,* 17, 2793 (2005).

[11] C. R. Martin and P. Kohli, *Nat. Rev. Drug. Discov.,* 2, 29 (2003).

[12] R. Singh, D. Pantarotto, D. McCarthy, O. Chaloin, J. Hoebeke, C. D. Partidos, J.-P. Briand, M. Prato, A. Bianco, and K. Kostarelos, *J. Am. Chem. Soc.,* 127, 12, 4388 (2005).

[13] S. Joseph, R. J. Mashl, E. Jakobsson, N. R. Aluru., *Nano. Lett.*, 3, 10, 1399 (2003).

[14] E. Ruoslahti, S. N. Bhatia, M. J. Sailor, *J. Cell. Biol.*, 188, 759 (2010).

[15] L. R. Hirsch, R. J. Stafford, J. A. Bankson, S. R. Sershen, B. Rivera, R. E. Price, J. D. Hazle, N.J. Halas, J. L. West., *Proc. Natl. Acad. Sci. USA.* 100, 13549 (2003)

[16] M. Hu, J. Chen, Z. Y. Li, L. Au, G. V. Hartland, X. Li, M. Marquez, and Y. Xia., *Chem. Soc. Rev.* 35, 1084 (2006).

[17] J.-H. Park, G. V. Maltzahn, M. J. Xu, V. Fogal, V. R. Kotamraju, E. Ruoslahti, S. N. Bhatia, and M. J. Sailor., *Proc. Natl. Acad. Sci. USA.* 107, 981 (2010).

[18] Park, J.-H., G. von Maltzahn, L. Zhang, A.M. Derfus, D. Simberg, T. J. Harris, E. Ruoslahti, S. N. Bhatia, and M. J. Sailor. *Small.* 5, 694 (2009).

[19] L. Zhou, A. Wanga, S.-C. Wu, J. Sun, S. Park, T. N. Jackson,, *Appl. Phys. Lett.*, 99, 083 502. (2006).

[20] W. Fix, A. Ullmann, J. Ficker, W. Clemens, *Appl. Phys. Lett.* 81, 1735. (2002).

[21] P. F. Baude, D. A. Ender, M. A. Haase, T. W. Kelley, D. V. Muyres, and S. D. Theiss, *Appl. Phys. Lett.* 82, 3964. (2003).

[22] R. C. G. Naber, C. Tanase, P. W. M. Blom, G. H. Gelinck, A. W. Marsman, F. J. Touwslager, S. Setayesh, and D. M. de Leeuw, *Nat. Mater.* 4, 243. (2005).

[23] B. Crone, A. Dodabalapur, A. Gelperin, L. Torsi, H. E. Katz, A. J. Lovinger, and Z. Bao, *Appl. Phys. Lett.* 78, 2229 (2001).

[24] I. Graz, M. Kaltenbrunner, C. Keplinger, R. Schwödiauer, S. Bauer, S. P. Lacour, S. Wagner,, *Appl. Phys. Lett.*, 89, 073 501. (2006).

[25] T. Someya, Y. Kato, T. Sekitani, S. Iba, Y. Noguchi, Y. Murase, H. Kawaguchi, T. Sakurai,, *Proc. Natl. Acad. Sci. USA, 102*, 13, 231. (2005).

[26] M. Maccioni, E. Orgiu, P. Cosseddu, S. Locci, and A. Bonfiglio, *Appl. Phys. Lett.*, Vol 89, 143 (2006).

[27] L. Wang, M.-H. Yoon, G. Lu, Y. Yu, A. Facchetti, T. J. Marks, *Nat. Mater. 5*, 893. (2006).

[28] M. Zirkl, A. Haase, A. Fian, H. Schön, C. Sommer, G. Jakopic, G. Leising, B. Stadlober, I. Graz, N. Gaar, R. Schwödiauer, S. Bauer- Gogonea, S. Bauer, *Adv. Mater. 19*, 2241–2245. (2007).

[29] Y.Rao and C. P.Wong, *J. Appl. Pol. Sci.*, 92, 2228 (2004).

[30] S. R. Forrest, *Nature*, Vol. 428, No. 911. (2004).

[31] H. Katz, *Chem. Mater.*, Vol. 16, p. 4748. (2004).

[32] D. Gamota, *Printed Organic and Molecular Electronics.* (2004)

[33] C. Dimitrakopoulos and P. R. L. Malenfant, *P. Adv. Mater.,* Vol. 14, No. 99. (2002).

[34] F. C. Chen, C. W. Chu, J. He, Y. Yang, *Appl. Phys. Lett.,* Vol. 85, No. 15, 11 (2004).

[35] A. Maliakal, H. Katz, P. M. Cotts, S. Subramoney, P. Mirau., *J. Am. Chem. Soc.*, Vol. 127, 14655 (2005).

[36] J. Lu, K. S. Moon, J. Xu, C. P. Wu, *J. Mater. Chem.,* 16, 1543 (2006).

[37] D. K. Ferry and S. M. Goodnick, *Tr. in Nanostructures, Cam. Univ. Pr., London.* (1997).

[38] C. A. Berven, L. Clarke, J. L. Mooster, M. N. Wybourne, and J. E. Hutchison, *Adv. Mater.*, 13, No 109 (2001).

[39] Q. Feng, Z. M. Dang, N. Li and X. L. Cao, *Mater. Sci. Eng. B*, 99, 325 (2003).

[40] A. Facchetti, M. H. Yoon, and T. J. Marks, *Adv. Mater.*, 17, 1705 (2005).

[41] G. Horowitz, *J. Mater. Res.*, 19, 1946 (2004).

[42] J. Lu, K.-S. Moon and C. P. Wong, *Electronic Components and Technology Conference* (2007).

[43] S-H. Choi, I. -D. Kim, J.- M Hong, S.-G Oh, *Macromol. Symp.*, 249, 241 (2007).

[44] C.J. Brinker, G.W. Scherer *Sol-Gel Science: The Physics and Chemistry of Sol-Gel Processing.* Academic Press. (1990).

[45] H. Farag, M. A. Zoubi, F. Endres, *J. Mater. Sci.*, 44, 122 (2009)

[46] J. M. Mochel,. *US Patents* 2,564,707; 2,564,987; 2,564,709; 2,564,710; 2,564,708; 2,564,706 (1951).

[47] R. R. Chamberlin, J. S. Skarman, *J. Electrochem. Soc.* 113, 1, 86 (1966).

[48] R. R. Chamberlin, J. S. Skarman, D. E. Koopman, L. E. Jr. Blakely, *Tech. Doc. Rep. ASD-TDR-63-223, Part I*, AD 403 053. Washington, DC: NTIS (1963).

[49] R. R. Chamberlin, J. S. Skarman, *Solid State Electron.* 9, 819 (1966).

[50] J. S. Maudes and T. Rodrigues, *Thin Solid Films,* 69, 1, 83 (1980).

[51] B. R. Pamplin, *Prog. Cryst. Growth Charact.*, 1, 4, 395 (1979).

[52] J. C. Viguie and J. Spitz, *J. Electrochem. Soc.* 122, 4, 585 (1975).

[53] J. B. Mooney and S. B. Radding, *Ann. Rev. Mater. Sci.* 12, 81 (1982).

[54]. R. Pommier, C. Gril, J. Marucchi, *Thin Solid Films*, 77, 9, 1 (1981).

[55] V. P. Singh, *IEEE Photovoltaic Specialists Conj: 13th*, Washington DC, Piscataway, NJ: IEEE (1978).

[56] J. F. Jordan, *IEEE Photovoltaic Specialists Coni, 11th*, Scottsdale, Ariz., Piscataway, NJ: IEEE (1975).

[57] G. A. Roderick, *Proc. Eur. Community Photovoltaic Solar Energy Conf, 3rd*, Cannes, 327. Dordrecht, Holland: Reidel (1980).

[58] Z. Ding, C. An, Q. Li, Z. Hou, J. Wang, H. Qi, F. Qi, *J. Nanomaterials*, 1, 5 (2010).

[59] M. Gracia-Pinilla, E. Martınez, G. Silva, V. E. Perez-Tijerina, *Nanoscale Res Lett.* 5, 180 (2010).

[60] Y. Khang and J. Lee, *J Nanopart Res,* 12, 1349(2010).

[61] F. K. Urban, A. Hosseini-Tehrani, P. Griffiths, A. Khabari, Y.-W. Kim, I. Petrov, *J. Vac. Sci. Technol. B,* 20, 3 (2002).

[62] N. Sano, H. Wang, I. Alexandrou, M. Chhowalla, K. B. K. Teo, G. A. J. Amaratunga and K. Iimura, *J. Appl. Phys.* 92, 2783 (2002).

[63] N. Sano, H. Wang, , M. Chhowalla, I. Alexandrou, G. A. J. Amaratunga, *Nature,* 414, 506 (2001)

[64] I. Alexandrou, H. Wang, N. Sano, G. A. J. Amaratunga, *J. Chem. Phys.,* 120, 1055(2004).

[65] I. Alexandrou, N. Sano, A. Burrows, R. R. Meyer, H. Wang, A. I. Kirkland, C. J. Kiely and G. A. J. Amaratunga, *Nanotechnology,* 14, 913 (2003).

[66] A. A. Ashkarran, A. Irajizad, M. M. Ahadian, S. M. Mahdavi, *Nanotechnology,* 19 195709 (2008).

[67] S. M. Liu, M. Kobayashi, S. Sato and K. Kimura *Chem. Commun.* 4690 (2005).

[68] J. K. Lung, J. C. Huang, D. C. Tien, C. Y. Liao, K. H. Tseng, , T. T. Tsung, W. S. Kao, T. H. Tsai, C. S. Jwo, H. M. Lin, L. Stobinski, *J. Alloys Compounds,* 434, 655 (2007).

[69] C. H. Lo, T. T. Tsung and H. M. Lin *J. Alloys Compounds,* 434, 659 (2007).

[70] D. C. Tien, K. H. Tseng, C. Y. Liao, J. C. Huang and T. T. Tsung *J. Alloys Compounds* 463 408–11 (2008).

[71] A. A. Ashkarran, A. Irajizad, S. M. Mahdavi, M. M. Ahadian and M. R. H. Nezhad *Appl. Phys. A,* 96, 423 (2009)

[72] W. T. Yao, S. H. Yu, Y. Zhou, J. Jiang, Q. S. Wu, L. Zhang and J. Jiang *J. Phys. Chem. B*, 109, 14011 (2005).

[73] T. Charinpanitkul, A. Soottitantawat, N. Tonanon and W. Tanthapanichakoon, *Mater. Chem. Phys.,* 116, 125 (2009).

[74] G. Xing, S. L. Jia and Z. Q. Shi, *New Carbon Mater.,* 22, 337 (2007).

[75] H. Lange, M. Sioda, A. Huczko, Y. Q. Zhu, H. W. Kroto and D. R. M. Walton *Carbon* 41, 1617 (2003).

# 2. CHARACTERIZATION TECHNIQUES

## 2.1. INTRODUCTION

Different analytical techniques were used to characterize the synthesized samples as well as the discharge itself. As far as the nanomaterials are concerned, the main ones are Transmission Electron Microscopy (TEM), Scanning Transmission Electron Microscopy (STEM), X-Ray Diffraction (XRD) and X-ray Photoelectron Spectroscopy (XPS) whereas the discharge was monitored in-situ using Optical Emission Spectroscopy (OES) and electrical measurements. The latter includes the monitoring of the arc voltage, current, power as well as luminous activity. Here, a brief description of these techniques is given since they have been frequently used throughout this work.

### 2.1.1. HIGH RESOLUTION TRANSMISSION ELECTRON MICROSCOPY (HRTEM)

Electron microscopes are scientific instruments that use a beam of highly energetic electrons to examine objects on a very fine scale. They were developed after light microscopes for the sole purpose of higher resolution/magnification since the resolution of the light microscope is limited by the wavelength of light used. A good light microscope can have a resolution of about 300 nanometers while a High Resolution Transmission Electron Microscope (HRTEM) can easily reach a resolution limit of below 1 Angstrom (Å). Figure 2-1 shows a simple schematic of a TEM microscope. A TEM usually consists of an illumination system, a condenser lens system, a specimen stage, where the sample is mounted, an objective lens system, the magnification system, and the image recording unit.

The electron gun is the source of the illumination system, which typically uses a lanthanum hexaboride (LaB6) thermionic emission source or a field emission source, followed by an acceleration unit with a potential difference of the order of 100's of kV. The illumination system also includes the condenser lenses that are vitally important for forming a fine electron probe, controlling the intensity and

ensuring exposure illumination of the sample by a parallel beam of electrons. Part of the beam can be excluded to adjust the illumination characteristics also, using the condenser aperture.

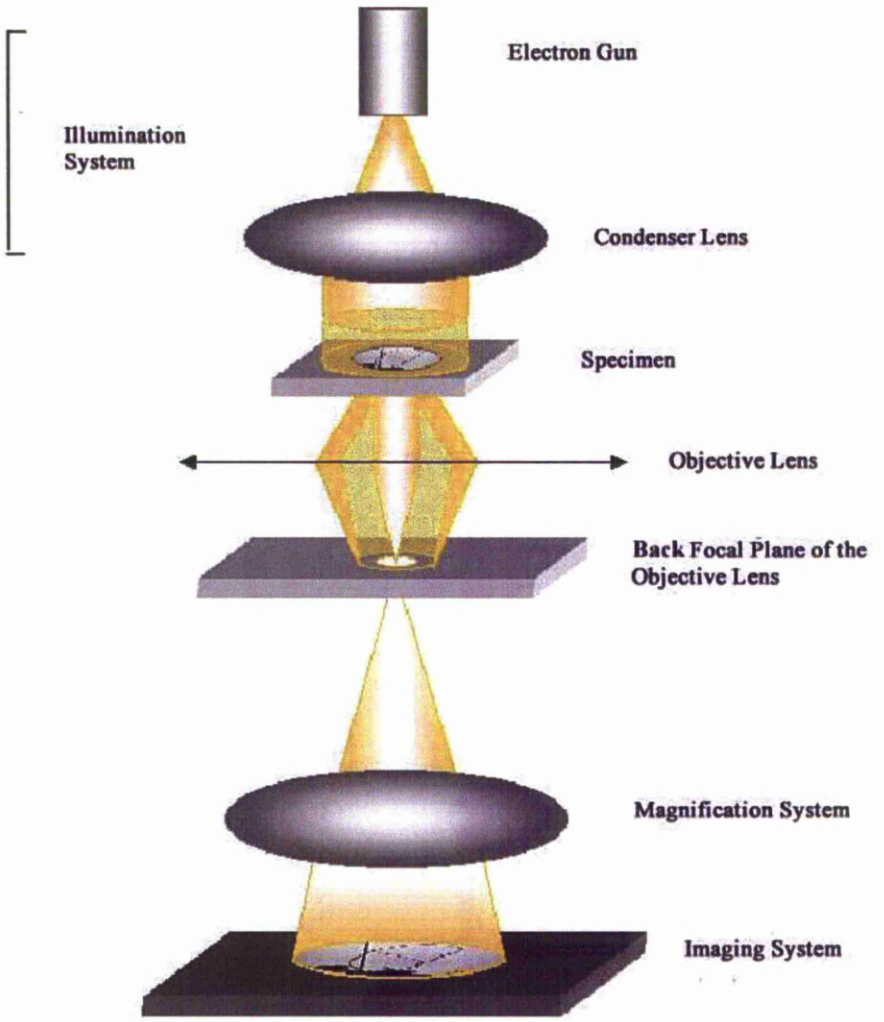


*Figure 2-1: Schematic diagram of a TEM in bright field mode.*

The specimen, generally supported on a grid, is accommodated in a sample holder and is transferred to the column via the specimen stage. Then the electron beam passes through the specimen and enters the objective lens, which is the most important part of the microscope in a TEM as it determines the limit of the image resolution. The beam electrons can interact with the sample in different ways and

incur elastic and inelastic scattering. The information electrons carry with them after passing through the sample depends strongly on the type of scattering they underwent during their interaction with the atoms of the sample. In HRTEM imaging, the elastic scattering is of interest. The scattered electrons are focused by the objective lens onto its back focal plane. The electrons scattered at the same angle (or by the same periodicity) are then focused at the same point at the back focal plane irrespective of the place in the sample where the interaction took place. If the image formed at the back focal plane is recorded, then the diffraction pattern is acquired. The electrons continue along their trajectory and at the first image plane, all that originate from the same point in the sample are focused at the same point. Since different electrons have travelled different optical paths due to their having undergone different scattering/diffraction with the sample, their interaction will provide the contrast in TEM images.

The magnification system consists of the intermediate and projection lenses, and it can provide magnification of several million times. Finally, the image is revealed onto a phosphour screen or can be visualized via a charge-coupled device (CCD) connected to a monitor. The image can be permanently recorded using a photographic plate or digitally via CCD camera.

All the lenses in the microscope are electromagnetic in nature except for the gun lens and energy prism where applicable and are affected to some extent by chromatic and spherical aberrations. These are phenomena that are inherent to round lenses, either optical or electromagnetic. Chromatic aberration stems from the fact that electrons with different energies are focused at different planes. Furthermore, chromatic aberration relates to the fact that electrons traveling off-axis, experience the inhomogeneous field of the lens, so that their wave-fronts are spherically distorted. Electrons that travel toward the outer part of the lens experience a stronger bending action by the magnetic field, given as $F=qvB\sin\theta$ where q is the charge, v is the speed, B is the magnetic field and $\theta$ is the angle between v and B, The electrons are thus focused on a plane above the back focal plane for those passing through the centre of the lens. Electromagnetic lenses can also be astigmatic: electrons sense a non-uniform magnetic field across different directions of the lens. These are the main aberrations that can distort the images and affect the resolution of the microscope. The term "resolution" indicates the minimum resolvable distance in the object, and is limited, in

principle, by the wavelength of the electrons, λ, and by the collection semi angle of the objective lens, β (the radius of the Airy disk: $r = a\frac{\lambda}{\beta}$). The practical resolution of a TEM is affected by the spherical aberration ($r \approx 0.91(C_s\lambda^3)^{\frac{1}{4}}$), where $C_s$ is the spherical aberration coefficient. The wavelength of the e-beam is normally too small to affect the microscope's resolution.

Two different operation modes of TEM imaging system are illustrated in Figure 2-2 [1]. A selected area diffraction (SAD) aperture is inserted onto the image plane of the objective lens in order to select a specific area of interest (which reduces the beam intensity falling on the screen). By changing the strength of the intermediate lens, either the SAD diffraction pattern or the image of the sample will be projected on to the screen or CCD.

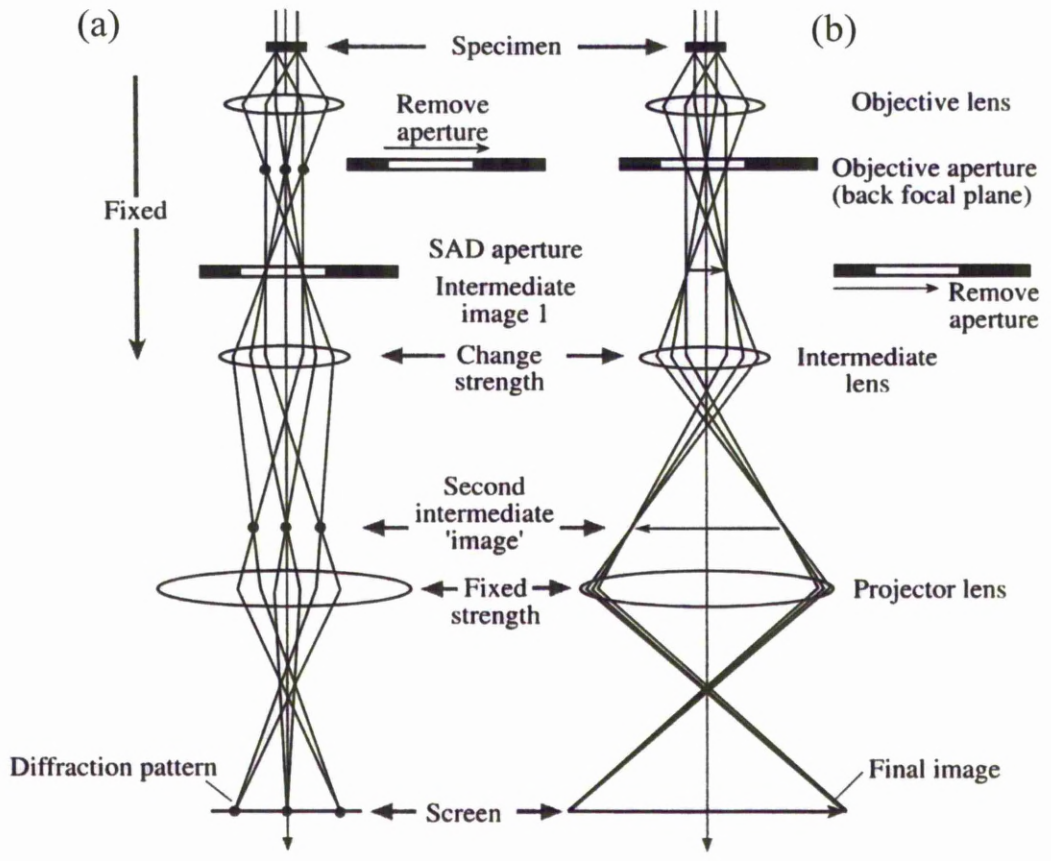


*Figure 2-2: Two different operation modes of TEM involving projection of (a) the diffraction pattern and (b) the image onto the screen [1].*

Samples for high resolution electron microscopy analysis are collected on holey carbon grids directly as floating flakes or by sprinkling a few droplets of powder sample dissolved in an organic solvent. The HRTEM analysis used in this study was carried out in several microscopes from the two pioneering microscopy microscopy companies: FEI and JEOL. A high resolution TEM serves two purposes; the first one is to examine nano-materials or thin films in terms of morphology, structure and size. The second one is to further analyze and identify the chemical composition of the particles of interest using mathematical models and conventional software.

An example of this practice is shown below. Using a JEOL 4000EX microscope operated at 400 kV with a point-to-point resolution of 1.9 Å and a resolution limit of 1.4 Å an image was captured depicting a particle which contains two phases. Selected areas of the high-resolution micrograph were digitized and the digital diffraction patterns (DDPs) were constructed applying a Fast Fourier Transform (FFT) on the image. Figure 2-3 illustrates a bilobar nanoparticle which consists of two different materials. By selecting an area in which the structure of the material is clearly defined, FFT was applied and the DDP reveals information about the lattice d-spacings (*d1, d2, d3*) and the angles ($\varphi$) between them. Ultimately, this leads to the crystallographic identification of the material. For this case, the smaller particle was found to be FePt and the larger one $FeO_3$.

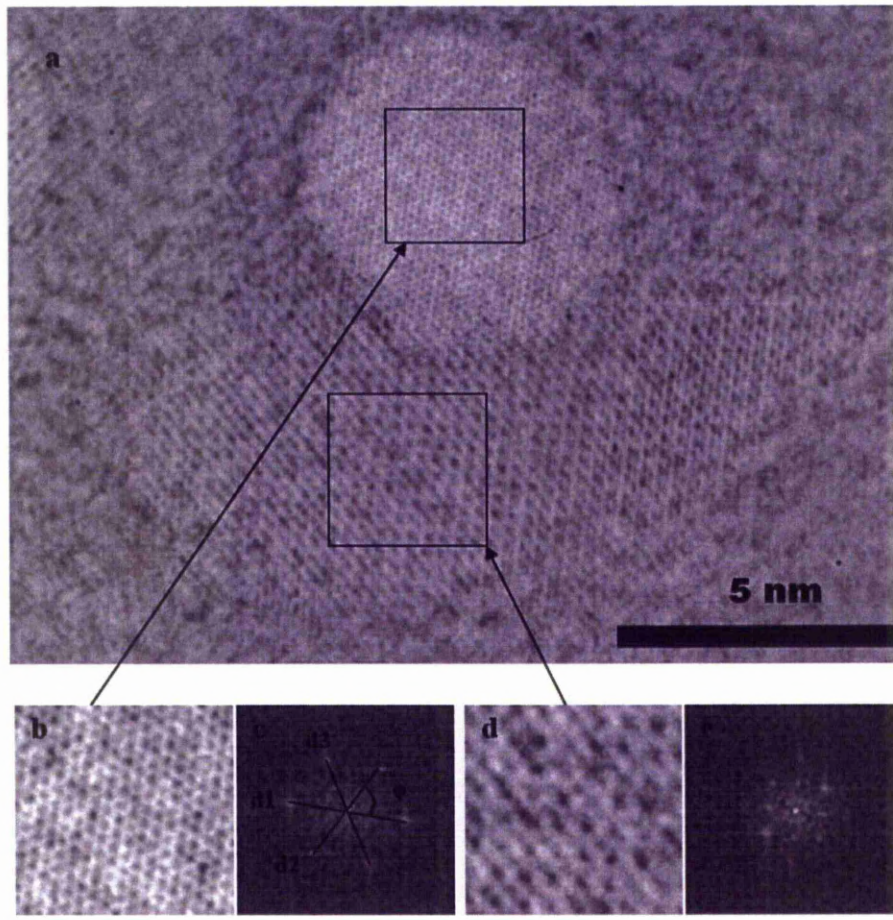


*Figure 2-3: a. HRTEM micrograph (inverted contrast). b. Selected area for FFT. c. DDP of selected area b. c. Selected area for FFT. d. DDP of selected area c*

In this approach the lattice d-spacings and the angles between the planes are measured with the highest accuracy from the DDP. The lattice parameters are then used for crystal phase identification through data comparison with crystallographic databases.

### 2.1.2. SCANNING TRANSMISSION ELECTRON MICROSCOPY (STEM)

A scanning transmission electron microscope (STEM) operated in the following manner. Electrons pass through the specimen, however, as in scanning electron microscopy, the electron optics focus the beam into a narrow spot which is raster-scanned over the sample. The raster-scan of the beam across the sample makes

these microscopes suitable for analytical investigations such as mapping by Energy Dispersive Spectroscopy (EDS) or electron energy loss spectroscopy. The image is formed using a High Angle Annular Dark Field (HAADF) detector.

The HAADF Imaging technique is based on the collection of scattered electrons using a annular dark-field detector (dough-nut shape). When the probe does not interact with matter, there are no scattered electrons and therefore all the beam passes through the open centre of the ADF detector which records zero signal for that point in the image. However, when the beam encounters atoms it will be scattered and the ADF detector will record a signal. Therefore, as the beam is rastered along the sample, the image is formed by spatially discrete levels of signal recorded by the ADF detector. The contrast of HAADF images is strongly dependent on the average atomic number of the atoms encountered by the incident probe as heavier atoms scatter more strongly. Spatial resolution is limited by the size of the focused incident probe and the intensity profile along it. In fact, atomic resolution imaging was first achieved in STEM by using an ADF detector to collect electrons scattered from heavy atoms supported on an ultra-thin, light-element substrate [2-4]. The high efficiency of the ADF signal made it possible to image individual atoms of heavy elements, and to study the motion and diffusion of atom clusters [5]. Atomic rows in small crystallites and different layers of atoms were also observed in ADFSTEM images, and for very small clusters, quantized levels of integrated intensity of atoms were observed [6-7].

The contrast of ADF images depends critically on the inner and outer collection angles of the ADF detector. The diffraction effects in ADF images of crystalline materials can be greatly suppressed by increasing the inner collection angle of the ADF detector beyond the Bragg reflections so that only high-angle scattered electrons contribute to the collected signal [8]. This new imaging mode is also called Z-contrast imaging. In HAADF images, the diffraction and phase contrast is significantly suppressed and the compositional sensitivity is recovered. The development of HAADF imaging technique has proved very successful for characterizing small particles and supported metal catalysts with sub-nanometer or atomic resolution and high compositional sensitivity [9-14]. Small metal particles supported on polycrystalline materials cannot be reliably detected in BF or low-angle ADF images because of the strong diffraction and phase effects, but these nanoparticles can be easily recognized in HAADF images.

EDS is a technique that is based on the characteristic X-ray peaks that are generated when an energetic electron beam interacts with the specimen. Each element produces characteristic X-rays that may be used to identify the presence of that element in the region being examined. Comparison of the relative intensities of X-ray peaks may be used to determine the relative concentrations of each element in the specimen.

The reason why modes of STEM-based techniques were used is because EDX is well suited for identifying the atomic composition of a material, is quite easy to use, and is particularly sensitive to heavier elements. HAADF imaging on the other hand, was chosen since the contrast difference between materials could assist on the identification of elements within a unique particle, as it will be demonstrated in later chapters.

### 2.1.3. X-RAY DIFFRACTION

X-ray diffraction is a proven technique for studying the crystalline structure of materials. X-rays are a form of electromagnetic radiation that have high energies and hence short wavelengths on the order of the atomic spacing for solids. When a beam of X-rays impinges on a solid material, a portion of this beam will be scattered in all directions by the electrons associated with each atom or ion that lies within its path.

X-rays are generated in a cathode ray tube by heating a filament to produce electrons, accelerating the electrons toward a target by applying a voltage, and bombarding the target material with electrons. When electrons have sufficient energy to dislodge inner shell electrons of the target material, characteristic X-ray spectra are produced. The specific wavelengths are characteristic of the target material (Cu, Fe, Mo, Cr). Filtering, by foils or crystal monochrometers, is required to produce monochromatic X-rays needed for diffraction. These X-rays are collimated and directed onto the sample. As the sample and detector are rotated, the intensity of the reflected X-rays is recorded. The diffraction of X-rays is due essentially to the existence of certain phase relations between two or more waves. These waves may constructively or destructively combine with each other depending upon their phase relationships. In order to get a constructive X-ray diffraction, Bragg's law must be obeyed [15]:

$$2d\sin(\theta) = n\lambda \tag{2.1}$$

Where:

$\theta$ is the angle between the incident beam and the crystal plane

$n$ is an integer number $\lambda$ is the wavelength of the incident X-ray

$d$ is the atomic spacing or in low angle scattering the spacing between two surface/interface planes.

A detector records and processes this X-ray signal and converts the signal to a count rate which is then output to a device such as a printer or computer monitor. The intensity of the diffraction pattern depends not only on how much each atom scatters the X-rays, but also on how those atoms are located with respect to each other in the crystal lattice. The structure factor F [16], which is related to the scatterings intensity of the respective atoms in the unit cell is given as:

$$F = \sum_{m=1}^{N} f_m e^{2\,i\,\pi\,(K\cdot\,r_m)} \tag{2.2}$$

Where:

The term $f_m$ (lattice: $f_m = m_1a + m_2b + m_3c$) is the scattering from a single atom in the unit cell.

vector $\boldsymbol{r}_m$ represents the position of a general atom in the unit cell relative to a lattice point (atom unit cell $r_m = x_n a + y_n b + z_n c$).

The sum is hence taken over all atoms in the unit cell.

K is the reciprocal lattice vector which is identified by the miller indexing (hkl) [17].

In general, $F$ is a complex number, and it expresses both the amplitude and phase of the resultant wave. Its absolute value, $|F|$, gives the amplitude of the resultant wave in terms of the amplitude of the wave scattered by a single electron. The intensity of the beam diffracted by all atoms of the unit cell in a direction predicted by the Bragg's law is simply proportional to $|F|^2$.

The relationship in Equation 2.2 gives some restrictions to the possible reflections so that some peaks are 'forbidden' because the diffraction from those planes results in a zero structure factor. For example, the allowed reflections for body centered cubic (bcc) structure must satisfy:

$$h+k+l = even \tag{2.3}$$

Possible Bragg reflections are (110), (200), (112) etc. and for face centered cubic (fcc) structure, it must satisfy:

$$h,k,l \ \ all\ even\ or\ all\ odd$$

Possible reflections are (111), (200), (220) etc.

XRD shows more global structural properties due to the large beam diameter as compared with the selected area diffraction (SAD) method in TEM, which provides localized information of the crystal structure.

The angular spread of the reflection from a crystal plane is affected by several factors, such as the particle size, the strain effect, or the defects inside the material. Scherrer's formula [17] can be used to estimate the average particle size, $D$, from the full width half maximum (FWHM) of the peak:

$$D = \frac{K\lambda}{\beta\cos(\theta)} \tag{2.4}$$

Where: $K$ is a constant ranging between 0.89 and 1 (usually a value of 0.9 is used)

$\lambda$ is the wavelength of the incident x-ray

$\theta$ is the Bragg angle and $\beta$ is the FWHM of the diffraction peak in radians.

As the average size of the crystallites decreases, the angular spread of the reflection from a particulate system will increase. After a suitable calibration, the FWHM of a diffraction pattern can be used as a quantitative measure of the mean particle size of the sample.

Powder XRD is a very common way of characterizing materials. Fine grains of single crystalline powder are an ideal material to be studied. However, the technique is used also for studying particles in liquid suspensions or polycrystalline solids; bulk or thin film materials.

The term "powder" really means that the crystalline domains are randomly oriented in the sample. Therefore, the 2-D diffraction pattern shows concentric rings of scattering peaks corresponding to the various d-spacings in the crystal lattice. The

positions and the intensities of the peaks are used for identifying the underlying structure or phase of the material. For example, the diffraction lines of graphite would be different from diamond even though they both are made of carbon atoms. This phase identification is important because the material properties are highly dependent on structure.

Powder diffraction data can be collected using either transmission or reflection geometry, as shown in Figure 2-4. Because the particles in the powder sample are randomly oriented, these two methods will yield the same data. In the MRL x-ray facility, powder diffraction data are measured using the Philips XPERT MPD diffractometer, which measures data in reflection mode and is used mostly with solid samples, or the custom built 4-circle diffractometer, which operates in transmission mode and is more suitable for liquid phase samples.

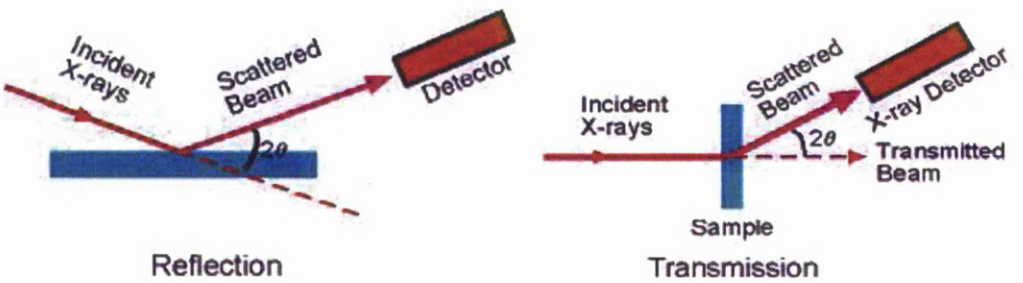


*Figure 2-4: Data collection methods; Reflection geometry (left) or Transmission geometry (right) [18].*

### 2.1.4. X-RAY PHOTOELECTRON SPECTROSCOPY (XPS)

X-Ray photoelectron spectroscopy (XPS) is a very commonly used method of surface analysis in materials science and chemistry. It provides valuable information of the atomic composition of the specimen as well as other chemical data, such as binding constants and oxidation states. The sample is radiated by a high energy X-ray source and the X-rays penetrate into a surface depth of 5 to 100 Å into the sample. As the atoms absorb the X-rays, the electrons in the lowest energy level will be ejected.

At that point, the kinetic energy (KE) of the electron is related to the energy of the incident beam (hν), the electron binding energy (BE), and the work function of the spectrometer ($\phi$ ).

$$BE = h\nu - KE - \varphi_s \qquad (2.5)$$

Thus, the binding energy of the electron can be calculated. The binding energy of the ejected electron is unique for each element and the number of electrons detected with the characteristic binding energy is proportional to the number of corresponding atoms in the particular specimen, taking into consideration the effective cross section. This information leads to an estimate of the percentage concentration of each atom in the sample. XPS analysis is also used to determine any surface composition as well as surface contamination (mainly detected as carbon peaks), chemical or electronic state of each element in the first few nanometers in depth and the uniformity of elemental composition across the surface.

Initially this technique was developed for the examination of thin, flat films; however XPS can also be performed in powder form samples. The sample preparation for powder examination differentiates from that for thin films. Usually, the powder should be pressed onto a high purity indium foil. Another way is to dissolve the powder in a quickly evapourating solvent which can then be drop-cast onto a substrate. This approach is not always possible since some powders cannot or should not be dissolved. For such cases, the powder is stuck to a disc or a tablet in order to keep the sample compressed, compact and completely dry. If not, the powder will contaminate the vacuum chamber by destroying the high vacuum and affecting the data of the current and future samples.

In this study, the capabilities of XPS analysis were widely used for the materials in powder form. The photoemission experiments were carried out in an ultra-high vacuum system (UHV) which consisted of a load lock assembly, a sample preparation and an analysis chamber. The base pressure in both chambers was $1 \times 10^{-9}$ mbar. Unmonochromatized Mg K$\alpha$ line at 1253.6 eV and an analyser pass energy of 97 eV, giving a full width at half maximum (FWHM) of 1.7 eV for the Au $4f_{7/2}$ peak, were used in all XPS measurements.

### 2.1.5. LUMINOUS ACTIVITY OF THE ARC-DISCHARGE: OPTICAL EMISSION SPECTROSCOPY (OES) & HIGH-SPEED IMAGING

In order to have a complete view of the whole arc-discharge experiment, a very important diagnostic tool, namely Optical Emission Spectroscopy was attached to the experimental set up. OES was used to investigate the active species, atoms, ions and molecules within the plasma. This method can provide differing information regarding the quantitative determination of major and trace elemental constituents in the plasma, the qualitative elemental analysis of elements, the densities of the species and their energy distribution.

The luminous activity of the discharge was studied by side-on observations through fused-silica UV viewports attached to the side of the container and centred to the inter-electrode gap (see Figure 2-9). The window was faced by a photomultiplier tube, PMT, R928 Hamamatsu Ltd. The evolution of the total light emission intensity, integrated over the interval of the emitted wavelengths, was registered by focusing a spot of 1 mm on the emissive photocathode which was type multialkali, 185-900 nm.

Moreover, the spectral emission of the arc was analysed through the second window using a 1/4 imaging spectrometer (MS260i Oriel Ltd). A ruled motorized grating (600 $lmm^{-1}$, blaze 400 nm, 250–1000 nm) was utilized as the dispersive device. The detector was an ICCD Andor$^{TM}$ camera; W-type photocathode, P43 phosphor, 185–850 nm. The wavelength calibration of the system was done with Pen-Ray® lamps. Figure 2-5 shows the spectral efficiency of the OES system, as it was calibrated in the laboratory ambience and demonstrates its influence on later arc spectra. The spectral efficiency was hard to calibrate due to the variable percentage of the nanoparticles (NPs) in the water as the discharge progressed. Thus, the OES was used only for line/band identification.

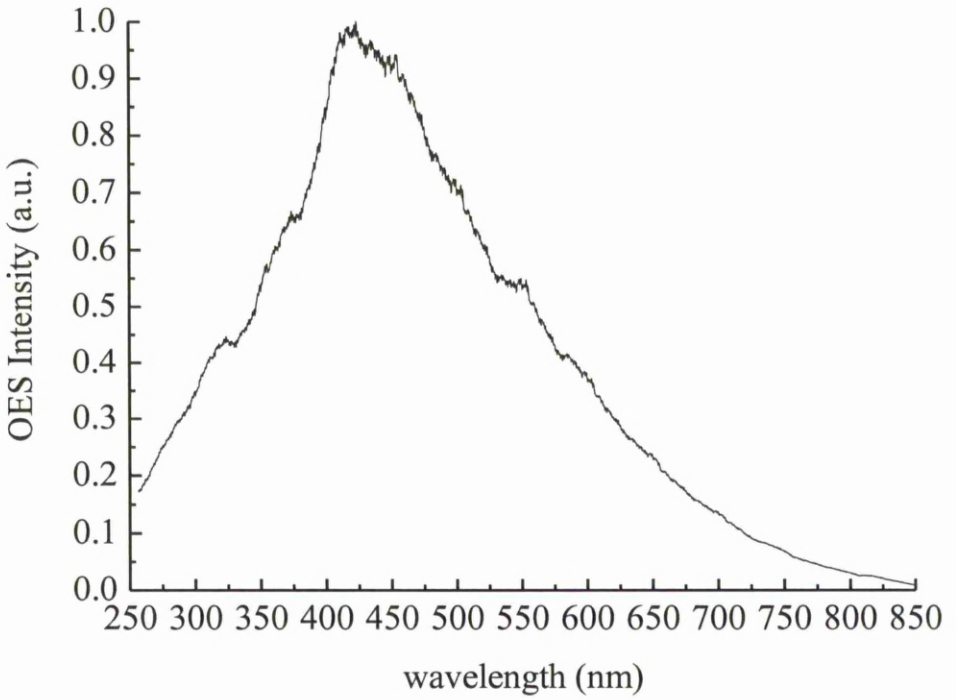


Figure 2-5: *Response of the optical spectrometry system to a tungsten halogen lamp (3300°K).*

Moreover, snapshots from the arc-discharge were recorded by means of high-speed imaging. An Ultima-APX Photron Ltd video camera system with an IEEE1394 interface was used. The camera was set to capture images from the ignition of the arc till its extinction. A better understanding of the plasma behaviour would be derived by following the process from start to finish.

For time-resolved measurements, both the spectrometer and the video system were triggered by 74LS74 TTL signals synchronized with the first negative edge of the inter-electrode voltage. Figure 2-6 presents the home-made circuit where the arc voltage is probed by a resistive divider and the attenuated signal is used to latch a positive-edge-triggered D flip–flop.

Finally, the evaporated mass of the electrodes was measured with a microbalance (A&D Instruments Ltd.) and the evaporation-arc time was accurately measured on the oscilloscope. Three sets of measurements were repeated to provide a mean value and a standard deviation for the evaporation rate (mgr/s). Observations on

the electrodes were performed by customary optical microscopy (Veho discovery vms-004 delux).

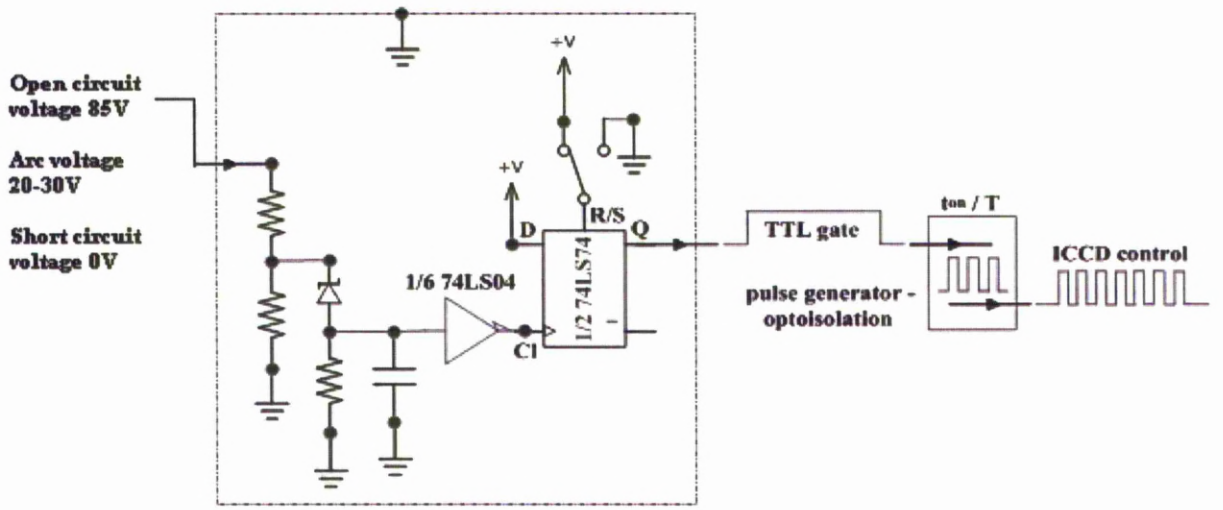


*Figure 2-6: TTL triggering circuit*

### 2.1.6. IN-SITU ELECTRICAL MEASUREMENTS OF THE ARC-DISCHARGE

The inter-electrode voltage was measured with a 100:1 voltage probe (P5100, 250 MHz) attached on the anode. For measuring the discharge high current, the grounded return lead of the cathode was shunted to three identical copper branches and the jaw of a Hall-effect current probe (TCP0030, 120 MHz) was clamped on one of them. Both voltage and current waveforms were monitored on a digital oscilloscope (DPO3000, 300 MHz - 2.5 GSamples/s) and saved on a personal computer through the oscilloscopes' interface. The electrical measurements of the open circuit operation are shown in Figure 2-7.

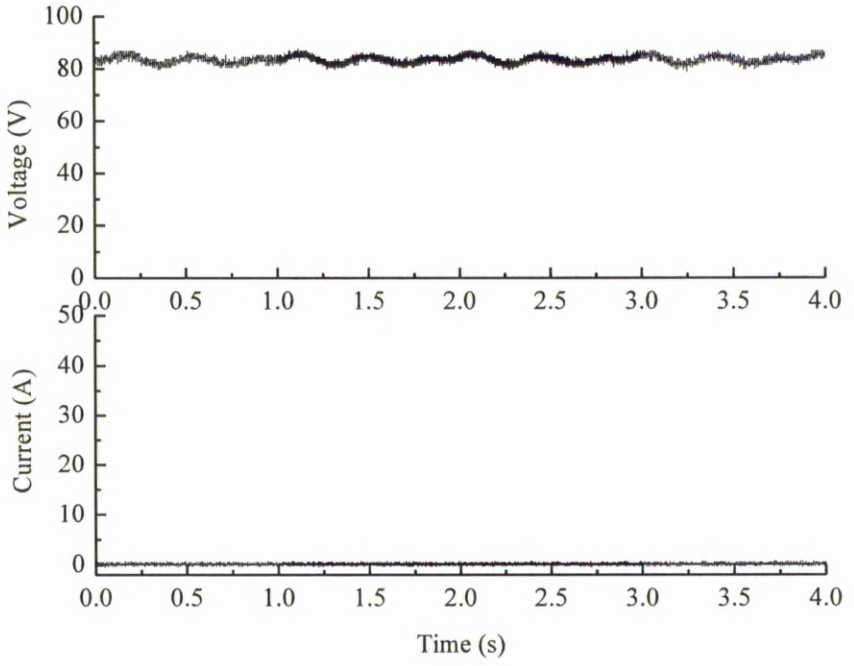


*Figure 2-7: Electrical characteristics of the power supply in open circuit operation.*

## 2.2. ARC-DISCHARGE IN DE-IONIZED WATER

### 2.2.1. EXPERIMENTAL SET UP

For this project a new vertical arc-discharge system was designed and constructed as shown in Figure 2-8. This system was intended to provide better stability and accuracy during the arc discharge, together with higher production rate of nanoparticles. The upper holder has manual up and down motion whereas the cathode is initially adjusted and aligned with the anode and remains stable throughout the duration of the arc-discharge.

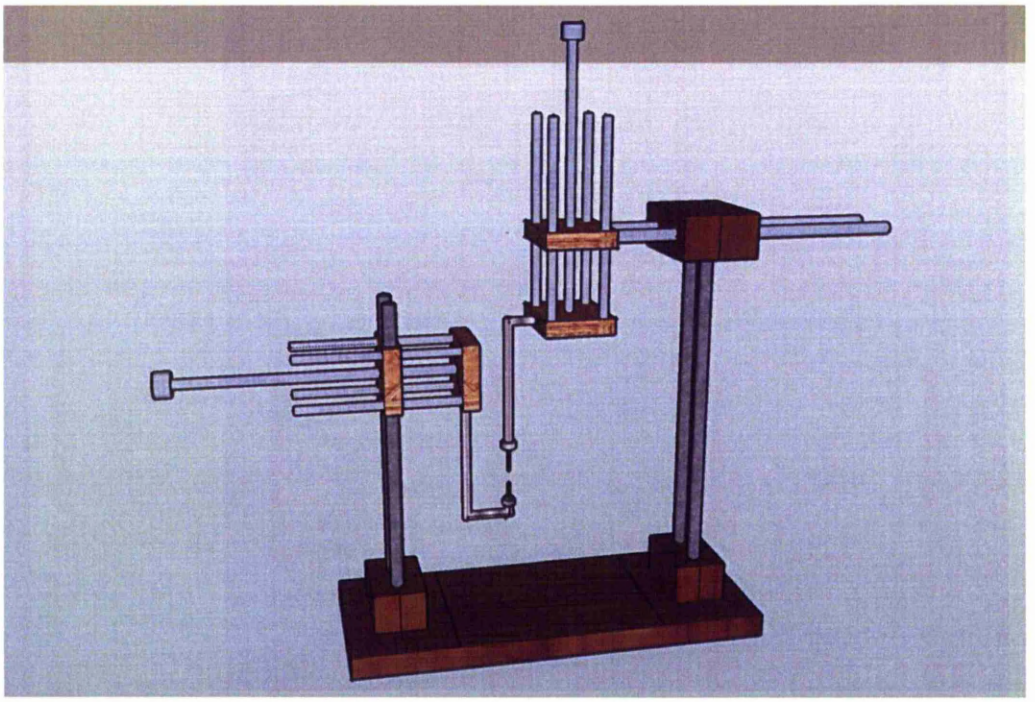

*Figure 2-8: Design of the vertical arc-discharge system*

A sketch of the system and the diagnostic devices attached to it, are presented in Figure 2-9. A plexiglass™ container was filled with de-ionized water (Acros Organics) and two electrodes were immersed. The first electrode, the anode, was either a Ø6.35 mm aluminium rod (99.95 %, Erodex Ltd.), or tantalum rod with Ø5 mm (99.99 %, Erodex Ltd.) or a mixture of copper and tantalum powder grains (1-5 microns 99%) compressed in a metal holder to form a solid uniform content.

All anodes were biased by a high-current DC power supply (Migatronic Tig Commander 400 AC/DC). The open-circuit voltage of the power supply was ~83 V and the arc current was stabilized at preset values (herein 15 to 60 A). The second electrode, the cathode, was Ø6.35 mm graphite rod (99.95 %, Alfa Aesar Ltd.) directly grounded.

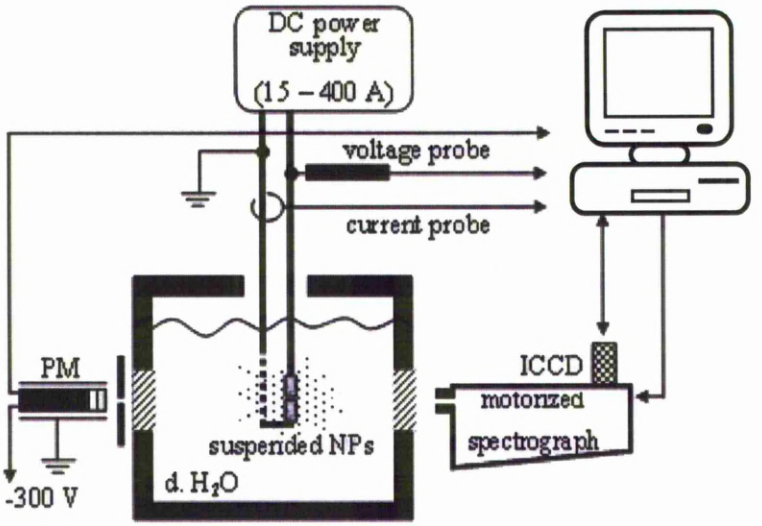


*Figure 2-9: General view of the experimental set up.*

Both electrodes were installed on a 2D manual translation stage for electrode alignment and gap adjustment. The NPs were collected by decanting the suspended material to beakers while avoiding the collection of sentiment. The water was eventually evaporated (~90 °C) and the NPs were collected in powder form.

## 2.3. INITIAL FINDINGS

### 2.3.1. HIGH-*K* DIELECTRIC POWDER

High-*k* dielectric powder was provided by BAE systems, both in pure form and as a mixture of dielectric resin and powder. The exact composition of the powder was not known, but only the elements. It consisted of calcium, bismuth, titanium and oxygen.

The dielectric constant of the pure powder was measured at 200 whereas that of the resin was measured about 7. Composites with 70% vol. concentration in $CaBiTiO_x$ show a dielectric constant of about 40. However, the high-*k* dielectric powder was available in grains whose size varies from few micrometers (μm) to

hundreds of μm. The arc discharge in water method was chosen to break these micro-grains into nanoparticles.

### 2.3.2. INVESTIGATION OF THE PURE POWDER GRAINS

In order to understand the nature of the powder, Scanning Transmission Microscopy (SEM) imaging was performed to give the results shown in Figure 2-10 (a), (b). The grains were shown to have a complex structure. The particles were micron-sized and spherical, with the surface of each grain comprising of smaller components, creating a brick-like outer wall.

TEM and HRTEM investigation was conducted in order to study the morphology of the original powder. Figure 2-11 (a), (b) and Figure 2-12 (a), (b), illustrate grains of the dielectric powder. Even though the powder appears to be a thick crystalline material, thin areas were found which allowed for HRTEM analysis. The data provided evidence of polycrystalline structure for this material.

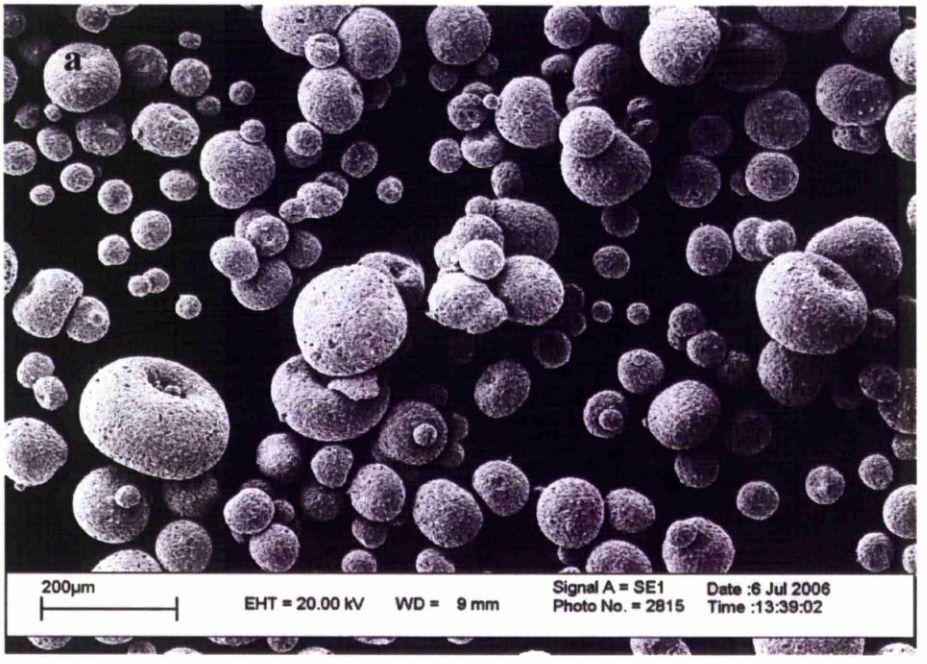

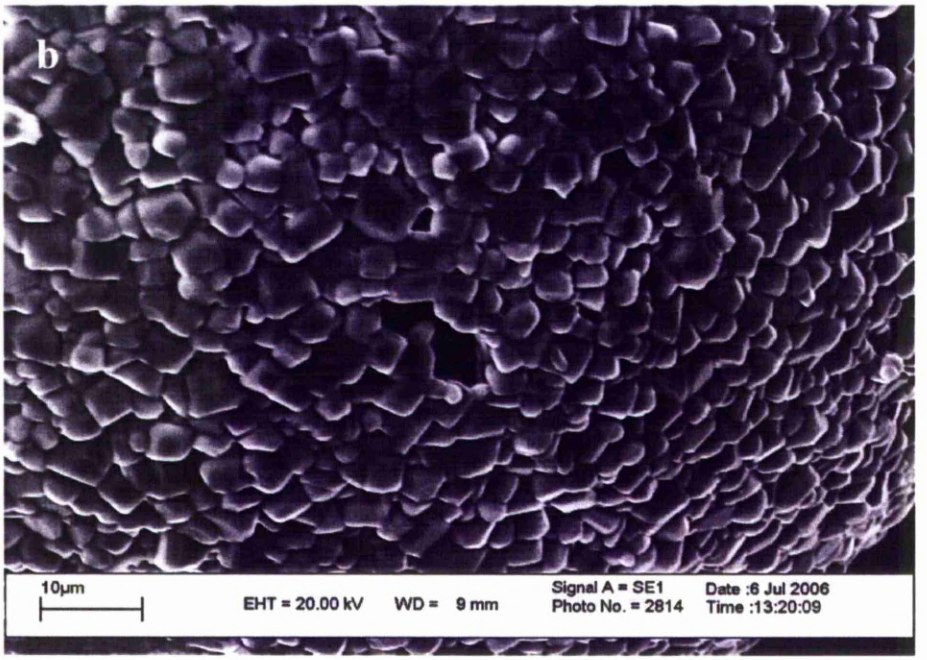


*Figure 2-10: (a) Low magnification SEM micrograph a. of grains of the high-k dielectric powder and (b) focused on the surface of an individual grain*

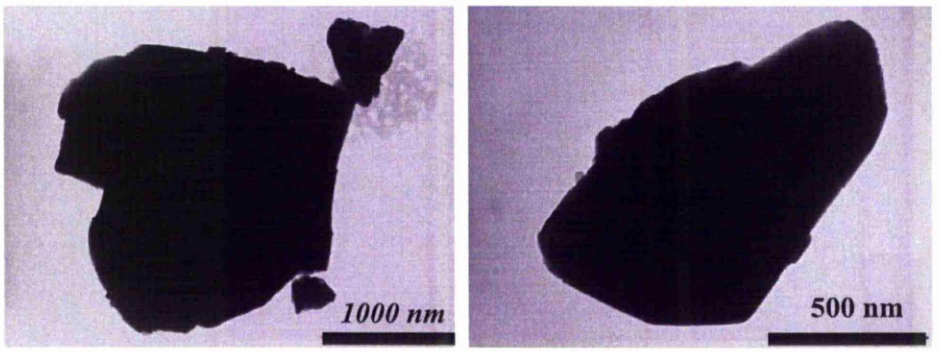


*Figure 2-11: (a), (b) TEM images illustrating grains of the high-k dielectric powder.*

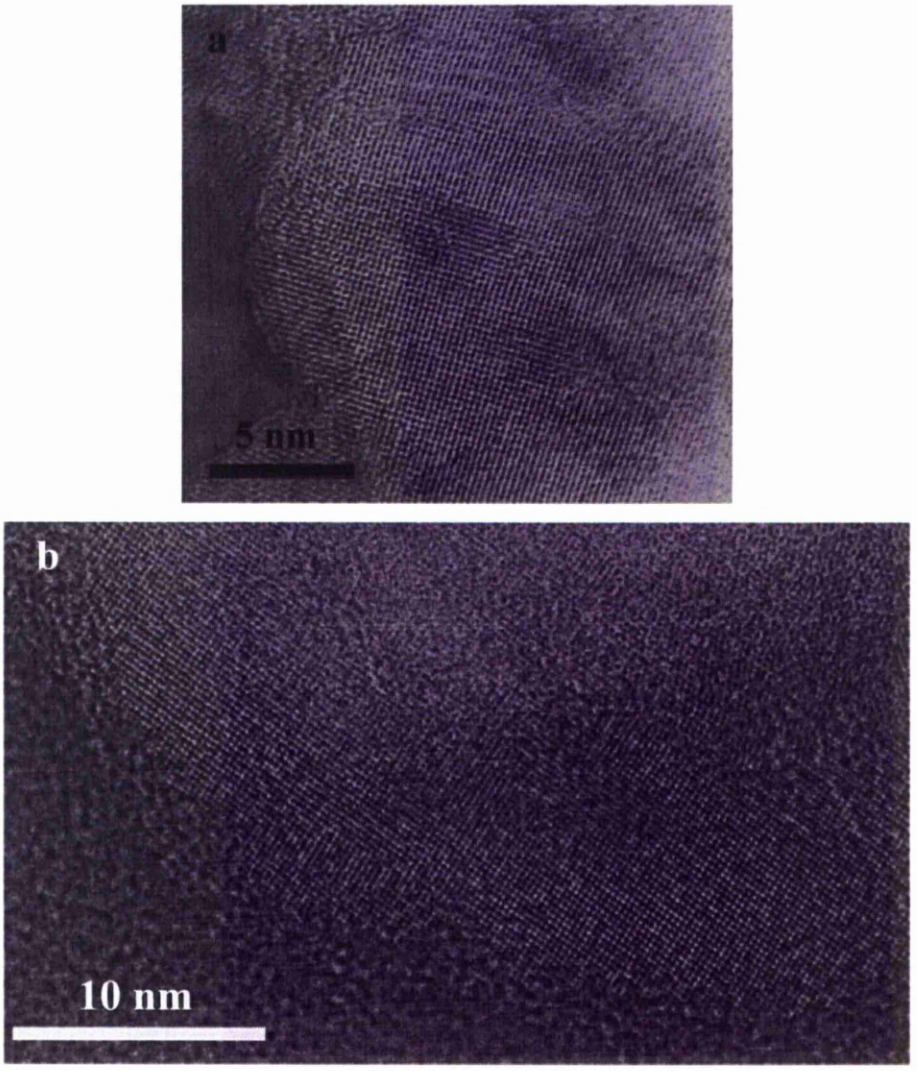


*Figure 2-12: (a), (b) HRTEM micrographs show the crystalline structure of the dielectric powder*

As well as microscopy observations, elemental composition of the initial powder was investigated using EDS. A typical EDS spectrum is portrayed as a plot of x-ray counts vs. energy (in keV). Energy peaks correspond to the various elements in the sample. The atomic elemental counts here, showed ratios 42.6% O, 18.21% Ca, 25% Ti and 3.15% Bi. Cu (9.6%) is thought to exist due to the holey carbon, copper grid which hosts the sample.

### 2.3.3. Formation of Dielectric Nanopaticles From $CaBiTiO_x$ Using The Arc-Discharge in Water Method.

This method was initially used for conductive materials where the current would easily flow from one electrode to the other. However, a dielectric would restrict the current flow so conductive materials needed to be installed on both electrodes. Pure $CaBiTiO_x$ powder was enclosed in an aluminium tube. Al was selected because it is a conductive metal and after the arc-discharge process it could appear as $AlO_x$ which has dielectric properties. The DC current, which was set at 30 A, flowed between the tube and a carbon electrode creating plasma at the vicinity of the $CaBiTiO_x$ high-k dielectric. The energy flux created leads to erosion of the dielectric into the form of nanoparticles. The schematic diagram of the system can be seen in Figure 2-13. The suspended product was collected after the evaporation of the water.

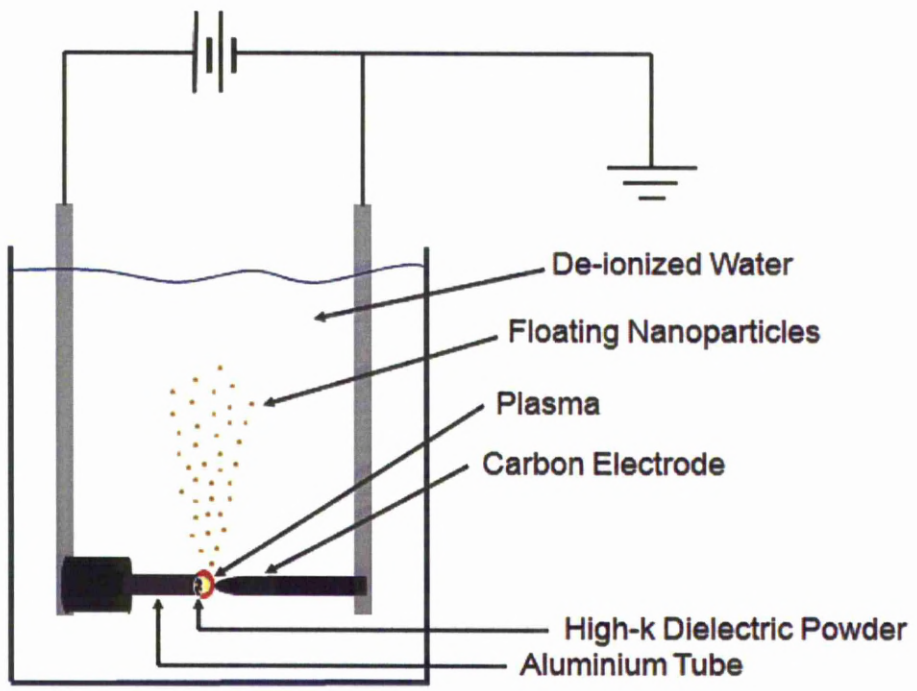


*Figure 2-13: Schematic of arc discharge in water method*

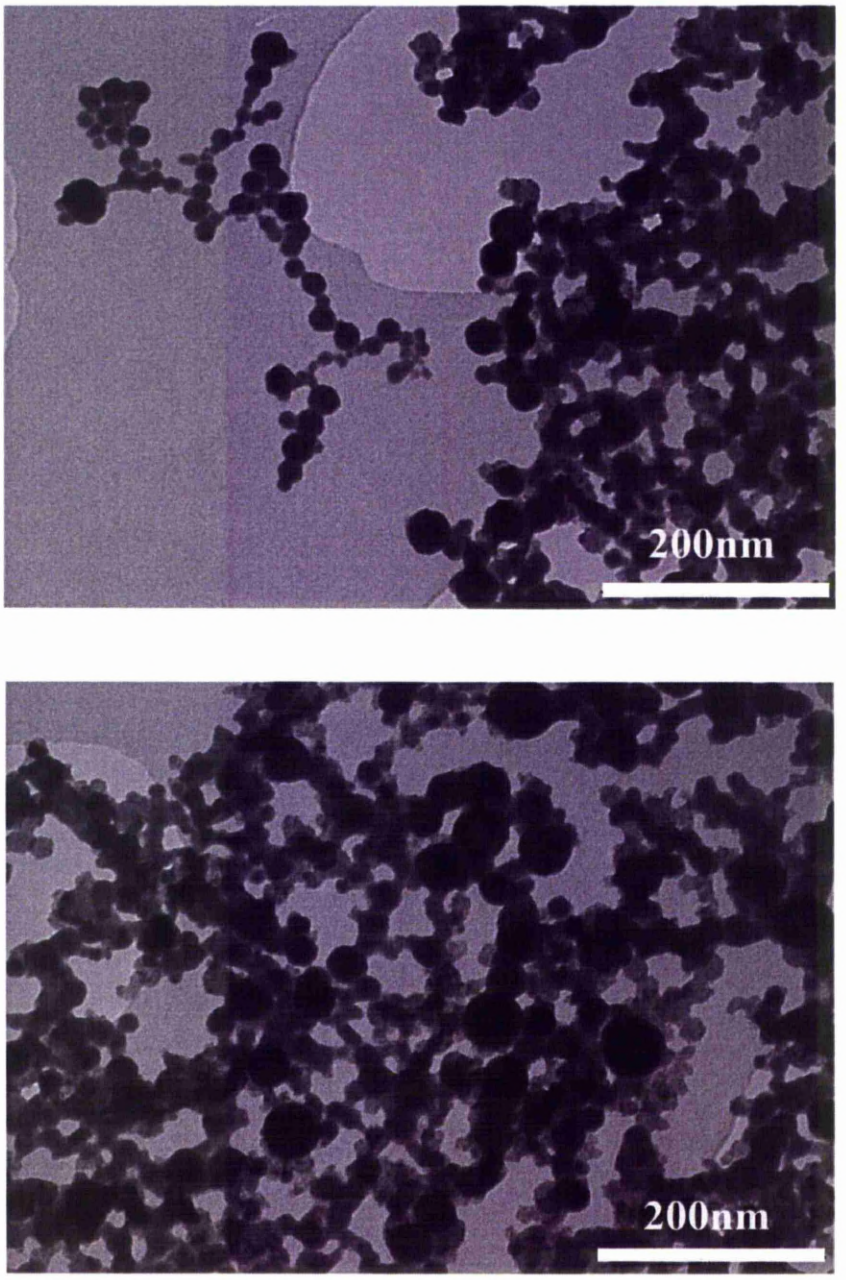


*Figure 2-14: Low resolution TEM images of a network-like structure of the produced material Average particle size at 40nm.*

TEM imaging showed particles with an average size below 50 nm encapsulated in an amorphous network as shown in Figure 2-14. Detailed HRTEM revealed that the structure of the material is poly-crystalline. An amorphous matrix surrounded as well as bonded the crystalline nanoparticles together, as shown in Figure-2-15.

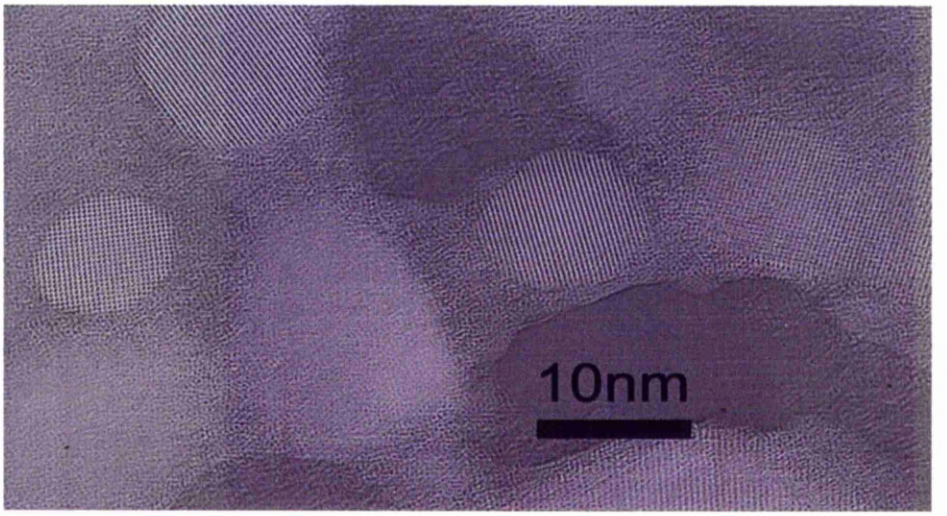


*Figure-2-15: HRTEM micrograph reveals that the network consists of crystalline nanoparticles embedded in an amorphous matrix.*

However, one of the main issues was the composition of these nanoparticles. EDS Element mapping was performed to identify the constituent elements of the nanoparticles after the arc exposure. An element map is an image showing the spatial distribution of elements in a sample. Element maps are extremely useful for displaying element distributions in textural context, particularly for showing compositional arrangements. The image is produced by progressively rastering the electron beam point by point over an area of interest. Element map can be considered as a pixel by pixel image based on chemical elements. Resolution is determined by beam size, and the relative response of each element is determined by the duration within which the beam dwells on each point; that is, the actual concentration of material exposed. Greater distinction can be made by longer analysis, but at the cost of time.

Initially, all the elements that were included in the arc process appeared in the final product. Aluminium, a bi-product of the process, was found in the form of metal oxide ($AlO_x$) crystalline nanoparticles. The elements of the high-k dielectric (Ti, Ca, Bi and O) look to be mainly concentrated in the amorphous matrix, as shown in Figure 2-16.

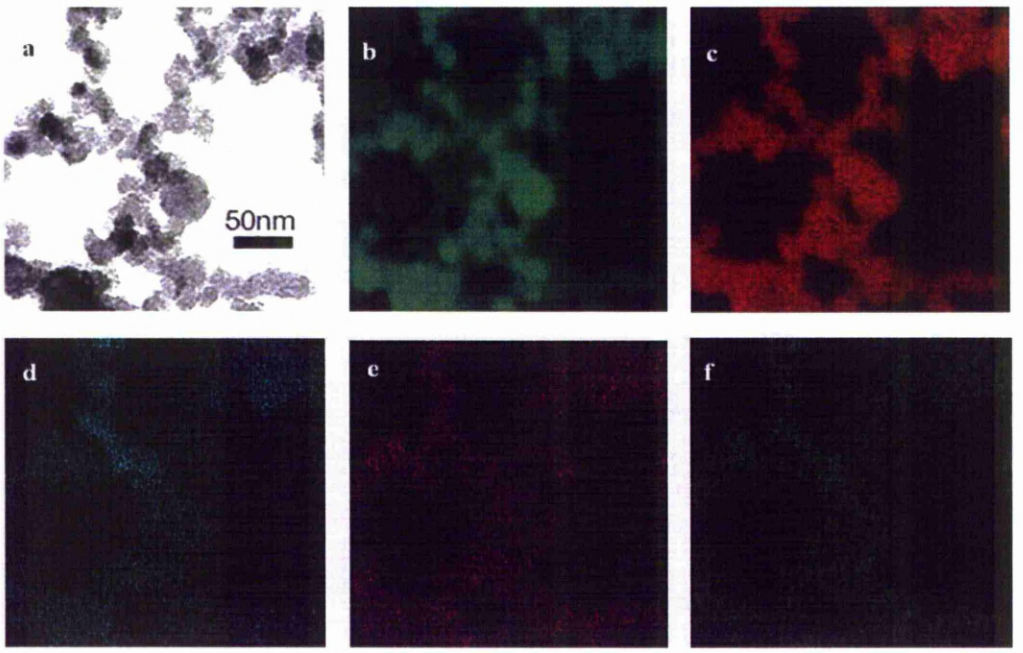


*Figure 2-16: a. STEM micrograph b. Aluminium c. Oxygen d. Titanium e. Calcium f. Bismuth*

### 2.3.4. SUMMARY

The presented advanced diagnostic tools and characterization techniques along with these initial findings generated the idea of testing the production of metal oxide (dielectric) NPs using the arc-discharge in water method. Up to that point, it became apparent that the discharge between an aluminium anode and a carbon cathode could create aluminium oxide NPs. The exact composition of the resulting particles was not determined however, EDS mapping showed no significant impurities acquired from the cathode. One step further in that direction was to test composite metals in order to form high purity and with increased production rate high-k dielectric NPs. Moreover, the physics behind the growth mechanism of the dielectric powders was also considered to be within the scope of this project.

## 2.4. REFERENCES

[1] D. B. Williams and C. B. Carter, Transmission Electron Microscopy: A Textbook for Materials Science, Plenum Press, New York, (1996)

[2] C. Kittel, Introduction to Solid State Physics, Wiley, New York. (1996)

[3] N. W. Ashcroft and N. D. Mermin, Solid State Physics, Saunders (1976).

[4] A. V. Crewe, J. Wall, J. Langmore, *Science* 168 ,1338 (1970).

[5] A. V. Crewe, J. Wall, *J. Mol. Biol.* 48, 373 (1970).

[6] A. V. Crewe, *Rep. Progr. Phys.* 43, 621 (1980).

[7] M. Isaacson, D. Kopf, M. Utlaut, N. W. Parker, A. V. Crewe, *Proc. Natl. Acad. Sci.*, 74, 1802 (1977).

[8] M. Isaacson, D. Kopf, M. Ohtsuki, M. Utlaut, *Ultramicroscopy*, 4, 101 (1979)

[9] M. Ohtsuki, *Ultramicroscopy,* 5, 325 (1980).

[10] A. Howie, *J. Microscopy* 117, 11. (1979).

[11] M. M. J. Treacy, A. Howie, C. J. Wilson, *Philos. Mag.* 1978, A38, 569 (1978)

[12] M. M. J. Treacy, S. B. Rice, *J. Microscopy* 156, 211 (1989).

[13] J. Liu, J. M. Cowley, *Ultramicroscopy* 34, 119 (1990).

[14] S. B. Rice, J. Y. Koo, M. M. Disco, M. M. J. Treacy, *Ultramicroscopy* 34, 108 (1990).

[15] S. A. Bradley, M. J. Cohn, S. J. Pennycook, *Microsc. Res. Tech.* 28, 427 (1994).

[16] R. Narayanan and S. Ramaseshan *Acta Crystallographica Section A*, 37, 636 (1981).

[17] P. D. Nellist, S, J, Pennycook, *Science* 274, 413 (1996).

[18] J. A. Nielsen and D. McMorrow, Elements of Modern X-ray Physics, John Wiley & Sons, Ltd., (2001).

# 3. ALUMINIUM OXIDE NP PRODUCTION

## 3.1. ALUMINIUM OXIDE GENERAL BACKROUND

Aluminium oxide ($Al_2O_3$), commonly named as alumina, is a ceramic material and is used in the field of electronics as an electrical insulator for the gates of field effect transistors and also in capacitors. It has a dielectric constant of almost 10, a band gap of 7 eV and a relatively high thermal conductivity (30 $Wm^{-1}K^{-14}$). Aluminium oxide can be found in many different forms (beta, delta etc.) however, the most common ones are alpha-aluminium oxide ($\alpha$-$Al_2O_3$) and gamma-aluminium oxide ($\gamma$- $Al_2O_3$). $\alpha$- $Al_2O_3$ is the most stable crystalline form (also known as corundum) and can be found in nature. $\gamma$-$Al_2O_3$ transforms to $\alpha$-$Al_2O_3$ at high temperatures.

High purity alumina is one of the strongest and stiffest oxide ceramics rendering this material usable for a variety of applications. Abrasion resistant tubes, thermometry sensors, sample holders, seal rings, cutting tools, high temperature and high voltage electrical insulators as well as electronic substrates are just a few examples of the numerous applications of this metal oxide. In nanotechnology, $Al_2O_3$ is widely used in thin films as a dielectric. It can be used as a gate dielectric layer on its own or combined with other materials such as silicon dioxide, to form bi-layers, to enhance the properties of a film. In addition, polymer/aluminium oxide nanoparticle (NP) composite films are easy to fabricate for the same purpose, finding application in organic electronics.

Pure aluminium metal can be easily transformed to its metal oxide when it comes with contact with oxygen. Taking advantage of previous referred experiments with arc discharge in water, the goal was to create aluminium oxide NPs from its raw material after performing high temperature plasma during discharge in water environment. The oxidization properties combined with the dissociation of water ($H_2O$) molecules create the appropriate conditions to synthesize aluminium oxide atoms and consequently NPs. The proposed production mechanism will be discussed in detail at the end of this chapter.

## 3.2. DISCHARGE CHARACTERISTICS

### 3.2.1. ELECTRICAL CHARACTERISTICS

The first goal was to produce dielectric NPs by arc-discharge in de-ionized water using an aluminium rod as an anode and a graphite rod as a cathode. In order to find the optimum conditions, in terms of particle size uniformity and arc stability three different current densities were tested (15 A, 35 A and 60 A).

Figure 3-1 shows the electrical characteristics as well as the emitted light intensity during an aluminium arc at 35A.

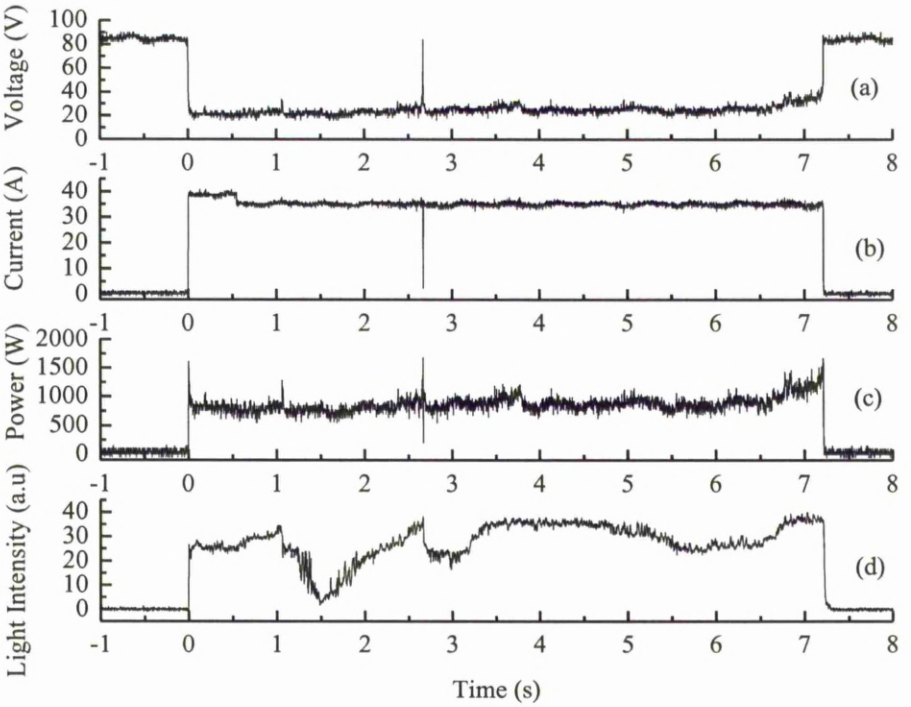


*Figure 3-1: Electrical characteristics and luminous activity of the arc-discharge in water using an aluminium rod as anode.*

In Figure 3-1 (a) and (b), typical time dependent current and voltage waveforms for the arc-discharge in water are presented. Initially, when the electrodes are not in contact, the gap voltage is equal to the open-circuit voltage, ~ 85 V. As

soon as the electrodes are brought into contact, the current increases and stabilizes to the preselected value (here 35 A) in the first 10 ms, (see Figure 3-2) consistent with the current source concept. Inevitably, the electrode surfaces have imperfections (roughness). The current starts to flow through these projected points, but liquid breakdown and electron avalanches are further induced by various processes [1, 2]. The local heating and electrolysis generates vapour and, progressively, space charge is created and sustained by ionization impacts between energetic electrons and neutrals in the vapour phase [2]. Self-maintaining plasma surrounding the electrodes is established and the current is constant even when the electrode gap starts to grow due to thermal evaporation.

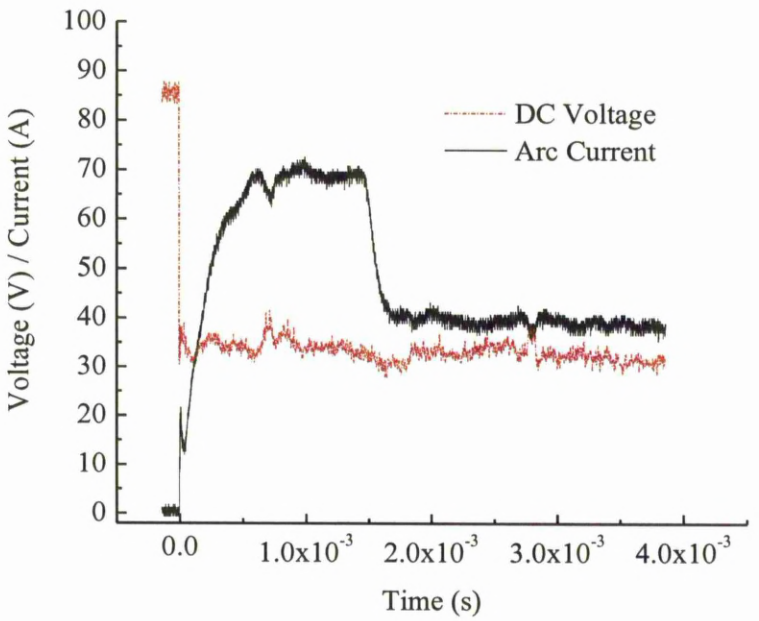


*Figure 3-2: The first 4 ms of the arc-discharge.*

The voltage (Figure 3-1 (a)) is reduced from ~ 85 V to fluctuating values (indicative 20 to 30 V). The operation voltage and current of this discharge in water are similar to those of its counterpart in gas [3, p 189]. The cathode current density (J = I / A), where I is the selected current and A is the area of the electrode is roughly calculated at 35 A/[$\pi$/0.635/2 cm$^2$] $\approx$ 110 A·cm$^{-2}$, which is a value slightly higher than the lower limit of an arc-discharge range [4, p 245]. Therefore the term arc-discharge

used here is justified. Furthermore, it could be assumed that the plasma produced is potentially close to equilibrium, taking into account previous studies as shown below; that is thermal plasma [5], because of the working pressure. The plasma of air, other molecular gases and metal vapour at pressure higher or equal to 1 Atm are in equilibrium at practically any current [4, p 272]. The equilibrium is caused by intensive energy exchange between electrons and molecules through excitation of vibrational and rotational modes and by large elastic scattering cross sections of electrons in metal vapour [4, p 272]. At pressures higher than 0.1–0.5 Atm [4, p 247] increased collision frequency and density are achieved intensifying the exchange of energy, and, even more important, the diffusion losses of electrons slow down, increasing the degree of ionization to the equilibrium level corresponding to the electron temperature [4, p 287].

The typical intensity of the light emitted by the plasma versus the time is shown in Figure 3-1 (d). Although the current is fixed, the study of the light reveals strong perturbations of the gaseous phase at the atomic level which are often mirrored on the voltage signal. In the bulk plasma, the copious excited species that participate to the NP synthesis vary significantly with time and affect the NP properties. It could be considered that the dynamic light intensity (or spectrum, see below) is not related to the variation of ionization and excitation reactions in the plasma, but is simply provoked by the discharge displacement during the arc run. After all, light intensity is recorded using a camera (see below) outside the water vessel and depending on the position of the arc with respect to the electrodes the latter might shadow the light signal. But still, such a displacement is just another evidence of spatiotemporal variation of the parameters of the plasma within the specific volume probed by the PMT (or spectrometer). These parameters, in turn, determine the discharge propagation and luminous intensity.

### 3.2.2. HIGH SPEED IMAGING

Figure 3-3, depicts successive frames captured during a discharge of ~ 0.7 s while the current was stabilized at 35 A. It appears that there is intense ionization-excitation between areas of the electrodes which are not in contact and continuous release of vapour bubbles formed in the plasma core.

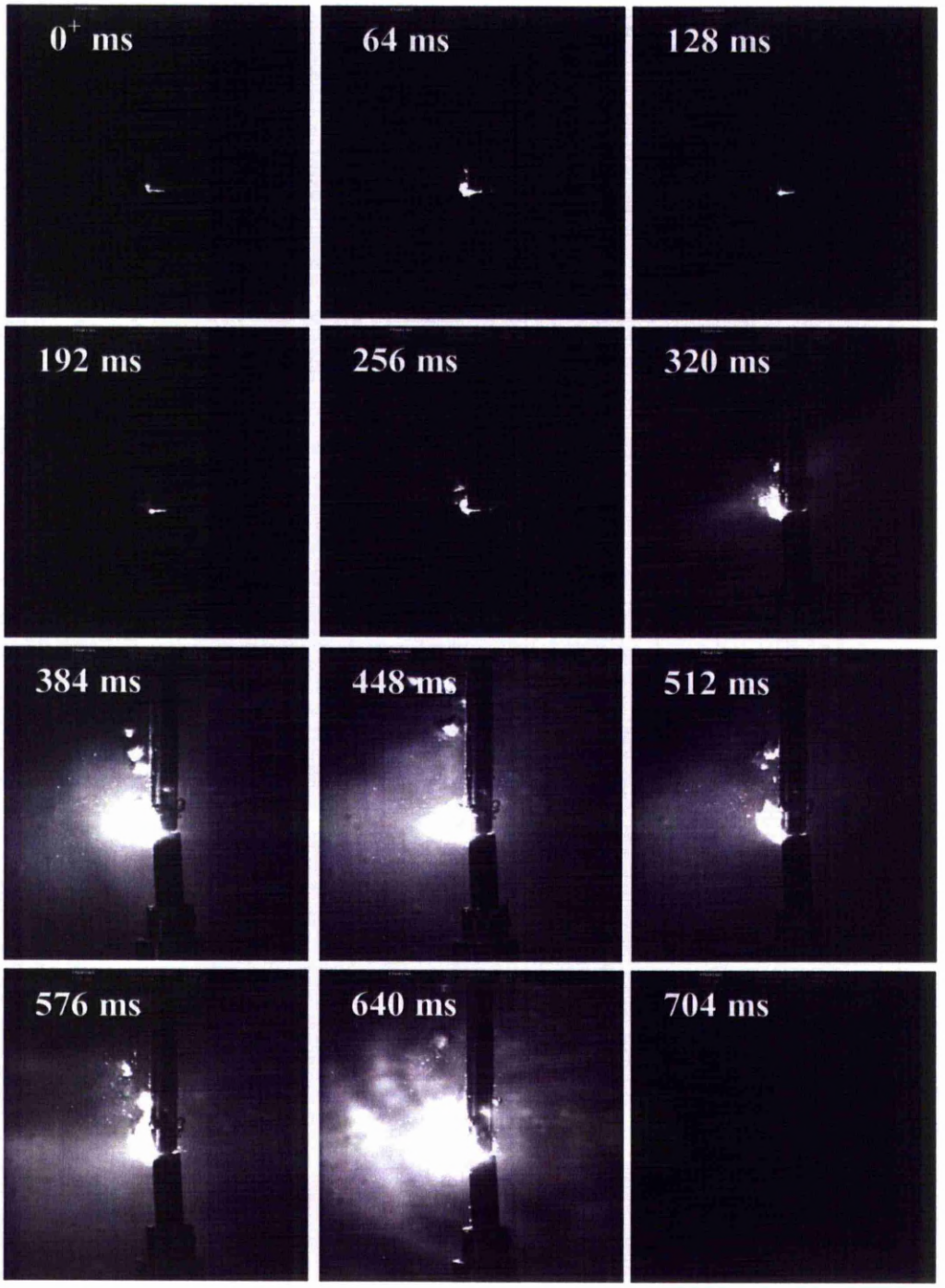


*Figure 3-3: Time-resolved snapshots between the ignition and exhausting of a single dc arc in de-ionized water. The electrode diameter is 6.35 mm.*

Despite the stochastic aspect of the appearance of an electrical breakdown [6, 7], Figure 3-3 shows a representative example of the geometry and location of the

arcs examined in this work; the plasma occupies a volume enclosing the electrode gap, even though it expands, contracts and rotates.

The high-speed camera was set at 125 frames per second (fps), or else, every 8ms and was triggered using a home-made circuit to capture the first image at the instance the open voltage dropped below 60 V (zero second). The snapshots shown above are every 64 ms in order to illustrate the evolution of the discharge. Initially, there is a very low intensity spark, since not all the arcs occurring simultaneously have yet evolved. After 64 ms the intensity starts to rise however, it decreases again ($3^{rd}$ snapshot) due to deformation of the electrodes. The current finds significant amount of conducting paths at 320 ms and localized high pressure causes gas bubbles to form and escape towards the surface of the water. The centre of the arc constantly changes since the electrode damage is very rapid and new arcs are bursting at neighbouring points of the electrode surface. Various plasma fluctuations occur until the electrodes have been deformed/consumed enough for the current to pass through so the arc stops (typical electrode gap ~2 mm).

### 3.2.3. Optical Emission Spectroscopy

By performing OES, excited species, reactive during the arc-discharge were identified. Figure 3-4 presents the intensity of two representative *Al* lines, 394.4 and 396.15 nm, obtained by OES at random instances of the same arc. These lines originate from the 3.14-0.000 and 3.14-0.014 energy levels of the transition $3s^2(^1S)$ $4s$-$3s^2(^1S)$ $3p$, respectively [8]. The variation in the intensity of the *Al* lines supports the above statement about plasma dynamic evolution during the arc and suggests that OES lines could be used as reference signals for the monitoring and control of the production process.

In addition, Figure 3-5 includes all the emission lines and band heads that were recorded by the spectroscopy system. Despite the fact that these spectra were not acquired from the same arc, due to the single-shot character of each arc and the availability of one optical dispersive device, the same excitations were reproducibly recorded and albeit of varied intensity between different arc runs. The wavelengths of all the reactive emission lines are indicated in Figure 3-5. The spectra prove that anode thermal evaporation takes place and aluminium atoms pass to the gaseous

phase. The labelled peaks are in good agreement with the bibliography (Al: [9-12], C: [13, 14], H: [15-17], Fulcher band: [18-20], O: [21, 22], wide spectra [14, 18, 23]).

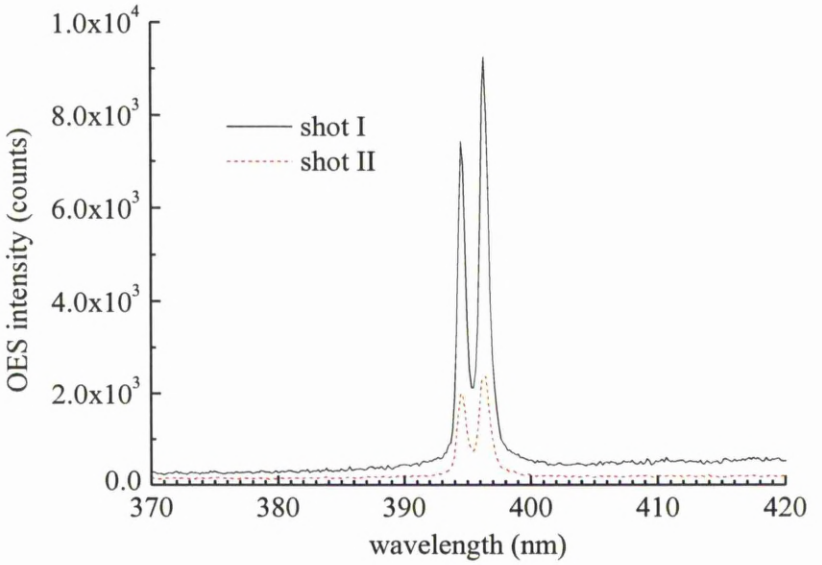


*Figure 3-4: Al lines (394 nm and 396 nm) observed at two difference instances of the same arc-discharge.*

Atomic (Al I) and single charged (Al II) aluminium lines prove that anode thermal evaporation takes place and aluminium atoms pass to the gaseous phase. According to the spectra, the water splits into oxygen and hydrogen. In the UV region around 309 nm, the typical band head structure of OH emission [18, 24, 25] was not observable and only aluminium lines were distinguishable. This strongly suggests that water is directly dissociated into hydrogen and oxygen by high energy electron impacts. The electrolysis releases gases that escape to the water surface as bubbles.

The high-speed imaging in Figure 3-3 clearly presents this effect. Evaporated Al and released O are the precursors of the NP 'seed'. The origin of carbon detected in the optical emission spectra could be water contamination, cathode spots [26, p 259], cathode sputtering by high energy ions, etc.

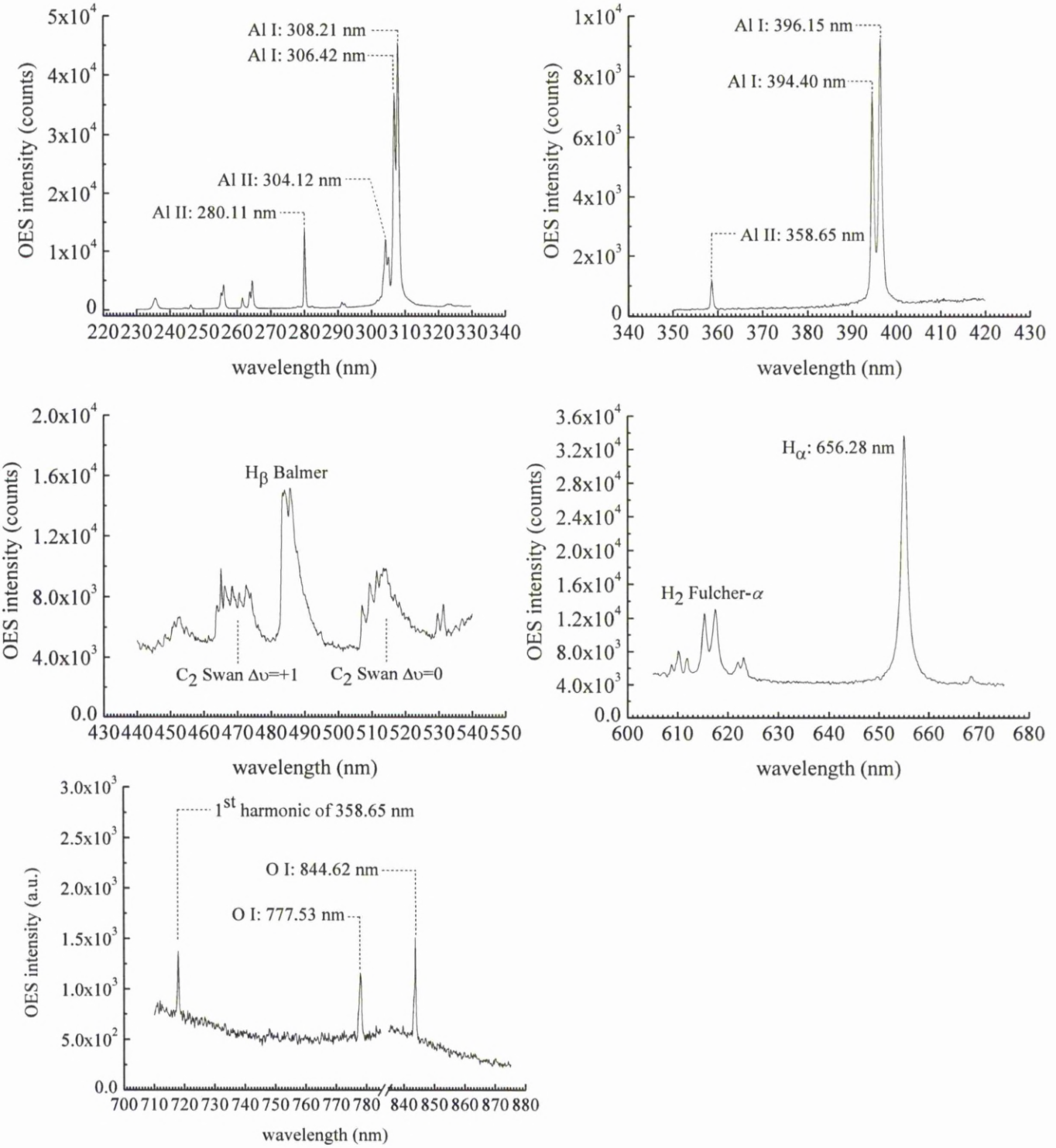


*Figure 3-5: Optical emission spectra of Aluminium arc-discharge from 200 nm to 900 nm.*

The complex gaseous medium containing high energy electrons, positive ions like $H^+$, excited Al*, O*, H*, C*, *etc.* is produced. The most significant finding of OES is the proof of the split of water molecules, to oxygen and hydrogen, giving the opportunity to aluminium atoms to became oxidized and form alumina.

### 3.2.4. ELECTRODE MASS REDUCTION

The anode evaporation is also confirmed by measuring the variation of both electrode masses (Figure 3-6). The error bars were calculated using a standard deviation after adding several arc times. It is more felicitous to refer to these data as 'mass reduction rate' than 'evaporation rate' due to the foreign by-products derived on the electrodes from the arc, e.g. alumina. The term 'evaporation rate' should be referred only to the unique element of every electrode, i.e. Al for the anode and C for the cathode.

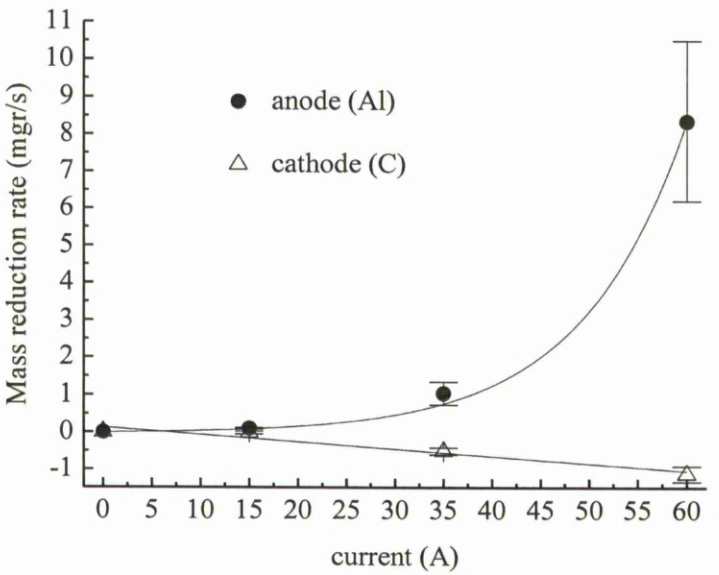


*Figure 3-6: Mass reduction rate of both electrodes used for arc-discharge in water*

The anode mass reduction rate increases exponentially with the increasing arc current (see as well the mass removal in photo of Figure 3-7), while the cathode mass increases slightly (negative reduction rate). The area around the tip of the anode is covered with melted Al, which is most probably oxidized to form alumina. The

carbon electrode is macroscopically unaffected (see photo in Figure 3-7) except for Al deposits on its surface due to welding. It is the latter that add to the mass of the cathode. It could therefore be deduced that an anodic arc-discharge is present [27]. The degradation of both electrodes chiefly affects the duration of the arc and the NP production rate. Though statistical measurements are not available, tentative observations indicate that the moderate current of 35A yields a long life-time for the arc runs (indicatively up to 10 s) and a comparatively small dispersion of the NP size distribution (as observed with Electron Microscopy). Lower current density (e.g. 15 A) gives arcs of similar life-time, but the size distribution seems broader. Finally, at higher current (e.g. 60 A) the arcs are unstable and shorter, and fragments in millimetre-scale are commonly detached from the anode (see as well the error bar width in Figure 3-6).

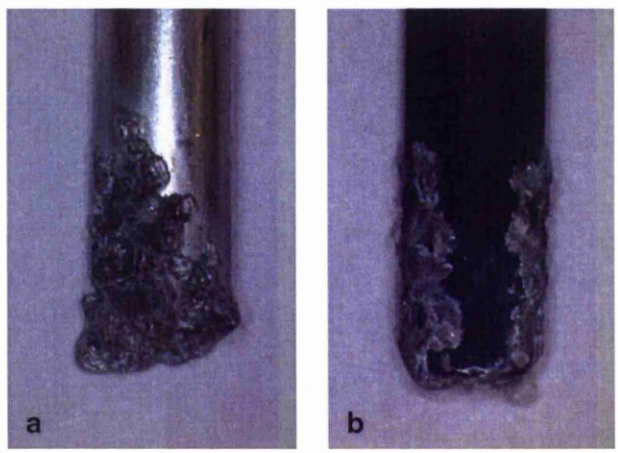


*Figure 3-7: Degradation of the electrode parts subjected to arc-discharge. Aluminium electrode (left) and Carbon electrode (right).*

## 3.3. NANOPARTICLE CHARACTERIZATION

### 3.3.1. HIGH RESOLUTION TRANMISSION ELECTRON MICROSCOPY

During the arc discharge particles float mainly from the arc level and onwards till they reach the surface of the water beaker. After the end of the NP production process, the content of the beaker is almost half decanted to another glass container

and is placed on a hot plate. The reason of the vessel alteration is to avoid the large fragments that detach from the electrodes during plasma and rest in the bottom of the beaker. The temperature of the hot plate is set below 100 °C and after the evaporation of water, the product is collected in powder form. Samples for structural examination are collected on holey carbon TEM grids, either from the beaker after a set of arc runs or, by diluting the dry powder in de-ionized water which in turn, was cleaned ultra-sonically for 5 minutes.

The morphology and microstructure of the discharge product was studied using a FEI Tecnai G2 Spirit BioTWIN, operating at 120kV, for inventory low magnification microscopy (max magnification 300kx times) and a 4000EX II Jeol Ltd. transmission electron microscope operated at 400 kV with a resolution limit of 0.14 nm. Low resolution microscopy showed the presence of crystalline spherical nanoparticles in various diameters; however the vast majority (>95%) were in nanometer scale. Typical TEM micrographs of the as-synthesized NPs are shown in Figure 3-8 (a), (b). The agglomeration consists of well-defined spherical particles and the diameters were statistically ranged between 5 and 100 nm, with a mean particle size of ~ 40 nm.

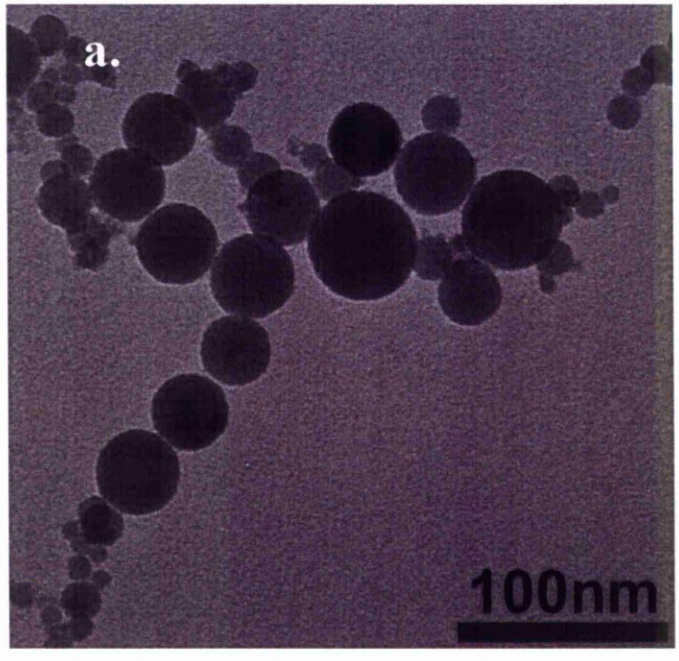

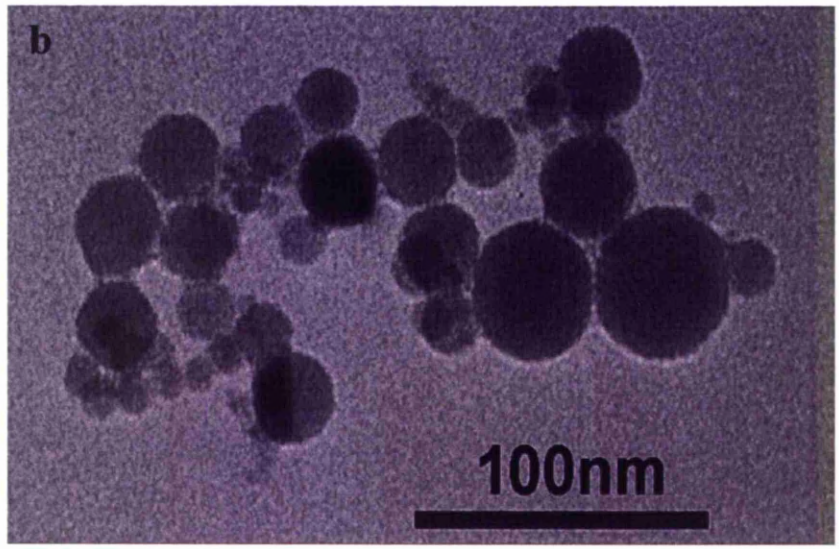


Figure 3-8 (a), (b): TEM micrographs of Aluminium arc cluster particles.

The size distribution of the product was further studied with a highly sensitive dynamic light scattering system (Malvern HPPS). A small volume (<3 ml) of the solution was analyzed after its agitation under ultrasonic conditions for 10 min. A few tens of tests were repeated providing graphs as the one in Figure 3-9.

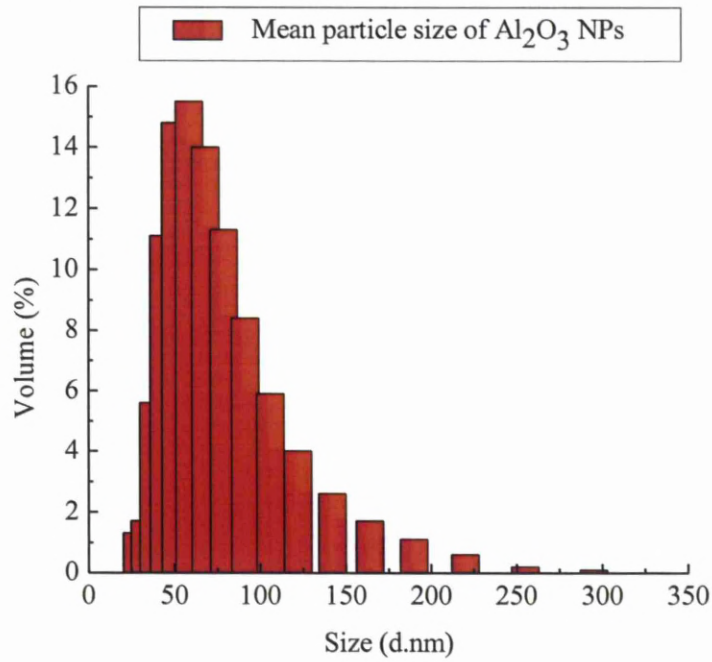


*Figure 3-9: Size distribution of the powder grains collected.*

The mean particle size was measured to be 72.5 nm. However, this result is in discrepancy with the TEM findings, which show a significantly lower NP distribution. In this case, the distribution is shifted to the right, suggesting higher particle sizes and, therefore, a higher mean value. Although the detection of NPs smaller than 25 nm is within the capabilities of the apparatus used, no signal is received in this region (Figure 3-9). This fact could be attributed to inherent particle agglomeration which distorts the distribution derived by the particle analyzer. Therefore, TEM observations are more trustworthy.

High resolution microscopy revealed the crystalline nature of the particles. TEM micrographs clearly show crystalline nanoparticles.

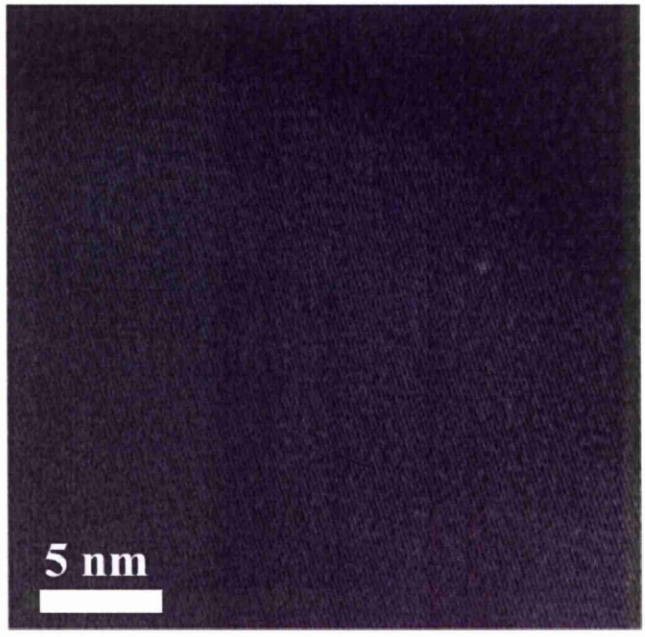


*Figure 3-10: High Resolution TEM micrograph of a single nanoparticle.*

The lattice spacings and the angles between the illustrated lattice fringes were measured. A fast Fourier transform was applied on the images obtained and the digital diffraction pattern was derived. The experimental data were compared to Chemical Database Service [28].

Figure 3-11 (a) shows an atomic resolution image of a single crystal particle. Figure 3-11 (b) shows a 512x512 pixel area of the particle. Using Fast Fourier Transform (FFT) we have produced the Digital Diffraction Pattern (DDP) shown in Figure 3-11 (c). Using the DDP we have calculated $d_1$=0.289 nm, $d_2$ = 0.247 nm and

$d_3 = 0.247$ nm and the angles between them $\varphi_{12} = 65.1^\circ$, $\varphi_{13} = 115.3^\circ$ and $\varphi_{23} = 50.2^\circ$. The values of the d-spacings (error ranges ~ 0.05 nm) and angles (error ranges ~ $1.5^\circ$) derived from the DDP closely match those for the (02-2), (31-1), and (3-11) planes of $\gamma$-$Al_2O_3$. In fact, the DDP of the marked area Figure 3-11 (a) corresponds to that of theoretical $\gamma$-$Al_2O_3$ crystal along the [011] zone axis (Figure 3-11(d)).

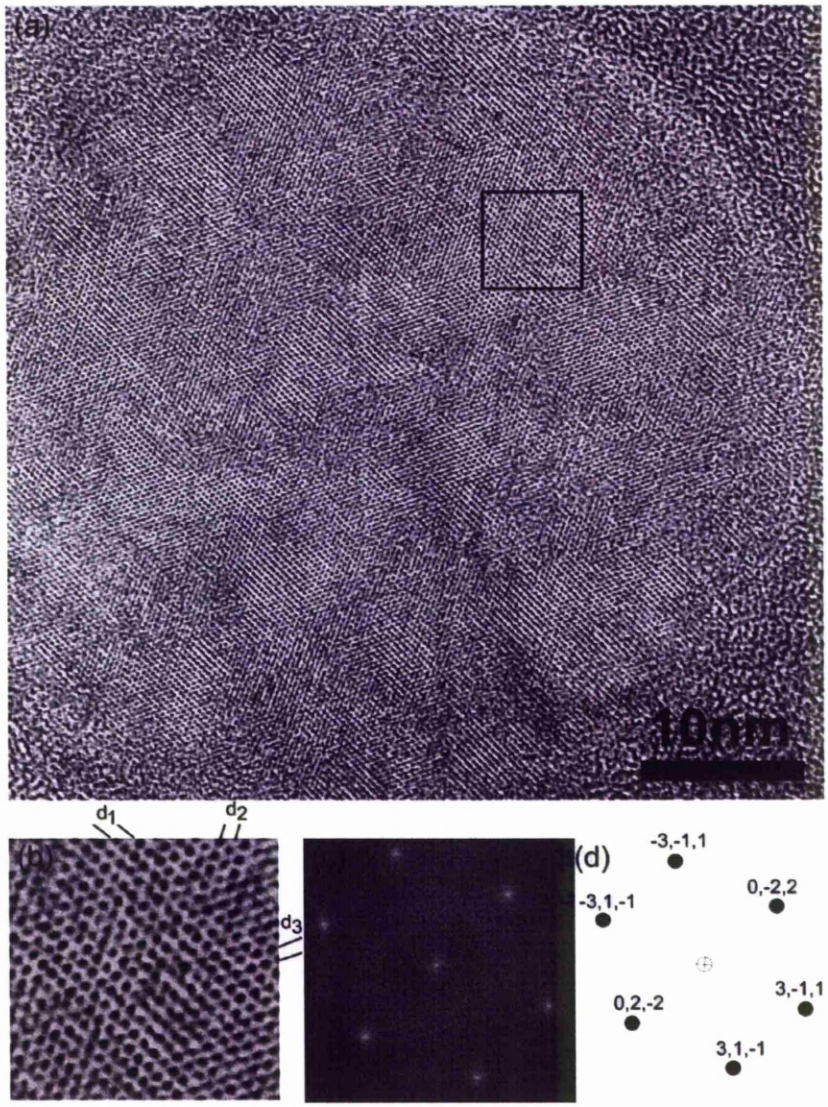


*Figure 3-11: (a) HRTEM micrograph of an as-synthesized particle (particle size 45nm). The FFT of the region indicated in the square (b) generates the DDP shown in (c). The DDP of the 512x512 pixels area was used to identify image as the [011] zone axis of theoretical $\gamma$-$Al_2O_3$ shown in (d).*

### 3.3.2. X-RAY DIFFRACTION (XRD)

The XRD analyses (Figure 3-12) further testified that the NPs were pure alumina in the $\gamma$-phase [28]. It is remarkable that no carbon from the cathode or other impurities were introduced to the chemical structure of the particles, although the optical emission spectra showed their fingerprints. Based on the broadening of the most prominent peak ([4 0 0], $2\theta = 46.11^{\circ}$) in the XRD profile, a mean crystallite dimension $\tau \approx 7.4$ Å was calculated by Scherrer's formula [29, 30]:

$$\tau = K\lambda / \beta \cos\theta \qquad (1)$$

where $\lambda$ stands for the X-ray radiation wavelength (here ~1.50 Å), $\beta$ for the line broadening at half the maximum intensity in radians (herein 0.02), $\theta$ is the Bragg angle and $K$ is a shape factor. For the case of a sphere has been shown that $K = 0.9$. To the best of the author's knowledge, this is the first time that high purity $\gamma$-phase $Al_2O_3$ crystalline NPs have been produced by the arc-discharge in water method.

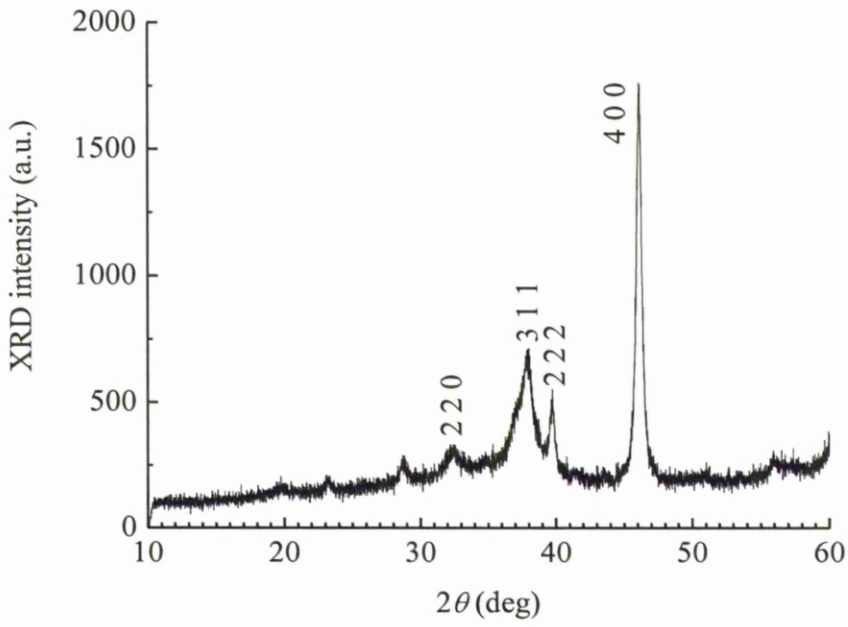


*Figure 3-12: XRD pattern of the produced $Al_2O_3$ nanopowder*

### 3.3.3. X-RAY PHOTOELECTRON SPECTROSCOPY (XPS)

The photoemission experiments were carried out in an ultra high vacuum system (UHV) which consists of a fast entry specimen assembly, a sample preparation and an analysis chamber [31]. The base pressure in both chambers was $1\times10^{-9}$ mbar. Unmonochromatized MgKα line at 1253.6 eV and an analyzer pass energy of 97 eV, giving a full width at half maximum (FWHM) of 1.7 eV for the Au $4f_{7/2}$ peak, were used in all XPS measurements. The XPS core level spectra were analyzed using a fitting routine, which can decompose each spectrum into individual mixed Gaussian-Lorentzian peaks after a Shirley background subtraction. Regarding the measurement errors, for the XPS core level peaks it was estimated that for a good signal to noise ratio, errors in peak positions are of about ±0.05 eV after calibrating the instrument according the equipments specification. The binding energy (BE) scale was calibrated by assigning the main C1s peak at 284.6 eV.

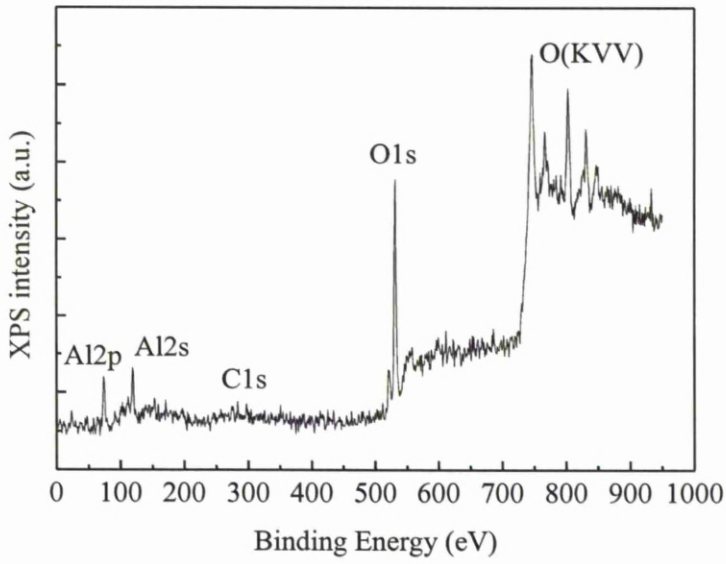


*Figure 3-13: XPS wide scan $AlO_x$ sample.*

The spectrum (Figure 3-13) clearly reveals the photoelectron peaks of *Al2p*, *Al2s*, *O1s*, as well as the X-ray-induced Auger peak O(KVV) indicating the formation of $AlO_x$ thin films. Moreover, the scan indicates the position of the carbon peak (*C1s*) where it is easily seen that there is no significant presence; proving that, not only that

there is no bonding with carbon during the formation of the NPs, but also that there are no impurities in the powder. The C1s peak is comparable to the background noise, that is, very weak. The C1s peak is analyzed into two components in Figure 3-14 (c). The first at BE = 284.6 eV is attributed to residual carbon usually in the graphitic form and the second, at 286.3 eV, corresponds to carbon atoms attached to oxygen or hydroxyl species. Focusing on the two aluminium peaks (*74.7 eV* and *119.6 eV*) and the oxygen peak (*532 eV*) from the literature it is known that these values correspond to $Al_2O_3$ [32] (Figure 3-14).

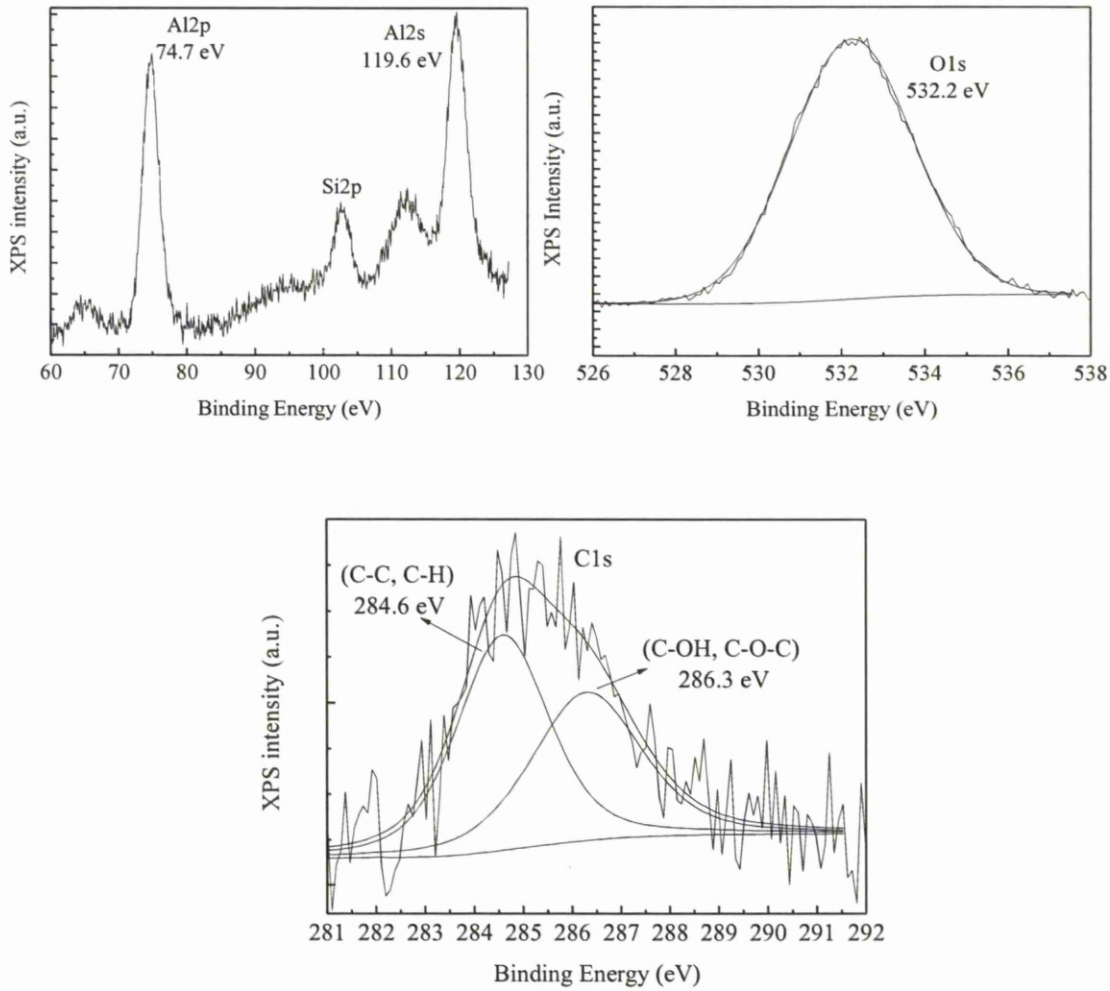


*Figure 3-14: Zooming to the predominant lines (Al, O, C)*

## 3.4. PRODUCTION MECHANISM

Spheroidization of micro-sized solid particles is clearly a melting operation [33]. The nano-sized particles reported here are however, produced by another mechanism. It is suggested that the solidification of most of the particles is initiated by homogeneous nucleation and occurs at a temperature considerably below the equilibrium melting point [33]. Quenching following chemical reactions is often vital for making the desired product. Chemical species which are formed as stable products at high temperatures may undergo undesirable phase changes during gradual cooling to room temperature. The desired product, however, may be preserved by rapid quenching to room temperature [34]. In the present process, the arc 'burst' to the colder water ensures the product quenching and stabilization to its final form, as explained in detail in the next paragraph.

The above experimentally monitored anode thermal evaporation and hydrolysis feed the discharge vapours with Al and O atoms. The images of Figure 3-3 imply that electrohydrodynamic effects are present, causing expansion of the plasma and vapour displacement from the high temperature arc to cold water. The formation of pressure waves in arc discharges has previously been reported [35, 36] however, in this case, it is the gas flow generated by pressure difference that carries the species away from the arc column and is the driving force for the initiation of primary nucleation and crystal shaping of the NPs. That is to say, the rapid quenching of the plasma-produced species in the vapour state leads to a high supersaturation which, in turn, gives rise to homogeneous nucleation [37]. Since the nucleation rate increases extremely fast with decreasing temperature, the particles produced will all solidify within a small temperature range [33]. During the nucleation, the degree of supersaturation is reduced due to NP formation and there is a moment at which the vapours are no more supersaturated and the nucleation stops. The time elapsed between the primary nucleation and this moment determines the NP size.

The crystallization process is governed by both thermodynamic and kinetic factors, which can make it highly variable and difficult to control. Factors such as impurity level, mixing regime, vessel design and cooling profile can have a major impact on the size, number and shape of crystals produced [38]. Despite the complexity arising from the interaction of the electrical arc and the supersaturation process, it is here postulated that it is vital to build an arc-discharge in water system

for production of high purity crystalline NPs of alumina at the metastable phase gamma. This robust system is lastly promising for full production capacity.

## 3.5. SUMMARY

High purity gamma-alumina NPs were produced with an arc-discharge in water. The discharge was running between Al anode and C cathode, and exhibited characteristics similar to an anodic thermal arc. It was found to be rich in excited Al I,O I, $C_2$ and H, with densities significantly varied in an arc event. For an arc current of 35A the typical arc duration was 5–10 s, and spherical crystalline particles having mean diameter 40 nm were obtained. The production mechanism involved the anode atomization and water hydrolysis, followed by the formation of supersaturated vapours. The relative concentration of the substances of these vapours was indirectly monitored by real-time OES which could in the future provide feedback signals for a more controllable synthesis process.

## 3.6. REFERENCES


[1] I. Wenåker, *Physica Scripta,* 42, 667 (1990).

[2] H. Bhuyan, M. Favre, E. Valderrama, G. Avaria, E. Wyndham, H. Chuaqui, J. Baier, H. Kelly, D. Grondona, A. Marquez, *Appl. Surf. Sci.,* 255, 3558 (2009).

[3] E. Nasser, *Fundamentals of Gaseous Ionization and Plasma Electronics* (1971) Wiley

[4] J. Heberlein, *Pure Appl. Chem.* 74 327-335 (2002).

[5] K.B.S. Eriksson, H.B.S. Isberg, *Arkiv foer Physik,* 23, 527 (1963).

[6] S. Dadras, M.J. Torkamany, J. Sabbaghzadeh, *J. Phys. D: Appl. Phys,* 41 225202 (2008).

[7] V. Kaufman, L. Hagan, *Journal of Optical Society of America* 69 232 (1979).

[8] A.L. Patterson, *Phys. Rev.* 56, 978 (1939).

[9] K. B. S. Eriksson and H. B. S. Isberg, *Ark. Phys.* 23 527 (1963)

[10] S. Dadras, M. J. Torkamany and J. Sabbaghzadeh, *J. Phys.D: Appl. Phys.* 41 225202 (2008).

[11] V. Kaufman and L. Hagan *J. Opt. Soc. Am.* 69 232–9 (1979).

[12] F. Paschen and R. Ritschl *Ann. Phys. Lpz.* 410 867–892 (1933)

[13] S. S. Harilal, R. C. Issac, C.V. Bindhu, V. P. N. Nampoori and C. P. G. Vallabhan *J. Phys. D: Appl. Phys.* 30 1703 (1997).

[14] R. Khalid, K. Yaqub, S. Yaseen, S. Javeed, A. Ashraf, S. A. Janjua and S. Ahmad *Nucl. Instrum, Methods Phys. Res. B,* 263, 497 (2007).

[15] C. G. Parigger, M. Dackman and J. O. Hornkohl , *Appl. Opt.*47 G1–6 (2008).

[16] C. G. Parigger, D. H. Plemmons and E. Oks *Appl. Opt.* 42 5992–6000 (2003).

[17] R. ˇ Ziki´c, M. A. Gigosos, M. Ivkovi´c, M. ´A. Gonz´alez and N. Konjevi´c, *Spectrochim. Acta Part* B, 57, 987 (2002).

[18] D. Vujoˇsevi´c, M. Mozetiˇc, U. Cvelbar, N. Krstulovi´c and S. Miloˇsevi´c *J. Appl. Phys.* 101, 103305 (2007).

[19] V. Suendo and P. Roca i Cabarrocas, *J. Non-Cryst. Solids* 352, 959 (2006).

[20] B. Xiao, S. Kado, S. Kajita and D. Yamasaki *Plasma Phys. Control. Fusion,* 46, 653 (2004).

[21] C. E. Moore *National Standard Reference Data System* 3 section 7, 30, (1976).

[22] I. Wenåker, *Phys. Scr,.* 42, 667 (1990).

[23] Bhuyan H, Favre M, Valderrama E, Avaria G, Wyndham E, Chuaqui H, Baier J, Kelly H, Grondona D and Marquez A *Appl. Surf. Sci.,* 255, 3558 (2009).

[24] S. B. S. Heil, J. L. van Hemmen, M. C. M. van de Sanden and W. M. M. Kessels *J. Appl. Phys.,* 103, 103302 (2008).

[25] K. J. Trevino and E. R. Fisher, *Plasma Process. Polym.,* 6, 180 (2009).

[26] P. Yu. Raizer, *Gas Discharge Physics* Springer-Verlag (1997).

[27] N. B. Jemaa and L. Morin *IEEE Trans. Compon. Packag. Technol.,* 25, 651 (2002)

[28] D. A. Fletcher, R. F. Mc Meeking, and D. J. Parkin, *J. Chem Inf and Com Sci.,* 36, 746 (1996).

[29] A. L. Patterson *Phys. Rev.,* 56, 978 (1939).

[30] M. Birkholz, P. F. Fewster and C. Genzel *Thin Films Analysis by X-ray Scattering* (New York: Wiley) (2006).

[31] A. Siokou, V. Papaefthimiou, S. Kennou, *Surf. Sci, 482, 2, 20, 1186* (2001).

[32] S. Ntais, A. Siokou, *Surf. Sci.*, 600, 18, 4216 (2006).

[33] R. McPherson, *J. Mater. Sci.* 8 851 (1973).

[34] R. M. Young and E. Pfender *Plasma Chem. Plasma Process.,* 5, 1 (1985).

[35] P. Bruggeman and C. Leys, *J. Phys. D: Appl. Phys.,* 42, 053001 (2009).

[36] J. S. Chang, P. C. Looy, K. Urashima and A. D. Bryden *Conf. Electr. Insul. Dielectr. Phenom.* 105 (2000).

[37] C. G. Granqvist and R. A. Buhrman *J. Appl. Phys.* 47 2200 (1976).

[38] http://wapedia.mobi/en/Crystallize

# 4. TANTALUM OXIDE NP PRODUCTION

## 4.1. TANTALUM OXIDE GENERAL BACKGROUND

Tantalum pentoxide ($Ta_2O_5$) is a refractory dielectric material extensively used for electronic devices and other applications. Electrolytic capacitors have made use of the chemical and thermal stability of amorphous $Ta_2O_5$ having a dielectric constant value between 25 and 27, while ceramics based on crystalline $Ta_2O_5$ have exhibited dielectric constant values of up to 280 at room temperature [1] providing obvious merits for construction of miniaturized devices, such as high density dynamic random access memories [2-4].

Additional unique properties of $Ta_2O_5$ such as its high refractive index (about 2.2), very low light absorption coefficient, and wide optical bandgap (4.35 eV) offer the possibility for further applications such as photonic crystal waveguides or other active optical devices [5] and antireflection coatings on solar cells [6]. Piezoelectric thin films [7] and improved pitting corrosion resistance of metal substrates [8] are two last but not least applications.

However, due to their peculiar structural characteristics and size effects, nanomaterials demonstrate some physicochemical properties, which are different from those of the bulk materials and are of great interest both for the theoretical study and for the potential nanodevice applications [9-11]. One approach is to add functional NPs into polymers and thus tailor at the nanometer scale key physical properties of the resulting composite material. Indeed, $Ta_2O_5$ NPs are promising candidates for nonlinear optical materials with good thermal stability, [12] promote photocatalytic reactions under de-aerated and aerated conditions [13], increase the performance of high temperature metal-insulator-silicon carbide gas sensors, [14] provide ceramic/polymer nanocomposites for polymer waveguides [15], just to name a few applications, and they have generally evoked great interest for the modification of bulk material characteristics. This potential provides strong motivation towards systematic research activity on the production of $Ta_2O_5$ NPs.

This chapter describes the production of $Ta_2O_5$ crystalline NPs by the arc-discharge in water, as part of an effort to use the reactive environment within the

thermal plasma to form oxide nanoparticles [16]. Although tantalum pentoxide NPs have been formed by diverse techniques (chemical [13, 17] plasma [9, 15], ion implantation [12] etc.), this appears to be the first attempt by arc discharge in water.

The NPs are identified by high resolution transmission electron microscopy (HRTEM), X-ray diffraction (XRD), X-ray photoelectron spectroscopy (XPS), and size distribution measurements. Although this is the main claim of this work, of equal importance is the understanding of the growth mechanism because it would allow better control of the process and scale up. Therefore, the arc-discharge is studied in situ by electrical measurements, integral optical emission records, optical emission spectroscopy (OES), and high speed imaging. This combined study of the product and production medium unveils the mechanism governing the $Ta_2O_5$ NPs synthesis.

## 4.2. DISCHARGE CHARACTERISTICS

### 4.2.1. ELECTRICAL CHARACTERISTICS

The only alteration on the experimental set up used for this experiment was that instead of using an aluminium rod, a tantalum rod was the anode. Taking into account the fact that aluminium oxide NPs can be produced by this method, the goal was to justify this method as a cost-efficient and easy to implement method for metal oxide NPs. For this reason, a 5 mm tantalum rod was used as the anode and a 6.35 mm graphite rod as the cathode.

Once more, three current densities (15A, 35A and 60A) were tested to identify the most efficient conditions for the NP production. The melting point (3017 °C) of tantalum is significantly higher than that of aluminium (660.32 °C) so the possibility of using higher current to increase the plasma energy had to be tested. In terms of arc stability, 35 A was shown to offer the most advantage. When a 15 A arc current was used, the arc was not as intense as at 35 A resulting in the extinction at much shorter electrode separation. In contrast, 60 A arc-current was so intense that large fragments of the anode were found in the bottom of the beaker after several arc-runs. Below, the electrical characteristics as well as the emitted light intensity of the arc-discharge, using a tantalum rod as an anode, are presented (Figure 4-1).

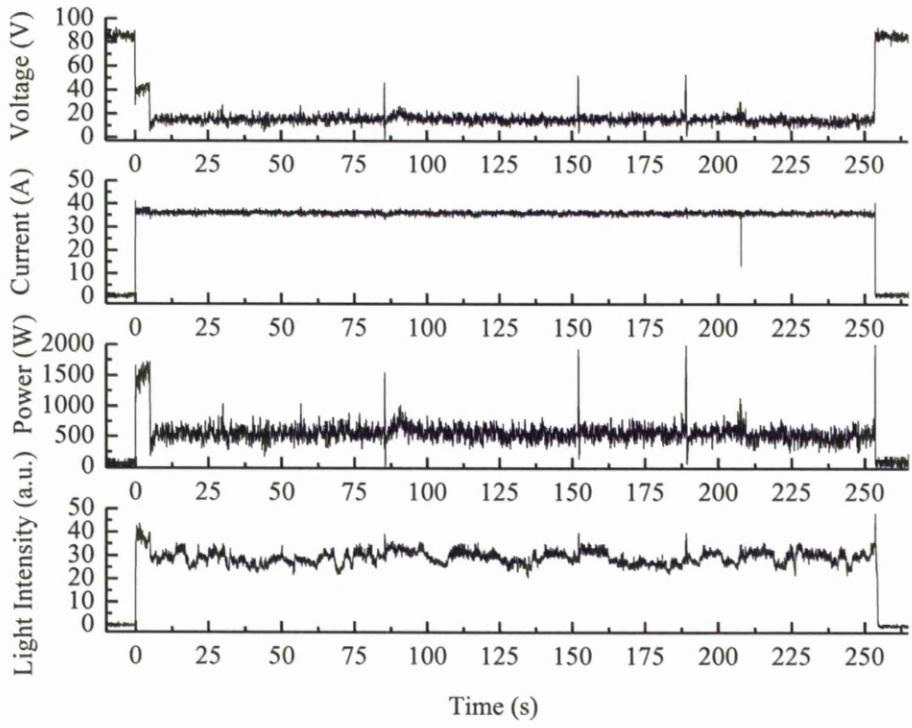


*Figure 4-1: Electrical characteristics and luminous activity of the arc-discharge in water using a Tantalum rod as anode.*

As long as the electrodes are separated, the gap voltage is equal to the open-circuit voltage of the power supply, i.e., 83 V. A circuit is closed either when the electrodes are brought so close that the local electrical field exceeds the liquid dielectric strength or when they are brought into physical contact. In both cases (zero time in Figure 4-1), the current rises and stabilizes at the pre-selected value of 35 A. This current induces hydrolysis and local heating, which, in turn, provoke water vapour release.

When the plasma was established, the inter-electrode conductivity increases and the voltage drops to a value typically lower than 20 V (see Figure 4-2). The measured values of current and voltage (35 A, 20 V) may justify the term "arc-discharge" used for the system; the arc discharge is characterized by large currents ($1–10^5$ A) and, as a rule, arcs burn at a low voltage not exceeding 20–30 V for short arcs and as low as several volts in some cases [18]. The direct product of the current

and voltage waveforms gives an idea not only about the magnitude of the power consumed in the plasma (0.3 – 0.9 kW) but also about the evolution of this power during the NP production. While the current is maintained constant, consistent with the concept of the current source, the voltage and, consequently, the power fluctuate and sharp peaks appear. These variations indirectly reflect the continuous changes of the space charge in the discharge. Furthermore, the similarity in form between the voltage (power) and the emitted light signals in Figure 4-1 unveils the influence of the space charge energy and density on the excited atoms/molecules, and vice versa. Among these particles there are the "building blocks" of the NPs and their distinction is further investigated.

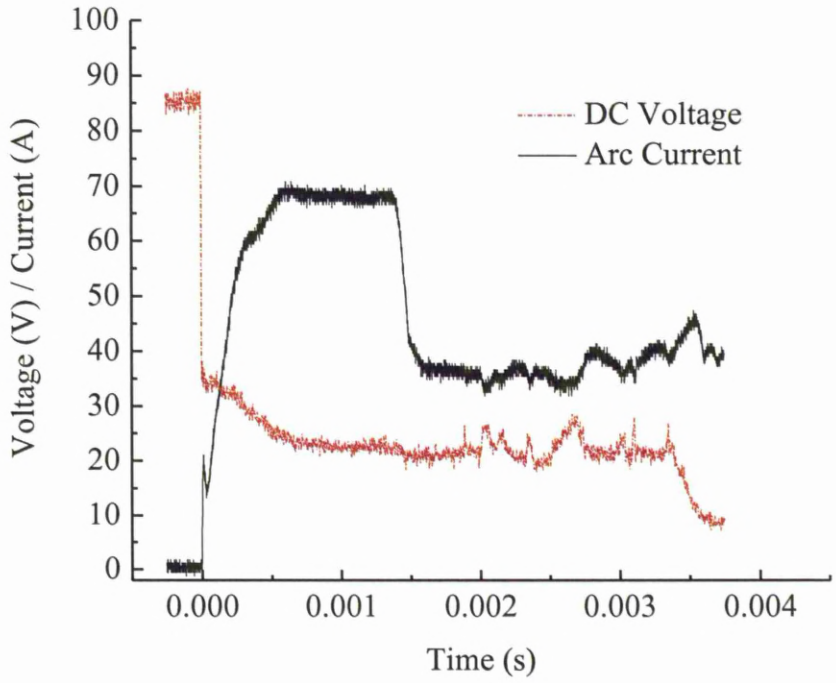


*Figure 4-2: The first 4 ms of the arc-discharge.*

In all signals recorded in Figure 4-1 it is worth noticing that there is stability (compared to aluminium arc) and most importantly the average time of each individual arc lasts minutes (more than 4 minutes) until the arc extinguishes.

### 4.2.2. HIGH SPEED IMAGING

Figure 4-3 depicts a series of time-resolved images of a single arc-discharge. That lasted for 3 s. The same camera settings were applied as with the aluminium arc. Since, the illustrated tantalum arc lasted for 3 s the frames shown below are every 264 ms.

Similarly to previous experiments, the arc intensity is not related with time but with the number of contact/approaching points of the electrodes that are feeding the arc. That is the reason why the light intensity as well as the contact position is constantly changing. Gas bubbles are continuously formed and escape toward the water surface. Hence, water molecules are split feeding the vapour with oxygen and hydrogen (see OES below). The luminous activity in Figure 4-3 and the photomultiplier (PMT) signals in Figure 4-1 demonstrate the establishment of an excited emissive medium in gaseous phase. Clearly, self-sustaining plasma surrounds the electrode tips. The various ionization and excitation reactions are predominantly triggered by energetic electron collisions with the vapour atoms/molecules [19]. As it will shortly be proven, the actual plasma chemistry is much more complicated due to electrode evaporation. However, the above statements of hydrolysis and local heating are confirmed.

The main difference between the aluminium and the tantalum arc relates to how the arc extinguishes. In the case of aluminium, the anode electrode surface was oxidized very rapidly. After this electrode deformation, even if the user was bringing in contact the electrodes to create a new discharge, the oxidized anode would forbid any current to go through. In the case of tantalum, the anode surface was never oxidized and the arc was extinguishing mainly due to electrode gap. The continuous NP production is considered to be a significant advantage of tantalum arc.

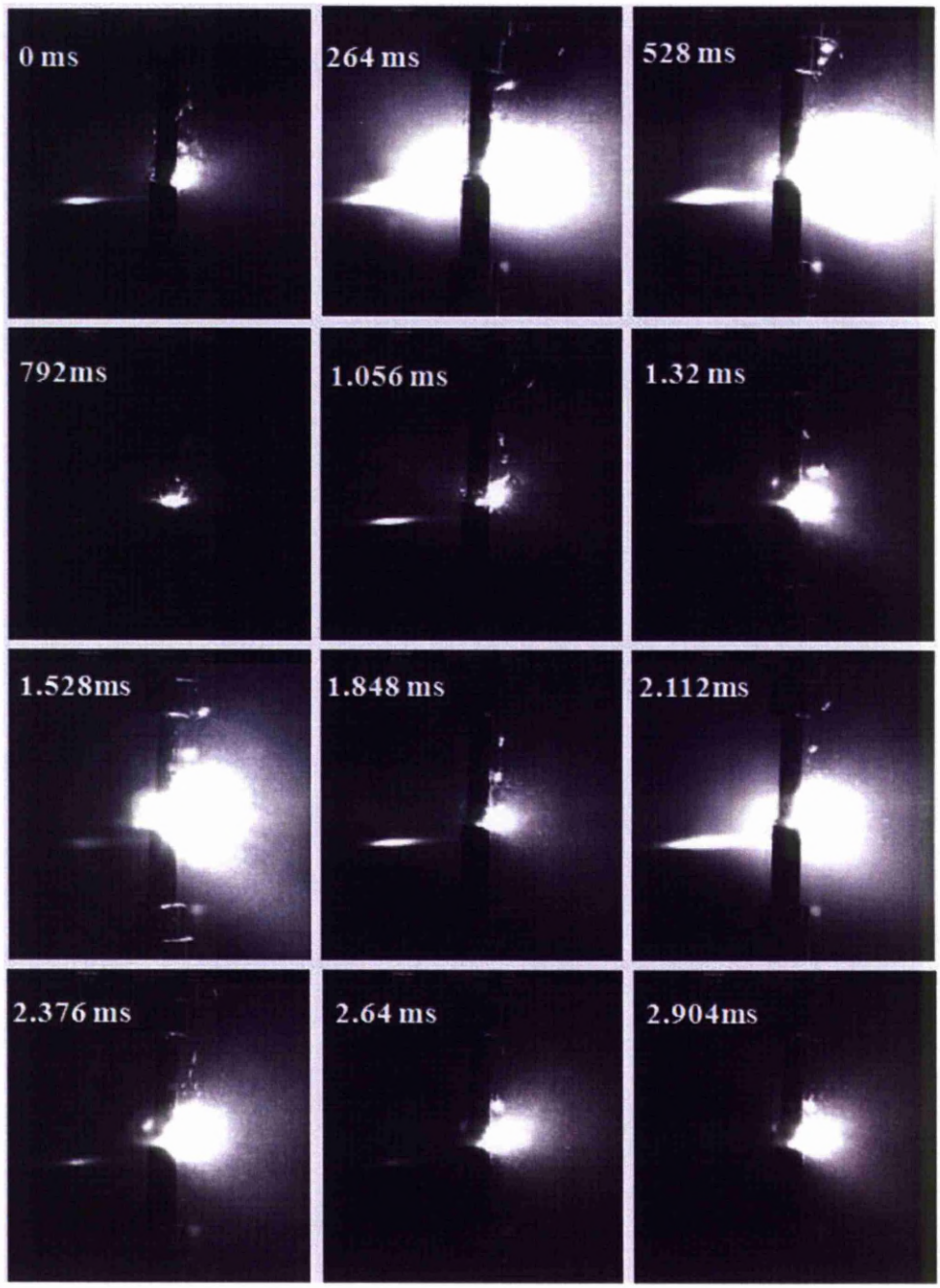


*Figure 4-3: Time-resolved snapshots between the ignition and exhausting of a single dc arc in de-ionized water. The Tantalum electrode diameter is 5 mm.*

### 4.2.3. OPTICAL EMISSION SPECTROSCOPY

Similarly to the previous investigation, OES was applied to the tantalum arc-discharge. However, for the case of tantalum, the optical spectrum is continuous and does not have distinctive peaks [20-21]. Figure 4-4 shows a representative spectrum, from 312 to 353 nm, captured in two different instances of the same arc with two Ta emission lines at 326.02 and 331.79 nm, respectively. The intensity level is clearly changing depending on the number of arcs occurring at each instant. Following the predominant emission lines it is clearly shown that the active species inside the plasma are always the same but not always in the same intensity.

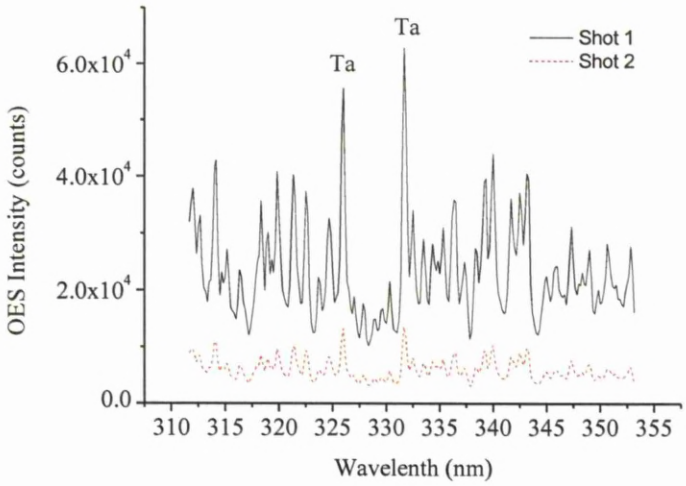


*Figure 4-4: Continuous Tantalum Spectrum with a predominant line at 331 nm.*

The fingerprints of tantalum and carbon as well as the products of $H_2O$ hydrolysis (H, O) are clearly visible in the discharge OES spectrum presented in Figure 4-5. The continuum agrees well with the bibliography [20, 21] and corresponds to tantalum emission. Indisputably, extensive anode thermal evaporation takes place and Ta atoms pass to the gaseous phase where they become ionized or excited. This is also proven by the Ta (326.02 and 331.79 nm) and Ta+ (383.37 nm) lines [22] observed on the continuum. The continuous shape of the spectrum is attributed to hot NPs [20, 23] and can be compared to black-body radiation to deduce the NP temperature [20]. Simultaneously, the emission lines of hydrogen ($H_a$ 656.28 nm, $H_\beta$ Balmer) [24], atomic oxygen (777.53 nm) [25], and single-ionized atomic oxygen

(718.2 nm) [26], originate from water dissociation as it was assumed previously. Furthermore, the intense molecular carbon band heads are emphasized. The bands marked in Figure 4-5 correspond to C2 Swan band [27]. Either cathode is sputtered by energetic ions or unavoidable hydrocarbon contamination is the source of carbon.

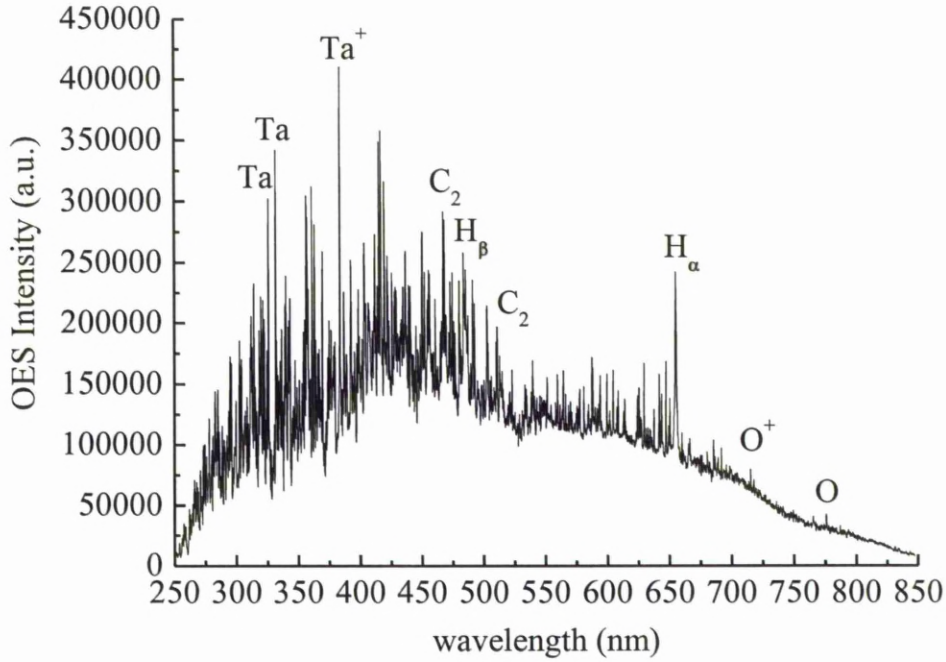


*Figure 4-5: Optical emission (UV-visible) raw spectrum of the Ta–C arc discharge in water*

### 4.2.4. ELECTRODE MASS REDUCTION

Figure 4-6 illustrates the anode (a) and cathode (b) electrodes, respectively, following a few arc-discharge runs. A layer of melted tantalum can be seen on both tips (black shiny color). The curves in Figure 4-7 show the mass reduction rate of both electrodes versus the steady-state arc current. Tantalum is evaporated from the anode, reducing its mass (positive reduction rate), and it is partially deposited on the cathode, increasing its mass (negative mass reduction rate). In this figure, the term "evaporation rate" is avoided because, strictly speaking, this term should be referred to the evaporation of pure Ta or C, but Figure 4-6 show that various components (e.g.,

oxides) are probably deposited on and are removed from the electrodes during the arc, even if the quantity of some of them is small. The formation of insulating layers on the contact surface of the electrodes and, predominantly, the widening of the inter-electrode gap, due to anode evaporation, leads eventually to the extinction of the arc. The long lifetime (e.g., ~ 250 s in Figure 4-1), the stability, and the sufficient confinement of the Ta arcs are distinct characteristics observed for moderate current values (see signals in Figure 4-1).

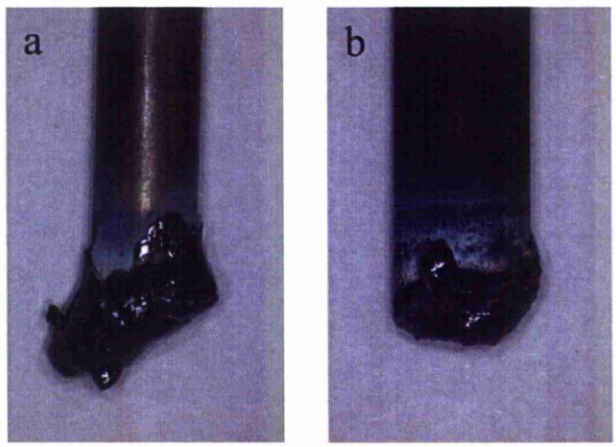


*Figure 4-6: Indicative photos of the anode (a) and cathode (b) electrodes used during many arc runs*

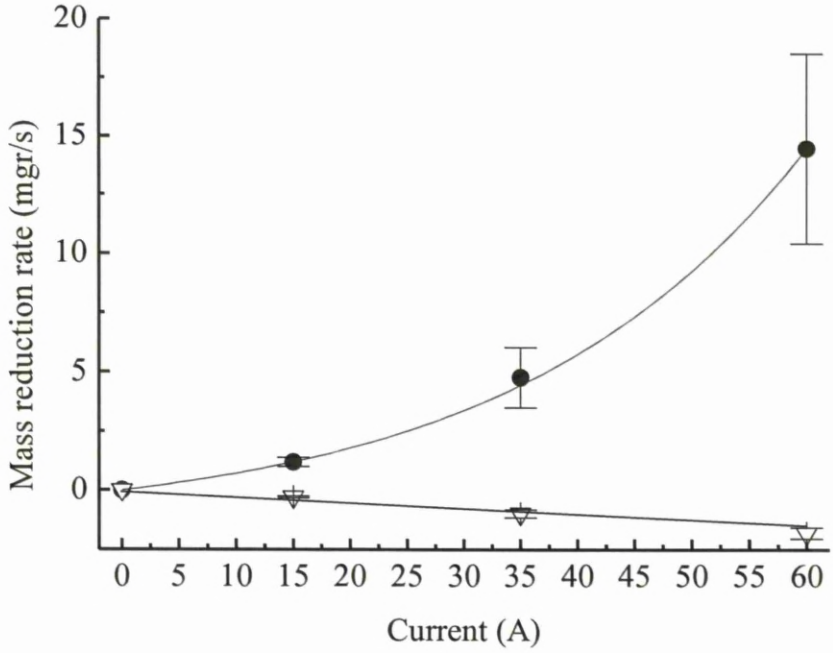


*Figure 4-7: Mass reduction rate of both electrodes as a function of the arc-discharge mean current*

At 60 A current the discharge instabilities lead to variable production rate (typically 4.5%), as the error bars show in Figure 4-7 while at 15 A arc current production rate decreases significantly. The size distribution is also noticeably affected by the arc current. Compared with the product from the 35 A arc, at 60 A the plasma region experiences very intensive alterations, thus detaching large fragments of the anode, whereas at 15 A the low plasma intensity leads to poorly shaped and usually amorphous NPs. The choice of a current of 35 A for the bulk of these studies was based on those empirical remarks of the best control of the discharge and more reproducible product morphology.

## 4.3. NANOPARTICLE CHARACTERISATION

### 4.3.1. TRANSMISSION ELECTRON MICROSCOPY (TEM)

Representative clusters of the NPs yielded by the arc-discharge in water are shown in the TEM images of Figure 4-8 (a) and (b). These spherical NPs have diameters between 5 and 100 nm and mean size of around 40 nm. These distribution parameters were found statistically by examining a large number of low magnification TEM images. Comparing the data derived by TEM observations and the graph in Figure 4-9, which indicates the NP distribution as received by the particle size analyzer, an increase of nearly 20 nm is noted. The particle size analyser suggests that the average diameter is 61 nm; however, no signal has been received for particles below the 15 nm scale. TEM measurement has shown that there is a significant number of particles in that range and they are usually the most agglomerated. This observation possibly, renders the particle analyzer unable to register this group, which in turn increases the average particle size to ~ 60 nm.

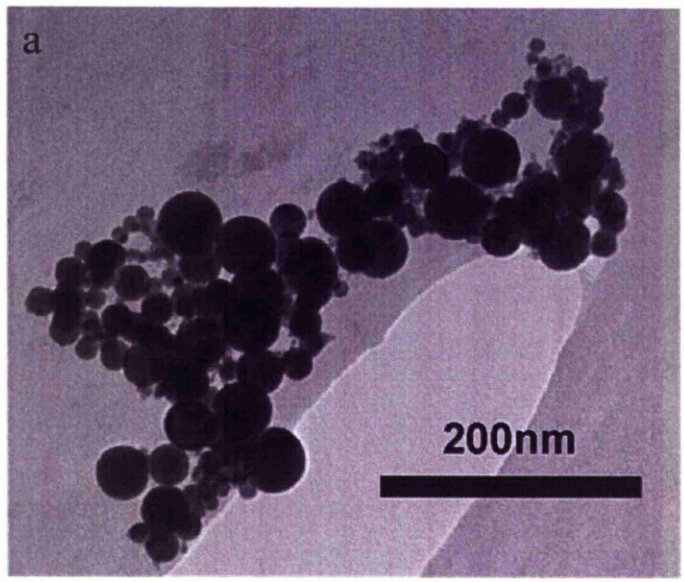

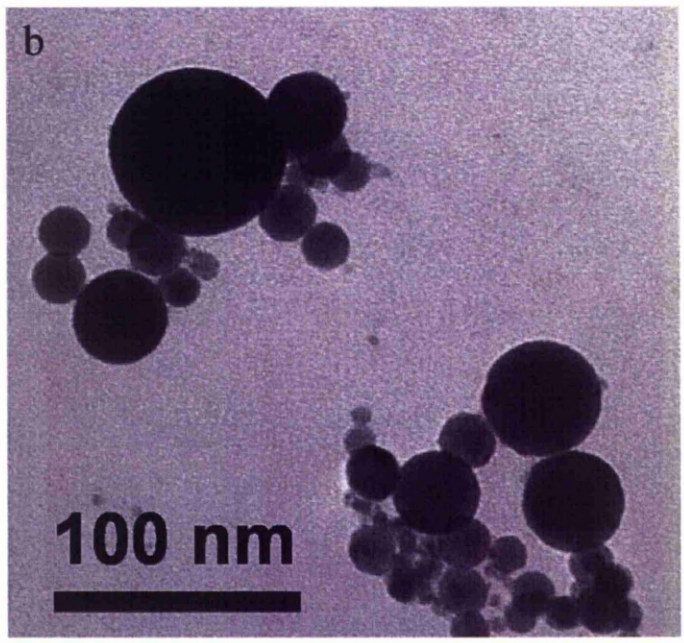


*Figure 4-8: TEM micrographs of (a) NP agglomeration around a hole of the support carbon grid and (b) small NPs clusters, produced by arc-discharge in water using a tantalum rod as anode.*

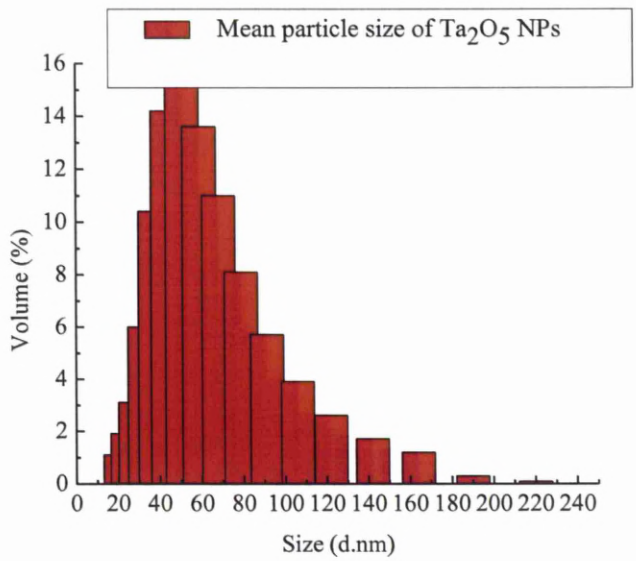


*Figure 4-9: Particle size distribution of Tantalum Oxide NPs. Mean particle size at 61 nm.*

High Resolution TEM (HRTEM) has revealed the crystalline nature of this product. Figure 4-10 (a) shows clearly the lattice fringes of a single particle (~ 23 nm diameter). Additionally, Figure 4-10 (b) illustrates three NPs, all crystalline.

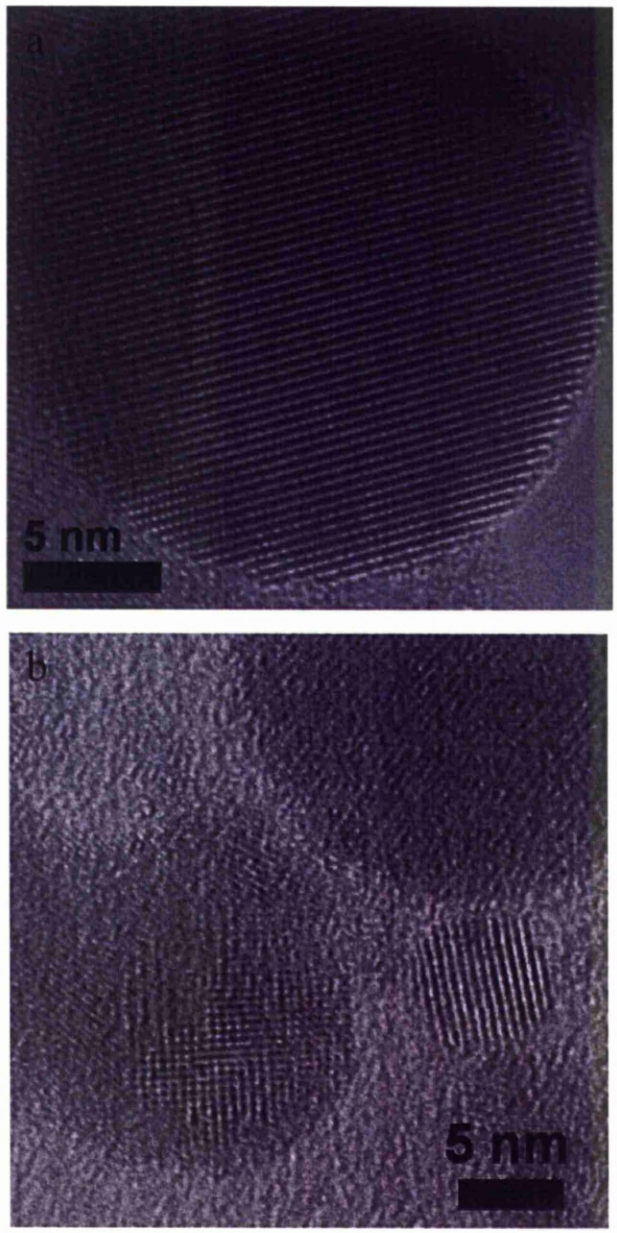


*Figure 4-10: a) Lattice fringes of a 23 nm in diameter single particle and b) crystalline structure of a 6 nm NP.*

An HRTEM (Figure 4-11 (a)) image proves the atomic structure of the particles revealing the lattice fringes of a round nanoparticle. FFT was applied to a

selected part of the image (b) to produce the digital diffraction pattern (DDP) shown in (c). The spacings and angles between the lattice fringes were calculated directly from the DDP and compared to crystallographic databases to find matching composition [28]. The values obtained for the spacings were $d_1$=0.219 nm, $d_2$ = 0.33 nm and $d_3$ = 0.232 nm and for the angles between them $\varphi_{12}$ = 142.42 °, $\varphi_{13}$ = 42.18 ° and $\varphi_{23}$ = 82.29 ° respectively. These values correspond to those for the (1 -1 -9), (0 0 10), and (1 -1 2) planes of $Ta_2O_5$ along the [0 1 1] zone axis.

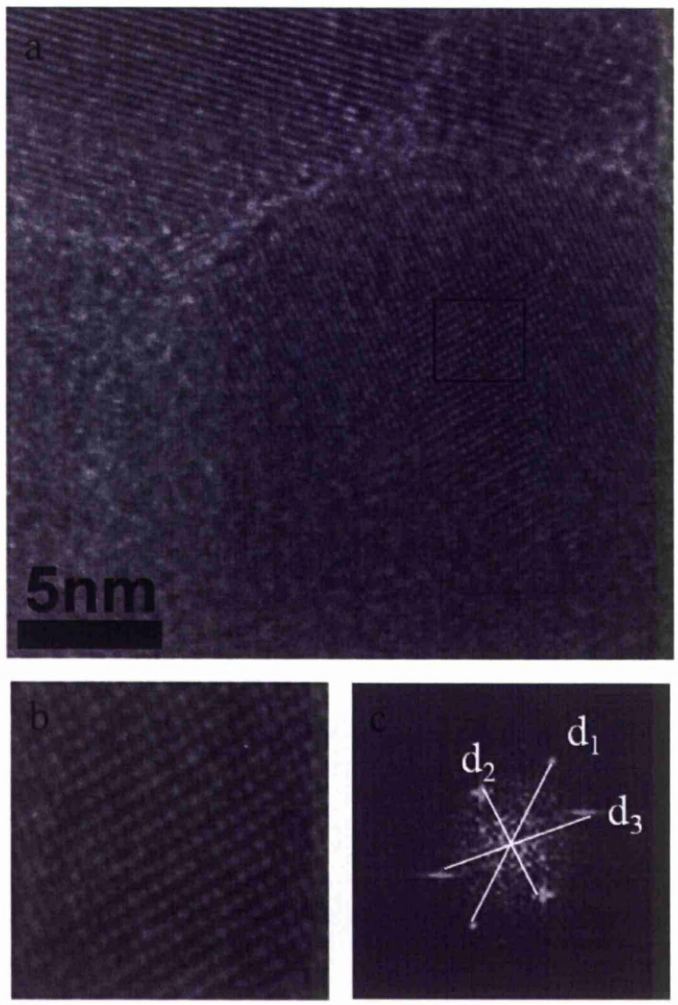


*Figure 4-11: (a) Atomic resolution micrographs of Tantalum oxide NPs. (b) Selected area to apply FFT to derive the DDP (c).*

### 4.3.2. X-RAY DIFFRACTION

The XRD spectrum of the NP powder is given in Figure 4-12. The various structures of tantalum pentoxide and their resulting diffraction patterns are very complex, with several overlapping peaks that are difficult to resolve directly using a laboratory X-ray source. However, the diffraction pattern in Figure 4-12 matches quite nicely with the $Ta_2O_5$ structure that is stable at room temperature and which is commonly referred to as "L-$Ta_2O_5$" [29]. Numerous narrow diffraction peaks are referred to in Ref. 29 but, as a result of peak overlapping (compare Figure 4-12 with the data in Ref. 28 and 29), the peaks of these XRD spectrum cannot be labeled with confidence.

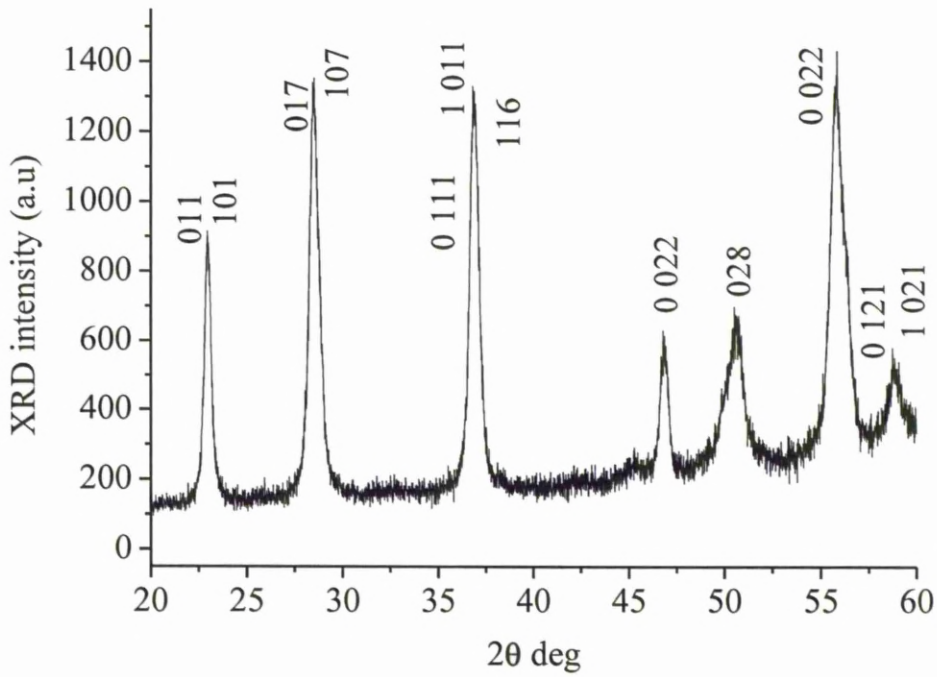


*Figure 4-12: XRD pattern of the produced nanopowder*

### 4.3.3. X-RAY PHOTOELECTRON SPECTROSCOPY

Although XRD analysis suggests a pure $Ta_2O_5$ product, the existence of carbon traces in the vapours, as it was proven by OES, imposed the need for further chemical examination of the NPs. Figure 13 (a) shows the wide scan recorded from the TaO*x* sample, where the main features detected are the XPS core level peaks of Ta, C 1s, and O 1s, as well as the X-ray-induced Auger peak O (KVV). The C 1s peak at binding energy of 284.7 eV is attributed to residual carbon usually in the graphitic form. The O 1s peak appears at 530.7 eV, which is a characteristic energy for TaO*x*. Figure 13 (b) shows the Ta 4f core level spectra appearing at 26 eV (Ta 4f7/2) and 27.5 eV (Ta 4f5/2), resulting to a spin orbit splitting of 1.8 eV agreeing with values reposted in the literature [30]. The binding energy values correspond to Ta atoms in Ta2O5. The surface atomic composition was calculated using the intensities (area) of the XPS core level peaks corrected by their sensitivity factors, which are 0.66, 0.185, and 2.4 for the O 1s, Al 2p, and Ta 4f peaks, respectively. More specifically, typical atomic concentration for the NP powder is 60% O, 30% Ta, and 10% C, with C concentration varying between 4 and 15% for different batches, modifying accordingly the O and Ta absolute concentrations.

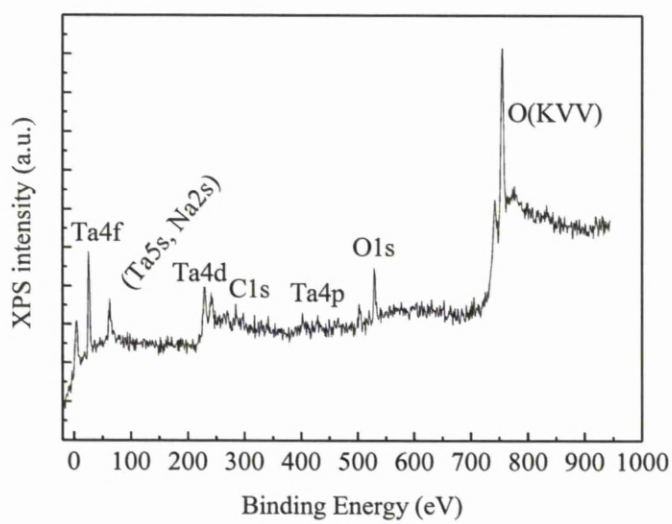


*Figure 4-13: XPS wide scan of the NP powder pressed in pallet form*

According to the XRD results, no carbon contamination from the cathode or other impurities was introduced to the chemical structure of the particles. Carbon structures were also not detected during TEM investigation. While the absence of any carbon structure is far from conclusive, the origin of carbon could be partially attributed to post-fabrication contamination. Considering a graphite layer on top of the oxide, for the TaO*x* sample, *x* equals 0.48 ± 0.05 atomic weight, adequately corresponding to the atomic proportion of Ta and O in $Ta_2O_5$.

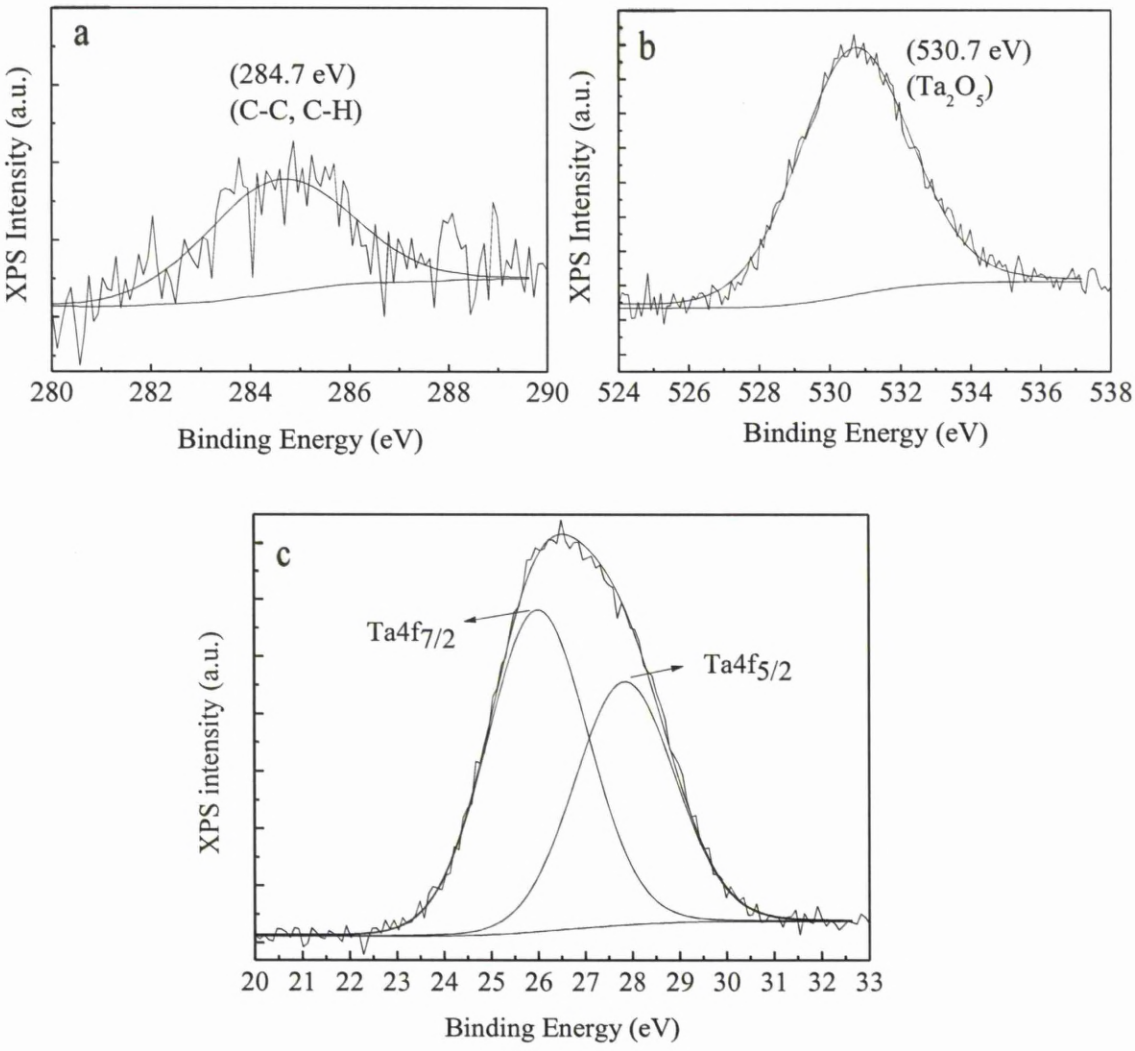


*Figure 4-14: (a) Ta 4f XPS peak and its deconvolution to Ta 4F7/2 and Ta 4f5/2. (b) O 1s XPS peak. (c) C 1s peak and its deconvolution to two components.*

## 4.4. NANOPARTICLE PRODUCTION MECHANISM

In response to an increased demand for NP production with controllable properties, such as size distribution, degree of agglomeration, chemical composition, it is herein intended to provide some fundamental understanding of the growth mechanism of nanometer-sized $Ta_2O_5$ particles synthesized by arc-discharge in water. While spheroidization of micrometre sized solid particles is clearly a melting operation [31] the sub-micrometre particles prepared by the system are formed by a different way. As has been demonstrated by OES, the vapour generated by the electrical breakdown contains in abundance O and Ta atoms which act as precursors for the tantalum pentoxide NPs. It is reasonable to assume that within the atmospheric pressure plasma increased concentration of those precursors leads to a situation of saturated vapours. In this state, any driving force that could reduce the solubility of the precursors in the vapours would create conditions of thermodynamic unstable mixture such as supersaturated vapour. It is postulated that such a driving force in the present system is associated with vapour quenching, that is by freezing-in the high temperature phase, due to plasma expansion or bubble release. This would have the effect of bringing the constituents of the vapour into contact with the surrounding water. This idea is supported by high speed images like the one in Figure 4-3. This process is continuous and self-sustained, i.e., the super-saturation is achieved without external actions such as drowning-out and increasing the interest for industrial applications.

When the degree of super-saturation is sufficient, and the reaction and condensation kinetics permit, particles will nucleate homogeneously. Once nucleation occurs, the remaining super-saturation can be relieved by condensation or a reaction of the vapour-phase molecules on the resulting particles and, accordingly, particle growth occurs rather than further nucleation. Any high temperature phases formed will be eventually frozen-in. The time span between this onset of the particle growth and the moment that the vapours are no more super-saturated determine the particle growth and thus their size. Once particles form in the gas phase, they coagulate at a rate that is proportional to the square of their number concentration and that is only weakly dependent on particle size [32]. It is underlined that OES provides indirectly a measure of the precursor concentration and becomes the only reliable signal for any possible feedback control of the process. At a sufficient high temperature, particles

coalesce faster than they coagulate and spherical particles are produced [32] such as in the case studied in this work.

## 4.5. SUMMARY

Anodic arc in water was presented as an efficient method for tantalum pentoxide nanoparticle production, without the need for costly and time-consuming cycles. Electrical and optical emission diagnosis of the system showed that this process involved anode and water atomization followed by vapour super-saturation. Spherical crystalline NPs with purity of at least 90% were synthesized, with mean diameter of about 40 nm. The extrapolation from bench scale to full production capacity of this procedure appears viable due to the low power consumption, the discharge stability, and the convenience of its execution.

## 4.6. REFERENCES


[1] G. L. Brennecka and D. A. Payne, *J. Am. Ceram. Soc.*, 89, 2089 (2006).

[2] J. F. Scott, *Annu. Rev. Mater. Sci.*, 28, 79 (1998).

[3] G. Q. Lo, D. L. Kwong, and S. Lee, *Appl. Phys. Lett.*, 60, 3286 (1992).

[4] H. Shinriki, T. Kisu, S.-I. Kimura, Y. Nishioka, Y. Kawamoto, and K. Mukai, *IEEE Trans. Electron Devices*, 37, 1939 (1990).

[5] D. A. Sager, V. Apostolopoulos, and J. S. Wilkinson, *J. Am. Ceram. Soc.*, 85, 2581 (2002).

[6] F. Rubio, J. Denis, J. M. Albella, and J. M. Martinez-Duart, *Thin Solid Films*, 90, 405 (1982).

[7] Y. Nakagawa, Y. Gomi, and T. Okada, *J. Appl. Phys.*, 61, 5012 (1987).

[8] P. M. Natishan, E. McCafferty, P. R. Puckett, and S. Michel, *Corros. Sci.*, 38, 1043 (1996).

[9] Y. Wang, Z. Cui, and Z. Zhang, *Mater. Lett.*, 58, 3017 (2004).

[10] S. Sun, C. B. Murray, D. Weller, L. Folks, and A. Moser, *Science*, 287, 1989 (2000).

[11] C.-C. Tu, Y.-K. Li, T.-M. Chen, and C.-Y. Wu, *IEEE Trans. NanoTechnol.*, 5, 284 (2006).

[12] Y. Takeda and N. Kishimoto, *Nucl. Instrum. Methods Phys. Res. B*, 206, 620 (2003).

[13]. H. Kominami, M. Miyakawa, S.-y. Murakami, T. Yasuda, M. Kohno, S.-i. Onoue, Y. Kera, and B. Ohtani, *Phys. Chem. Chem. Phys.*, 3, 2697 (2001).

[14] O. Böhme, A. L. Spetz, I. Lundström, and D. Schmeißer, *Adv. Mater.*, 13, 597 (2001).

[15] D. V. Szabó, R. Ochs, S. Schlabach, E. Ritzhaupt-Kleissl, and T. Hanemann, *Mater. Res. Soc. Symp. Proc.*, 1056E, 1056-HH10-09 (2008).

[16] D. Delaportas, P. Svarnas, I. Alexandrou, E. Siokou, K. Black, and J. W. Bradley, *J. Phys. D*, 42, 245204 (2009).

[17] N. Pinna, G. Garnweitner, M. Antonietti, and M. Niederberger, *Adv. Mater.*, 16, 2196 (2004).

[18] Yu. P. Raizer, *Gas Discharge Physics*, p. 245, Springer-Verlag, New York (1997).

[19] P. Bruggeman and C. Leys, *J. Phys. D*, 42, 053001 (2009).

[20] F. Garrelie, C. Donnet, A. S. Loir, and N. Benchikh, *Proc. SPIE*, 6261, 62610L (2006).

[21] S. B. S. Heil, F. Roozeboom, M. C. M. van de Sanden, and W. M. M. Kessels, *J. Vac. Sci. Technol. A*, 26, 472 (2008).

[22] National Institute of Standards and Technology (NIST), Atomic Spectra Database.

[23] D. Grojo, J. Hermann, and A. Perrone, *J. Appl. Phys.*, 97, 063306 (2005).

[24] C. G. Parigger, M. Dackman, and J. O. Hornkohl, *Appl. Opt.*, 47, G1 (2008).

[25] J. Musil, J. Matouš, and A. Rajskú, *Czech. J. Phys.*, 43, 533 (1993).

[26] I. Wenåker, *Phys. Scr.*, 42, 667 (1990).

[27] R. Khalid, K. Yaqub, S. Yaseen, S. Javeed, A. Ashraf, S. A. Janjua, and S. Ahmad, *Nucl. Instrum. Methods Phys. Res. B*, 263, 497 (2007).

[28] D. A. Fletcher, R. F. McMeeking, and D. Parkin, *J. Chem. Inf. Comput. Sci.*, 36, 746 (1996).

[29] N. C. Stephenson and R. S. Roth, *Acta Crystallogr., Sect. B: Struct. Crystallogr. Cryst. Chem.*, 27, 1037 (1971).

[30] D. Briggs and M. P. Seah, *Practical Surface Analysis*, John Wiley & Sons, New York (1990).

[31] R. McPherson, *J. Mater. Sci.*, 8, 851 (1973).

[32] M. T. Swihart, *Curr. Opin. Colloid Interface Sci.*, 8, 127 (2003).

# 5. COPPER OXIDE- TANTALUM OXIDE (CORE-SHELL) NANOPARTICLE PRODUCTION

## 5.1. TANTALUM/COPPER ANODIC TYPE ARC

Up to this point, the production of metal oxides with the arc discharge in water method has been successfully proven for the cases of aluminium and tantalum oxides with dielectric constants of ~10 [1] and ~25 [2], respectively. However, in order to produce materials with higher dielectric constant, composite metal oxides are considered to be the prime candidates. As mentioned before, materials like barium titanate $BaTiO_3$, (dielectric constant up to ~1300 [3]) have attracted huge interest from many research groups all over the world since they can be used in super-capacitors or as gate dielectrics in many electronic components. Renner B et.al [4] published a paper in 2004 studying the dielectric properties of $Cu_2Ta_4O_{12}$.

Figure 5-1 shows that for a variety of temperature and frequencies the dielectric constant is between the values of $10^2$ and $10^4$. This fact was the inspiring factor to reproduce this chemical composition in NPs using the arc-discharge method. In addition, the arc system has only been used once with composite targets so far; a Ni:C composite target was used to form carbon encapsulated Ni nanoparticles. Therefore, the use of Ta:Cu composite electrode offered the possibility to shed light into the evolution of nanoparticles and the relation of their composition to the composite electrode.

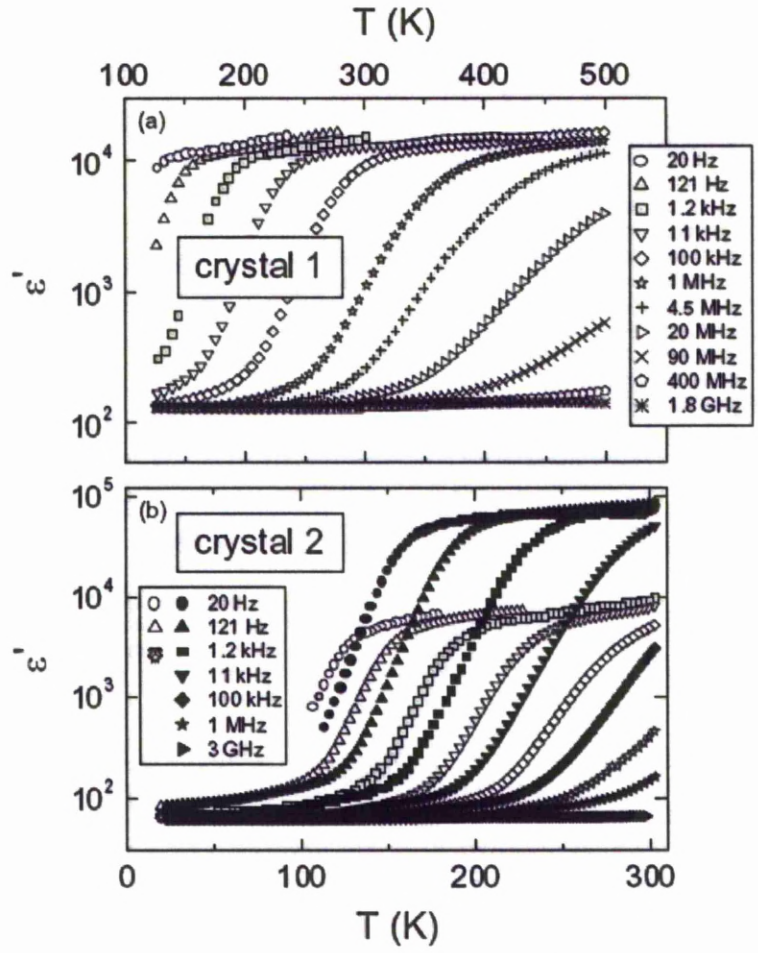


*Figure 5-1: Temperature-dependence of the dielectric constant of two crystals of $Cu_2Ta_4O_{12}$ at different frequencies [4].*

The evaporation and condensation of tantalum in the arc plasma has already been studied in this work. Moreover, it would be interesting to investigate if the process dynamics change when tantalum and copper are evaporated from the composite anode and their atoms coexist in the condensing vapour, taking into account the production mechanism proposed for metals oxides, where the anode is evaporated due to high power to the atomic level and the resulting vapour condenses to nanoparticles while simultaneously reacting with oxygen to form the oxide. Reactive oxygen species are produced due to the hydrolysis of the water. It might be expected that copper would either participate to this reaction by bonding with tantalum and oxygen or the two metals will form separate oxide NPs. The latter mechanism is not be desirable when trying to produce dielectric particles because

copper oxide is a p-type semiconductor with a narrow band gap of 1.2 eV, thus providing conduction paths for leakage current through the dielectric.

## 5.2. EXPERIMENTAL DETAILS

Previous experiments with aluminium and tantalum anodes were performed using pure metal rods as the anode. In the case of the composites, the metal anode was prepared in-house. Powders of both metals were purchased from Micrometals Ltd. (~ 99% purity, 1-5 um particle size) and were mixed by mechanical stirring. The tantalum / copper ratio was 2:1. The reason for using this ratio was that the initial goal was to create $Cu_2Ta_4O_{12}$. The mixed powder was poured in a metal crucible (stainless steel) and was compressed using a computer control electro-hydraulic compression testing machine to form a solid tablet. The compression force was 100 kN and the electrode area was 5.5 cm in diameter.

The conductive stainless steel crucible was then attached to the positive electrode. A schematic diagram of the modified system is illustrated in Figure 5-2.

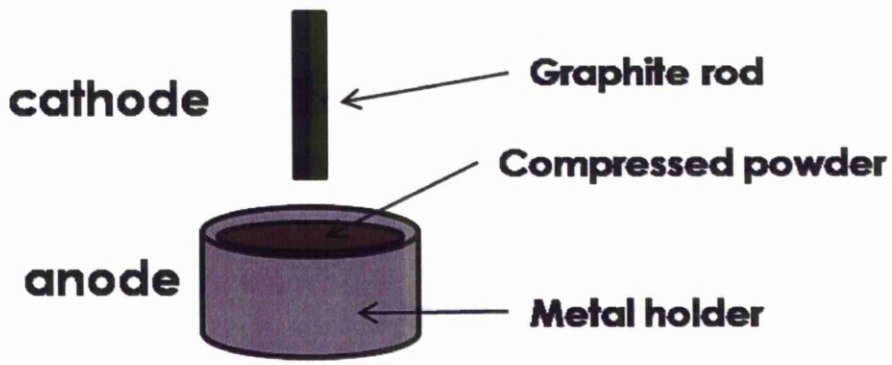


*Figure 5-2: Schematic diagram of the modified system to produce composite dielectric NPs.*

## 5.3. DISCHARGE CHARACTERISTICS

### 5.3.1. ELECTRICAL CHARACTERISTICS

Figure 5-3 depicts the electrical characteristics of a 35 A arc discharge. As soon as the two electrodes come into contact the arc potential drops instantly from ~ 82 V (open circuit voltage) to 25 V. The voltage remains relatively stable at 25 V for the first two seconds and then it drops over a few milliseconds almost to zero. The same incident happens near the discharge time values of t = 4 and t = 8 s. These abnormalities occur when the plasma literally melts part of the anode, bridging part of the inter-electrode space with conductive material for a short period of time causing minor short circuits. On the other hand, the voltage can also rise instantaneously (t = 6 s). At that point, the assumption is that the inter-electrode distance has increased across part of their surface due to anode erosion by the arc. This means that the discharge potential needs to increase for the current power supply to maintain the 35 A constant current set by the source. Existing conductive paths help to maintain the arc and such processes are mainly responsible for the erratic movement of the arc over the anode. A combination of these fluctuations is noticeable towards the end of the arc, after about eight seconds of the discharge time, where the distance between anode and cathode has increased and the arc cannot be sustained further. The current value is usually close to the pre-set value (here 35 A) but its time variation also reflects the local variation in the discharge properties, albeit at a diminished magnitude than the voltage fluctuations. The average arc duration of the discharge is ~10 s and the consumed power follows the multiplication of the voltage and the current (usually ~ 1 kW).

Compared to the previous experiments, the emitted light of the discharge was not recorded by a photomultiplier. The reason is that the produced material has a dark brown colour and as the arc progresses the liquid around the arc becomes rapidly darker. The rapidly diminishing liquid transparency renders any long lasting luminous measurements unreliable.

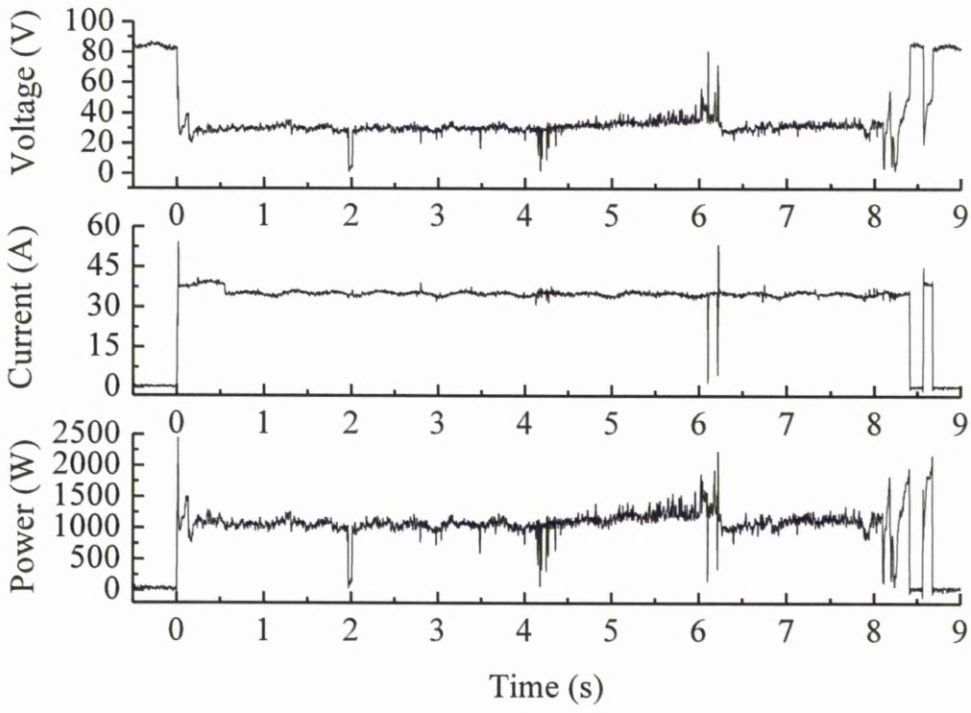


*Figure 5-3: Electrical characterization of copper-tantalum arc-discharge*

### 5.3.2. HIGH-SPEED IMAGING

Micrographs of time-resolved high speed imaging are shown in Figure 5-4. Normally, the camera would be placed horizontally, facing the edges of the electrodes, but in this case, since the composite anode is inside a crucible the camera was positioned at a 20° angle in order to view the contact point of the discharge. The system was set to record at 125 frames per second (fps) (frame interval 8 ms) and the particular arc lasted for approximately 3 s. The camera was synchronized to start recording when the voltage dropped below the 60 V; i.e. when the plasma is established. The first image was recorded at zero point and the last one when the arc had extinguished.

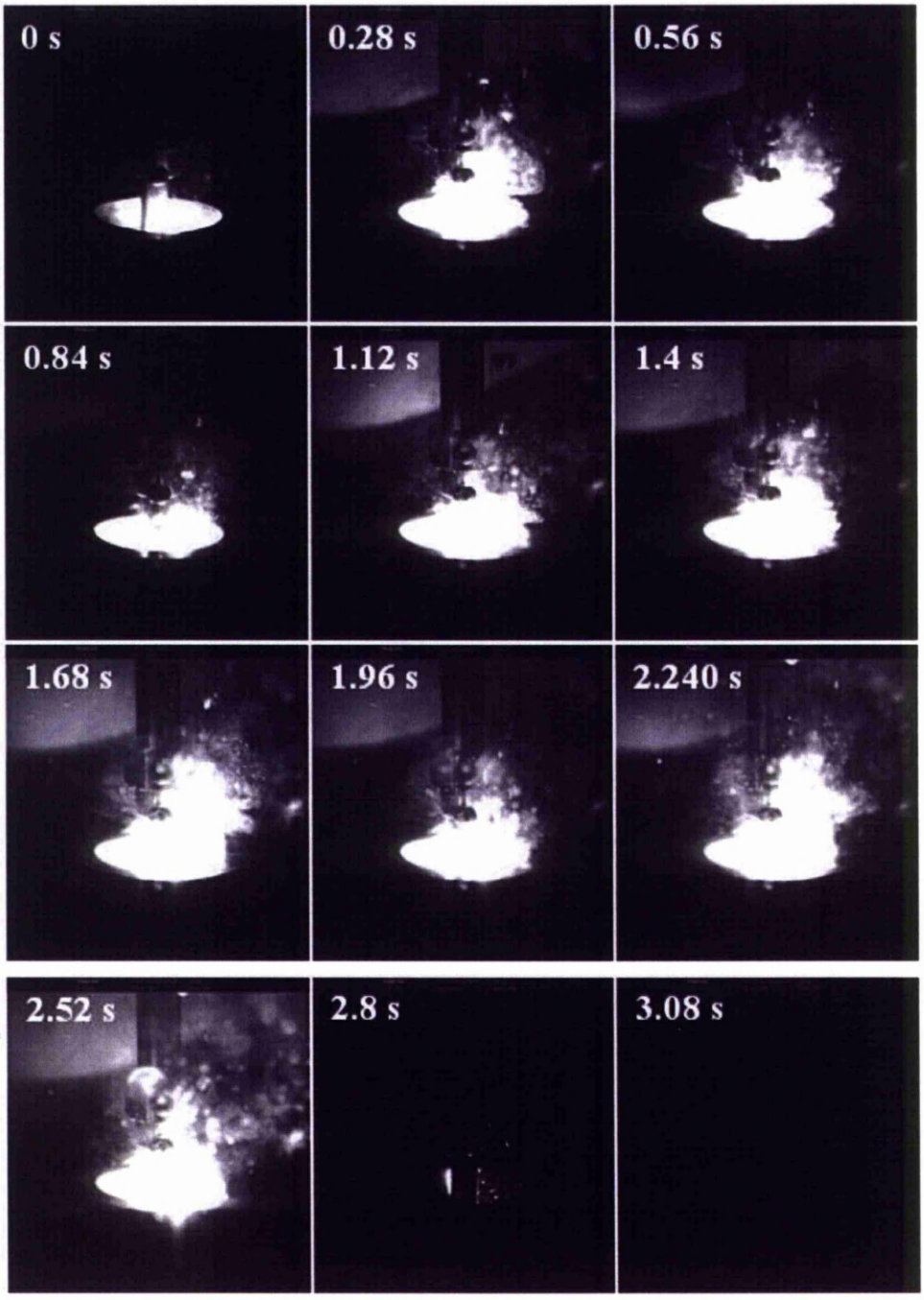


*Figure 5-4: Evolution of the arc-discharge using high-speed imaging of Tantalum/Copper arc-discharge in water*

The selected images presented are for every 0.28 s. The light intensity was constantly changing according to the number of conductive paths. Several paths are

active simultaneously across the surface of the electrodes and the more paths exist the more intense is the emitted light. From the whole ~ 3 s arc, plasma is more active at 1.68 s. Water bubbles are constantly formed, due to local pressure, and they are escaping towards the surface of the beaker. The light decreases rapidly during periods that the arc current decreases momentarily.

### 5.3.3. OPTICAL EMISSION SPECTROSCOPY (OES)

OES was applied to the present system. The entrance to the spectrometer was also placed in a 20° degrees angle (similarly to the high speed-camera) aiming at the core of the plasma. The spectrum extends from 200 nm to 850 nm wavelength. Due to the rapidly increasing opacity of the liquid, the whole spectrum (captured in 100 nm segments) was recorded after changing the water so that the data was free from absorption/scattering by the liquid.

Figure 5-5 depicts the same wavelength region (450-550 nm) from two different runs of the discharge. It can be said that the only difference between the two shots is merely in optical emission intensity (counts) showing that the plasma composition is similar between the different arcs. The marked emission lines represent the Cu I at 510.5 nm, 515.3 nm and 521.8 nm.

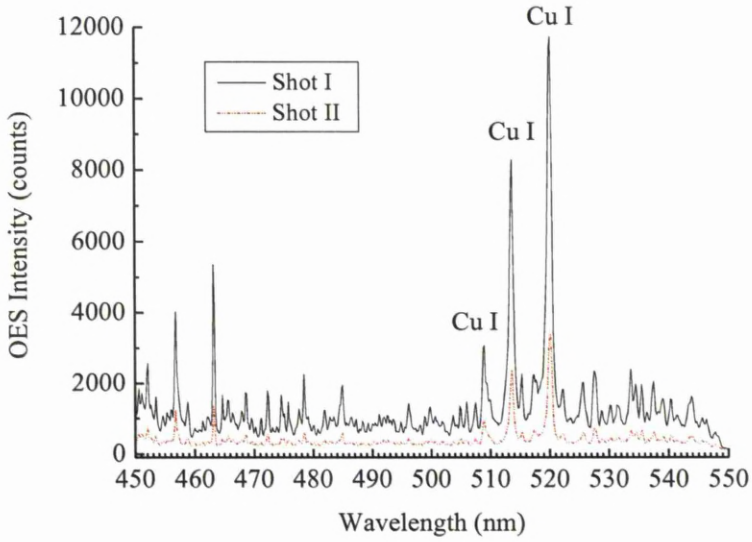


*Figure 5-5: Two snapshots from the same spatial region (450-550 nm) for the Cu:Ta arc discharge.*

Figure 5-6 shows the optical emission raw spectrum from 200 – 850 nm. This spectrum reveals all the energetic species that exist in the plasma. Similarly to previous experiments, thermal anode evaporation takes place where tantalum and copper atoms pass to the gaseous phase, becoming either ionized or excited. For tantalum, Ta (326, 02 and 331.79 nm) and $Ta^+$ (383.37 nm) lines [5] were observed in the spectrum. Copper lines were more discrete. Cu II ionic line (224.7 nm) and Cu II (229.4) as well as Cu I resonance (324.7 and 327.3 nm) lines and Cu I (510.5, 515.3, 521.8, 570.02 and 578.21 nm) lines [6-8] proved the evaporation and atomization of the copper in the anode. Moreover, secondary active species, such as atomic oxygen (777.53 nm) and single-ionized atomic oxygen (718. 2 nm) [9] and hydrogen emission lines ($H_\alpha$ 656.28 nm, $H_\beta$ Balmer) [10] can be seen, which are produced during water hydrolysis by the discharge. Finally, carbon swan bands were also identified; their origin being trace amounts of carbon due to cathode evaporation [11].

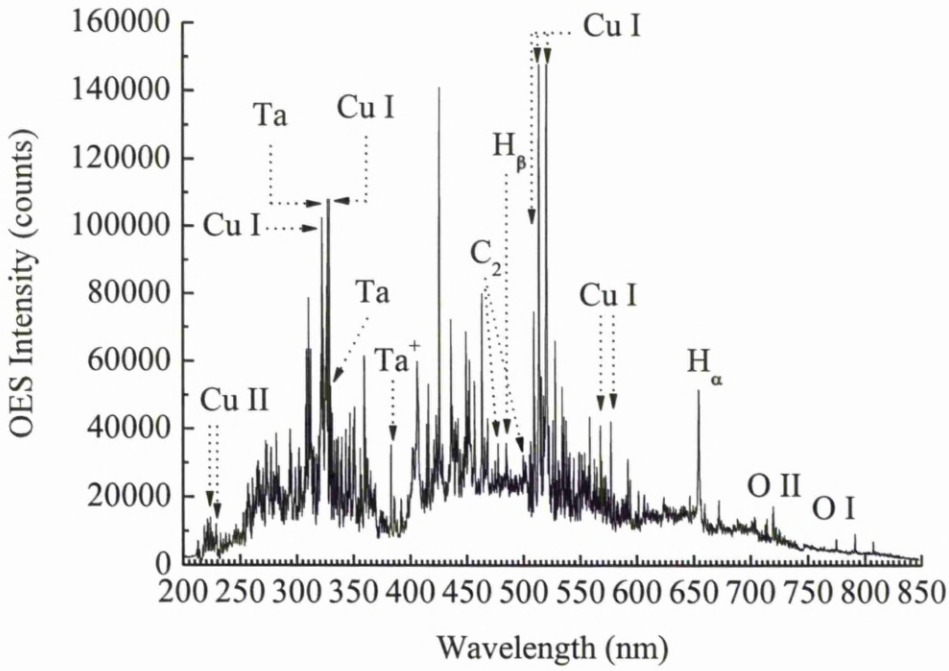


*Figure 5-6: Optical emission (UV-visible) raw spectrum of the Ta-Cu–C arc-discharge in water*

### 5.3.4. ELECTRODE MASS REDUCTION

The electrode mass reduction was calculated after several timed arc runs and by measuring the weight of the anode and cathode, before and after the discharges. The images below (Figure 5-7 a, b) show the deformation of the electrodes after a few runs for an arc current of 35 A. The flat, smooth surface of the as-compressed anode (see the outer part of the anode in Figure 5-7 a) was altered mainly due to melting of the composite during the arc. A similar surface modification can be seen on the cathode where the most evident effect is re-deposition or melt transfer of anode material onto the cathode.

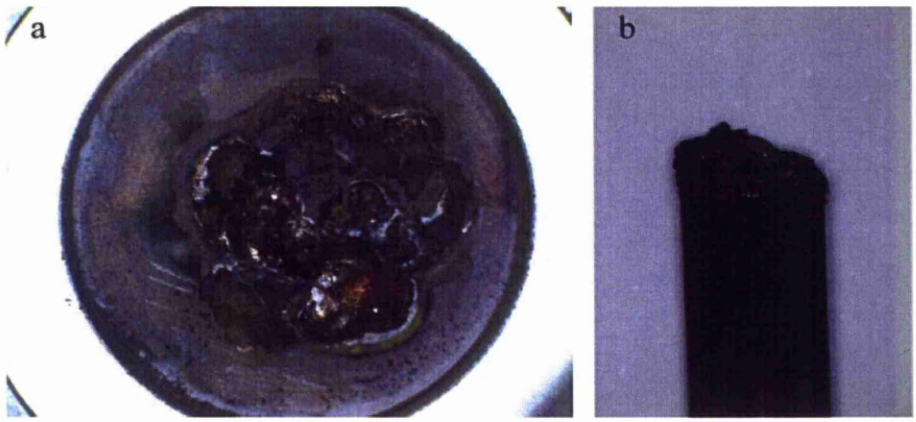


*Figure 5-7: Indicative photos of (a) the anode (tantalum/copper compressed powder) and (b) cathode (carbon rod) arc several arc runs.*

The mass of the cathode changed in a similar fashion to previous experiments: its weight increased (negative mass reduction rate) at a pace of -3.62 mgr/s (± 2.56 mgr/s). On the other hand, the anode had a significant loss of weight (positive mass reduction) of 36.14 mgr/s (± 23.78 mgr/s). This high loss of mass of the anode can be explained since the composite powder was in fact a mechanically compressed powder and not a true solid. The high energy of the plasma and the turbulent liquid at the vicinity of the arc could disturb the powder resulting in the loss of primary material in addition to the material evaporated during the discharge. However, after a few ten of seconds of the arc discharge the melted anode surface provides a very stable electrode.

## 5.4. NANOPARTICLE CHARACTERISATION

The samples were examined y means of TEM imaging, image corrected HRTEM, STEM imaging, EDX mapping, XRD and XPS analysis. Due to the complexity of the product, extensive examination was essential not only in terms of nanoparticle imaging but also to derive the chemical composition of this composite material.

### 5.4.1. HIGH RESOLUTION TRANSMISSION ELECTRON MICROSCOPY (HR-TEM)

Initial low magnification TEM investigation showed clusters of nanoparticles with a peculiar structure. Figure 5-8 (a) and (b) shows representative clusters of the nanoparticles. The particle size distribution varied from 5 nm to 50 nm with an average particle size below 20 nm, significantly smaller than previous experiments on $Al_2O_3$ and $Ta_2O_5$ NPs. The agglomeration was significant; a common feature among gas phase NP production. The contrast of the outer side of the particles appeared to be much stronger than the inner area. Usually, contrast differences reveal variations in either mass/density or crystalline structure. The images in Figure 5-8 can be interpreted by either assuming a core/shell structure or hollow spheres.

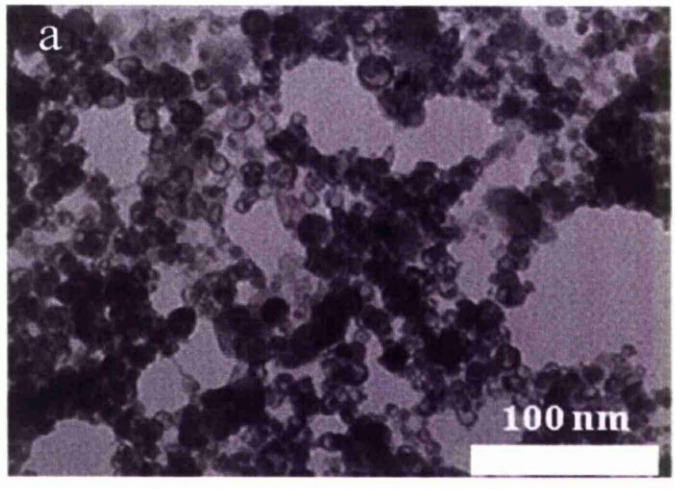

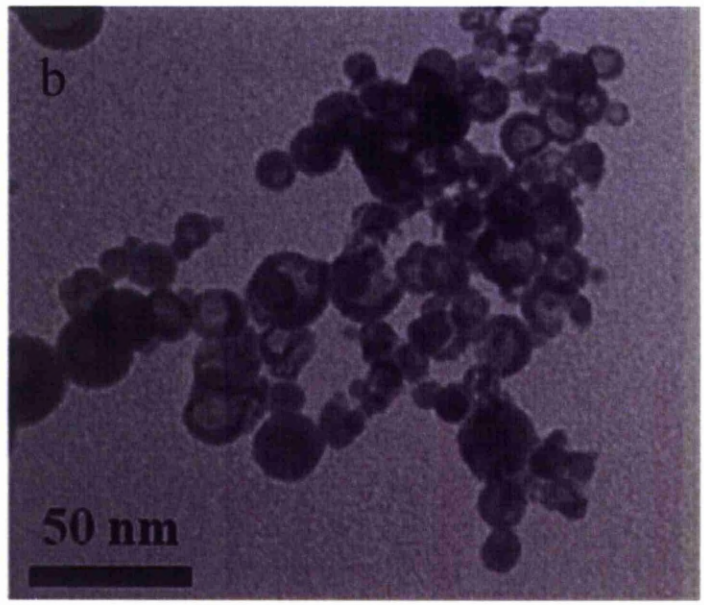


*Figure 5-8: Low magnification TEM images of NPs produced by arc-discharge using Cu:Ta anode in water.*

The microstructure of single particles is shown in the HREM images captured by a monochromated Cs image corrected 'cubed' Titan[3] 60-300 FEG S/TEM at an acceleration voltage of 300kV (Figure 5-9 (a), (b)). Lattice fringes are well resolved across the whole nanoparticle and some weak phase contrast is evident between the centre and the perimeter. Based on these images, the assumption that the NPs are hollow spheres is rejected. Figure 5-9 (a) depicts the difference at the cross fringes of a single particle.

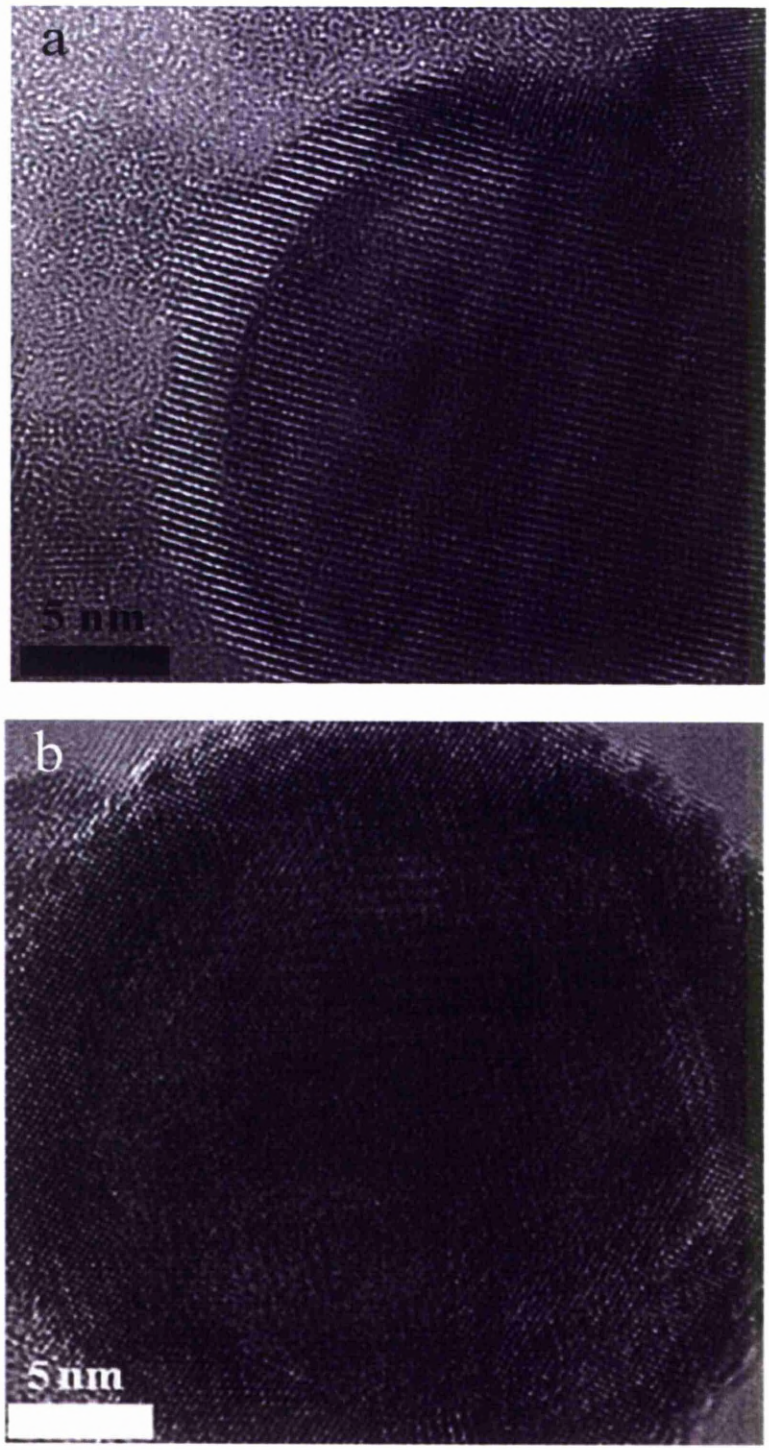


*Figure 5-9: HRTEM micrographs of the core/shell particles*

In TEM imaging the geometric spherical aberration (Cs ~ 1.2mm) means that each image contains interference information with an apparent depth of focus of

several tens of nm at optimum defocus value. In other words, the image produced is a projection of all the planes of the particle. In the case of a core/shell NP, the shell is clearly shown along the perimeter of the particle whereas in the core, both core and shell lattice fringes interfere, creating a complex crystallographic net.

The micrograph in Figure 5-10 illustrates a particle examined by 'through focal series'. The reduced geometrical aberration (Cs < 300 nm) means the imaging is at or near Gaussian focus and the depth of focus is reduced to less than 10 nm. Therefore, it is possible to acquire images where the periodicities of the core and the cell are faithfully transferred. In practice, such images are easier to acquire using an automatic through focus series software, to record about 30 images and subsequently pick the appropriate one. However, full and detailed analysis requires the reconstruction of the exit wave-function, a process that is not presented here. Figure 5-10 (a) shows a micrograph where different crystallographic orientations along one plane are present. Moreover, the marked areas (b, c) reveal different Digital Diffraction Patterns (DDP) derived from the core and shell which in turn correspond to different crystallographic structures. The variation in diffraction patterns (digital or otherwise) is perhaps the most convincing way to prove the true existence of core-shell structures by means of bright field TEM.

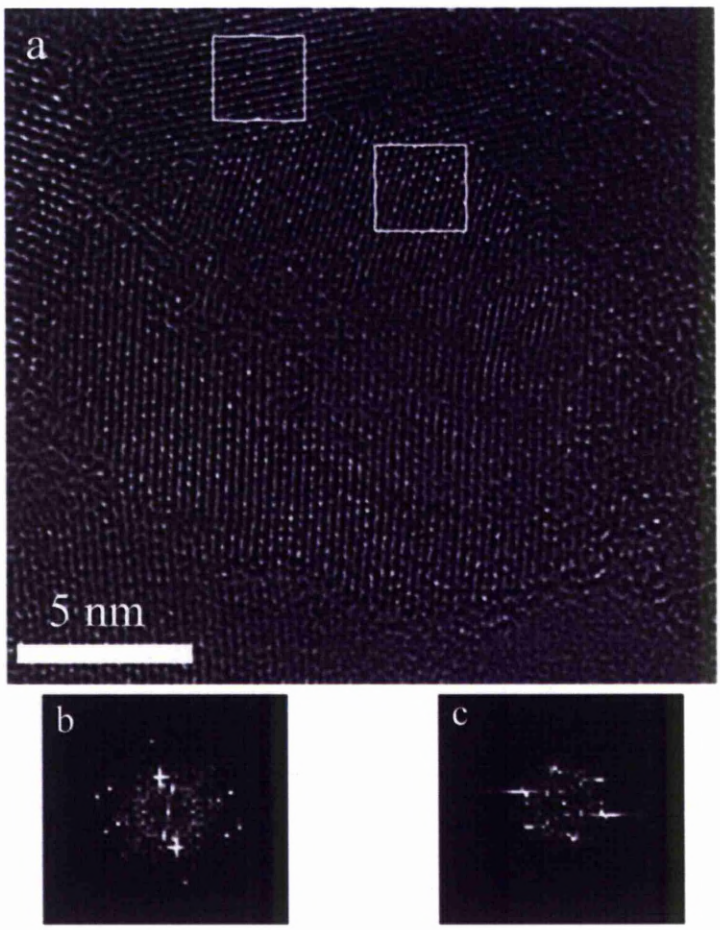


*Figure 5-10: a) Atomic resolution TEM image of a crystalline $Ta_2O_5$/CuO NP. The shell thickness appears to be below 4 nm. Marked areas (b and c) showing the difference in the DDPs between the core and shell.*

### 5.4.2. HIGH RESOLUTION SCANNING TRANSMISSION ELECTRON MICROSCOPY (HR-STEM)

To further investigate the microstructure and the chemical composition of the material produced by arc-discharge between the tantalum/copper anode and the carbon cathode, examination of the NPs was performed using a STEM probe. In this case, a monochromated Cs probe corrected 'cubed' Titan$^3$ 80-300 FEG S/TEM at an acceleration voltage of 300kV was used. High Angle Annular Dark-Field Imaging (HAADF) and Energy Dispersive X-Ray Spectroscopy (EDX) were used to explore the chemical composition of the nanoparticles.

### *5.4.2.1. High Angle Annular Dark-Field Imaging (HAADF)*

The complexity of the sample composition was further investigated by STEM HAADF imaging in order to explore the Z-contrast between Cu and Ta atoms. This technique is highly sensitive to variations in the atomic number of elements in the sample. The higher the atomic number of an element, the higher contrast illustrated on HAADF image.

Figure 5-11 (a) and (b) show low magnification images of the nano-powder. It is interesting to note the significant contrast between the shell and the core. Taking into account the atomic numbers of tantalum (Z=73) and copper (Z=29), a first conclusion would be that the particles of a Cu core surrounded by a Ta shell.

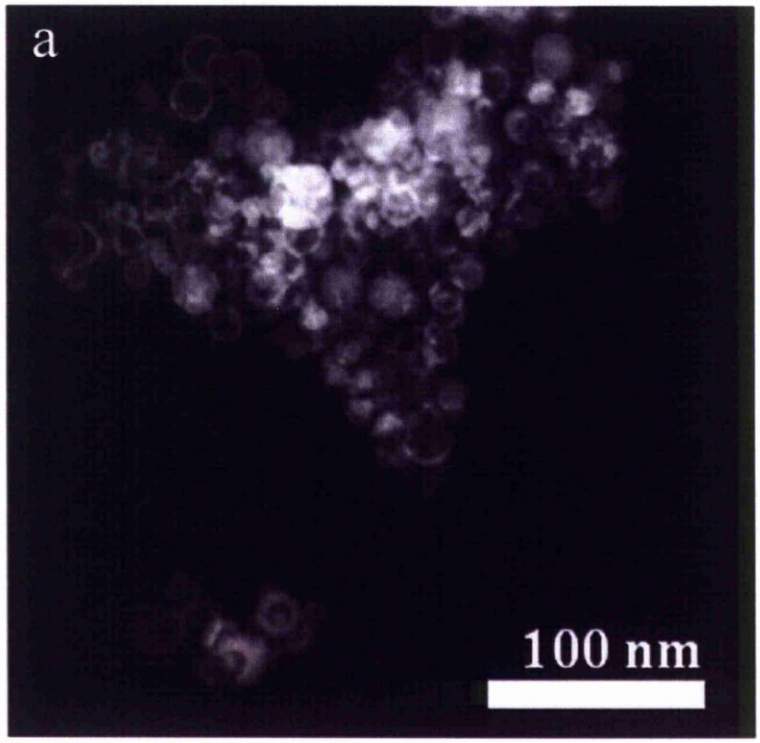

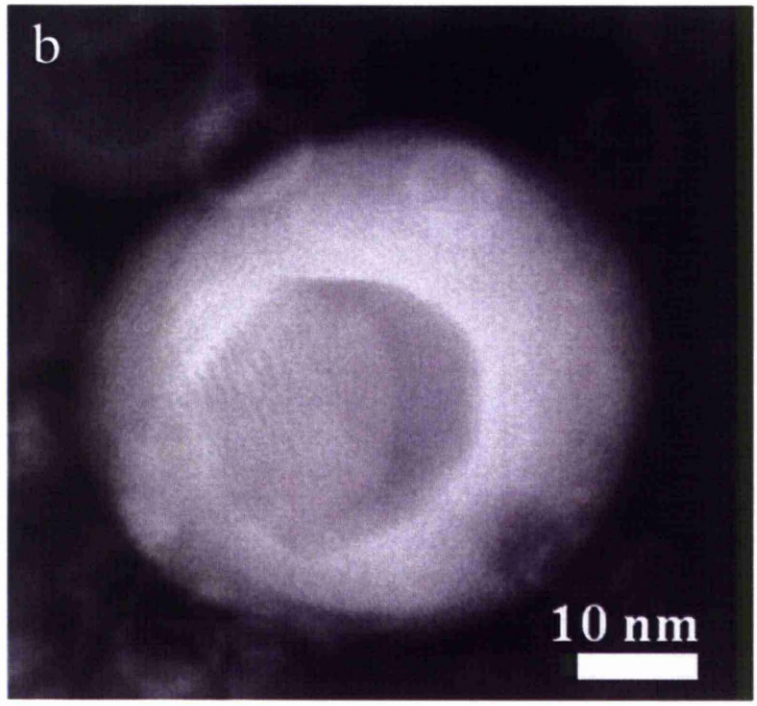


*Figure 5-11: Low magnification HAADF micrographs of core/shell NPs.*

Atomic resolution STEM was performed to further justify the above findings. The contrast difference is clearly seen in Figure 5-12 where the shell atoms are significantly brighter than the core ones. The shape, size and plane of focus of the probe in probe-corrected STEM depends strongly on objective focus and for given imaging conditions the image represents the structure and composition of the structure within a thin layer (< 5 nm) from the plane on which the probe is focused.

Figure 5-12 (a) shows an HAADF image of a core-shell nanoparticle where the shell is imaged with most clarity. There is a decreased contrast level due to the signal from electrons being scattered by the carbon contamination (appearing as a white cloud over the image), but neverthelss there is a clear contrast difference between the core and the shell. The much stronger contrast from the shell suggests that it consists of heavier elements than the core. Combining this information with the results from the XRD data, it seems likely that the core shell nanoparticles consist of a $Ta_2O_5$ shell around a CuO core.

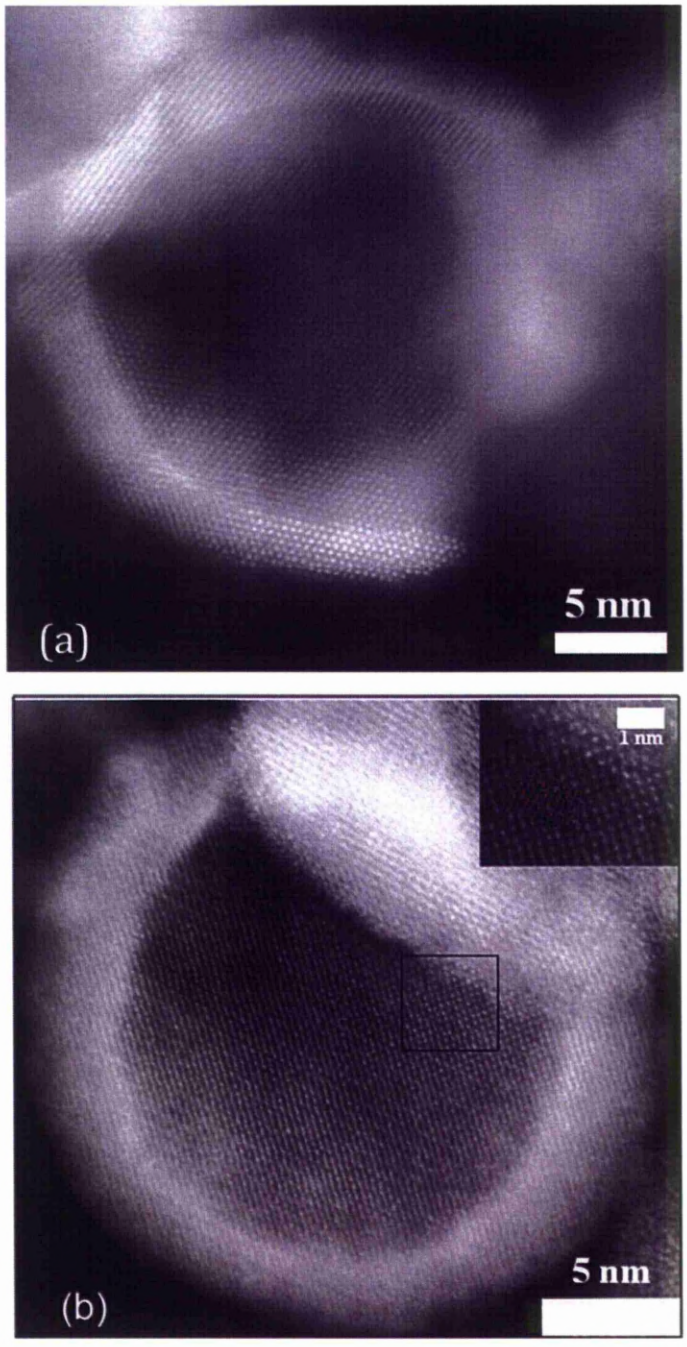


*Figure 5-12: HAADF STEM images from core-shell nanoparticles where the atomic structure is best resolved in (a) for the shell and in (b) for the core. The CuO lattice viewed along [101] is overlayed on the HAADF image in the inset of (b),with Cu atoms in red and O in blue.*

One approach to support this hypothesis is to use atomic resolution images to extract the digital diffraction pattern (DDP) as the fast Fourier transform (FFT) of the image and compare that with the diffraction pattern of prospect materials. Even though this is an approach usually followed for studying materials examined by bright field TEM, HAADF images are much better suited since atomic resolution images in STEM also offer atomic number (Z-) contrast.

However, the acquisition of images in STEM is more cumbersome because a major zone axis needs to be parallel to the optical axis. In bright field (BF) TEM, lattice fringes will be imaged even if there is mismatch between the zone axis and the optical axis. Figure 5-12 (b) shows an HAADF image acquired using a Cs-probe corrected Titan at an acceleration voltage of 300 kV, a camera length of 91 mm, a convergence angle of 24 mrad and a beam current of 60 pA. In this image, the core is well aligned with its zone axis parallel to the optical axis but the same is not true for the shell. Due to the absence of contamination the contrast between shell and core faithfully represents the ratio of atomic (Z) numbers of Ta and Cu, respectively. The ratio between the shell and core intensities is comparable to $(Z_{Cu}/Z_{Ta})^{1.7} = (73/29)^{1.7} = 4.8$, the latter being the theoretical intensity ratio ($2^3$). The area defined by the square in Figure 5-12 (b) was used to calculate the DDP for the core crystal, revealing that the core is CuO imaged along the [101] zone axis. The inset in Figure 5-12 (b) shows the HAADF image with the CuO crystal model along [101] superimposed on the image. The distance between Cu and O columns is 0.07 nm, which below the resolution limit of the image at the current magnification, resulting in the two columns imaged together in an elongated dumbell-line shape.

Figure 5-13 shows a histogram of HAADF intensity along the line (x-axis measured in nanometers). The core is imaged at almost half the Z-contrast compared to the shell; corresponding well to the variation in atomic numbers between tantalum and copper. The attached graph shows the intensity profile along a 52.5 nm line of atoms.

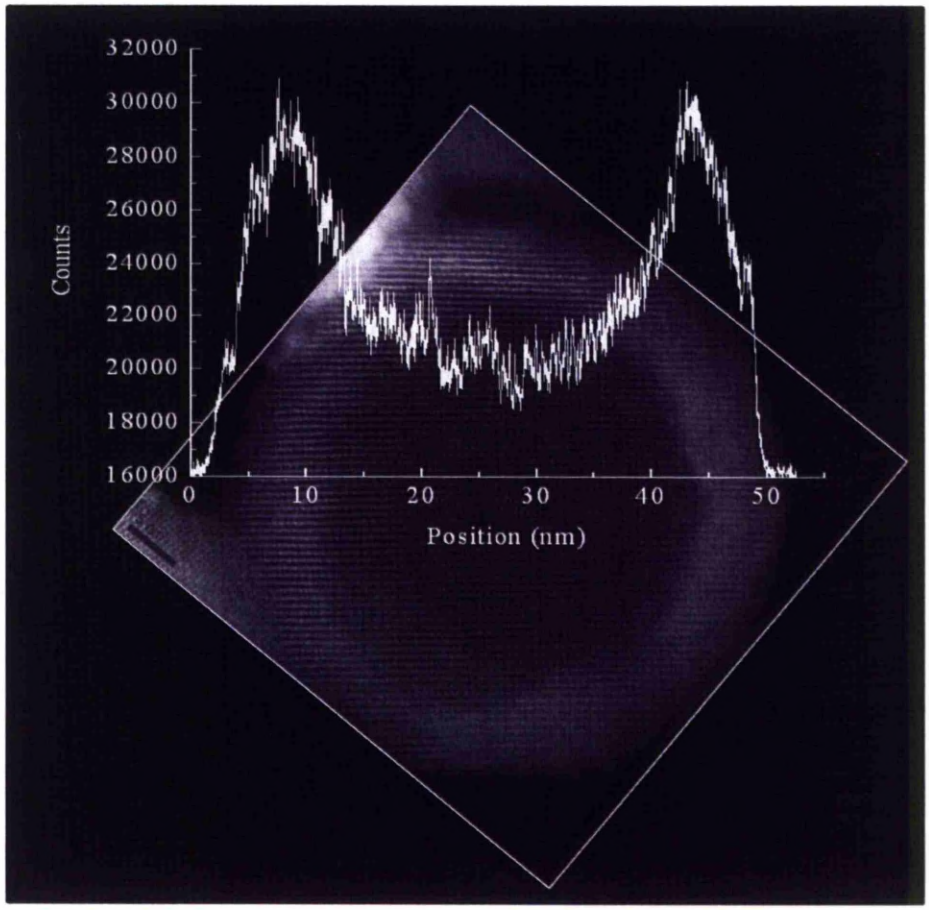


*Figure 5-13: Atomic resolution image with an embedded graph illustrating the intensity profile along a line of atoms (52.5 nm).*

### *5.4.2.2. Energy-Dispersive X-Ray Spectroscopy (EDX)*

The composition of the sample was further examined using drift corrected EDX chemical mapping. Figure 5-14 (a) shows a STEM micrograph of core/shell cluster with a line (22.7 nm long) over a single particle indicating the line scan at a step of 0.69 nm. To obtain the EDX image without the influence of the specimen drift, drift correction was applied every 30 s using the part in the yellow quadrangle. Figure 5-14 (b) and (c) show the reference and the last HAADF image, proving that sample drift was in the order of 1 nm during 2 min acquisition.

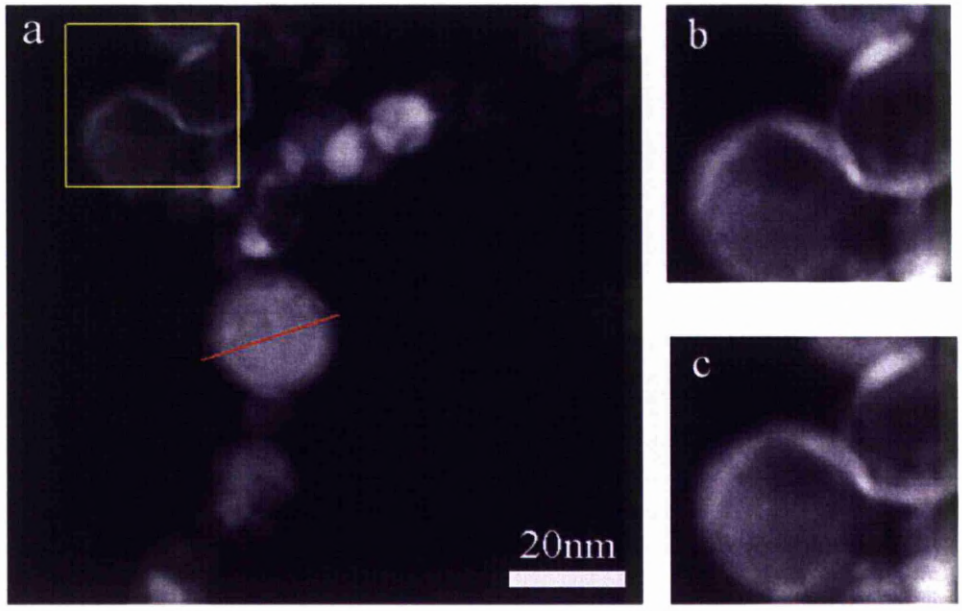


*Figure 5-14: EDX line scan on a core-shell particle (a). Drift correction was applied during scanning taking as reference image the marked area. Screenshots before (b) and after (c) the line scan show no significant movement of the examination area.*

Figure 5-15 illustrates the EDX spectrum from 0 to 12 keV, captured at the centre of the particle (6 nm from the start of the line scan). The emission lines of tantalum, copper, oxygen and carbon are clearly seen. The detected carbon originates from amorphous carbon support film. All data from the line scan are plotted in Figure 5-16 in the energy range between 0 and 2.25 keV; a region where all the elements have discrete peaks. Following the line scan from one end of the particle to the other, the Ta line is initially the only major peak. When the core of the particle is scanned, the Ta peak intensity decreases while the Cu peak intensity is becoming significant. Based on this data, the proposition of core-shell structure with a Cu:O core and a Ta:O shell is justified.

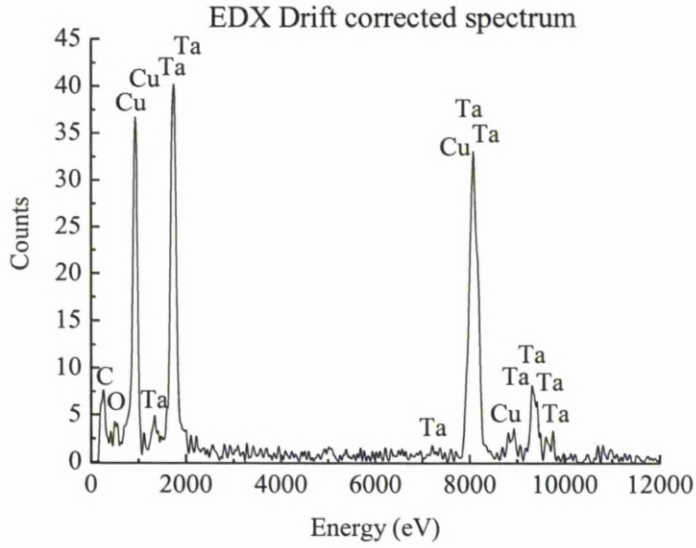


*Figure 5-15: EDX scan (0 to 12 KeV) derived at 6.01 nm position. The elements found are tantalum, copper, oxygen and carbon (the latter due to the amorphous carbon support).*

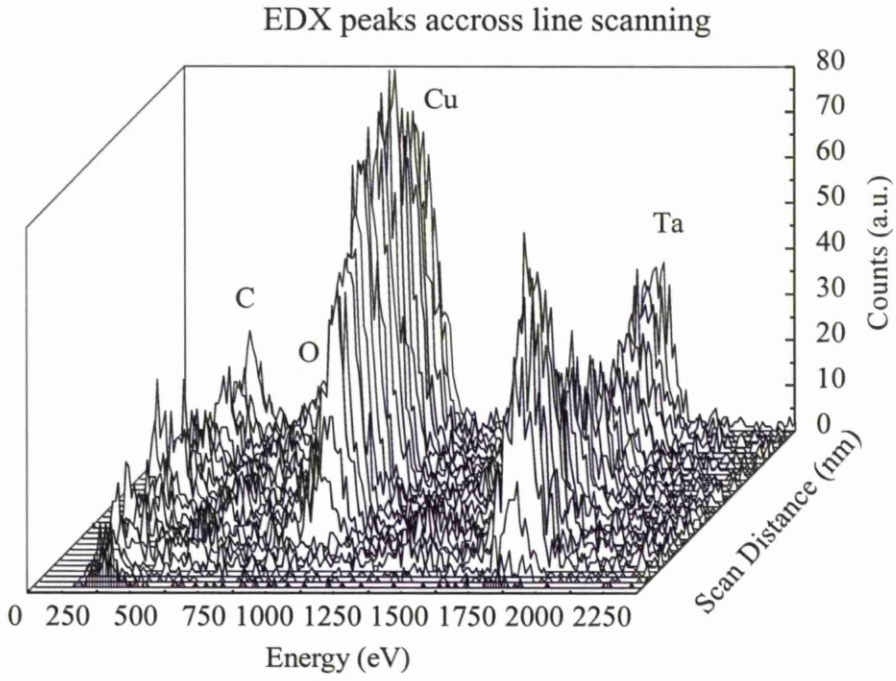


*Figure 5-16: 3D representation of EDX line scan focused at the first 2.25 KeV, where all the representative peaks of the elements are clearly shown without overlapping.*

The Ta detected while scanning along the core of the particle is to be expected since the beam passes through the whole particle, obviously detecting the Cu in the core and the Ta on the shell above and below the core. The carbon signal due to the underlying carbon layer is constant throughout the scan and so is the oxygen signal, due to the fact that the core and the shell are oxides. However, someone would expect that oxygen should provide higher signal compared to Cu and Ta lines since these particles were oxidized. The EDX-system was of the type EDAX microanalyser with a liquid nitrogen cooled Si(Li) detector shielded by a beryllium window. This system allows quantitative analysis down to atomic number Z = 11 (sodium) [12]. Low signal levels may require very long acquisition times in order to obtain good signal to noise ratios, i.e. minutes for standard EDX analysis. The atomic number of Oxygen is 16 which means that it is very close to the resolution limit of the microscope. Increased acquisition times would increase the signal level however, since the average size of the particles is 20 nm they were very sensitive to electron beam exposure. Generally, Electron Energy Loss Spectroscopy (EELS) is a good approach towards that direction because the sensitivity of EELS increases with decreasing Z number. Thus, the EDX line scan data cannot be considered trustworthy for quantitative analysis. XPS data show higher reliability as it will be demonstrated below.

Figure 5-17 shows the graphic representation of the EDX and HAADF signals during the line scan. The variation in EDX signal for Ta and Cu correlate qualitatively very well with the HAADF signal; Z-contrast between shell and core is not pronounced as demonstrated in the high resolution STEM image of Figure 5-13. The latter effect is a cumulative effect of two factors: firstly, the line scan was performed using a much bigger spot size than the HR-STEM image and secondly the acquisition time during the EDX line scan was a few seconds at every point contrary to tens of micro-seconds for the HR-STEM image. For such long acquisition times, the HAADF signal from thicker areas will increase and will not depend strongly on atomic number variation between the probed sites.

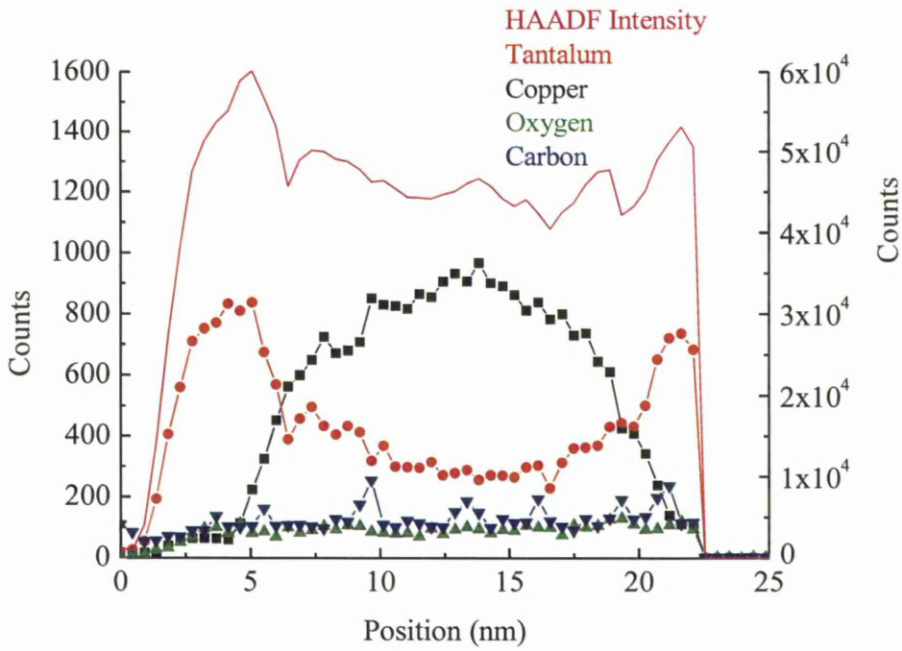


*Figure 5-17: EDX line scan atomic intensity of active elements and HAADF intensity profile throughout line scan.*

The composition of the produced material was also examined by means of EDX mapping. Figure 5-18 (a) shows low magnification STEM images depicting an agglomeration of NPs. The area was scanned for three different elements (tantalum (b), copper (c) and oxygen (d)) with the high contrast areas showing the concentration of its element. The presence of tantalum surrounds the copper core of most of the particles. Oxygen was found in all regions of the micrograph.

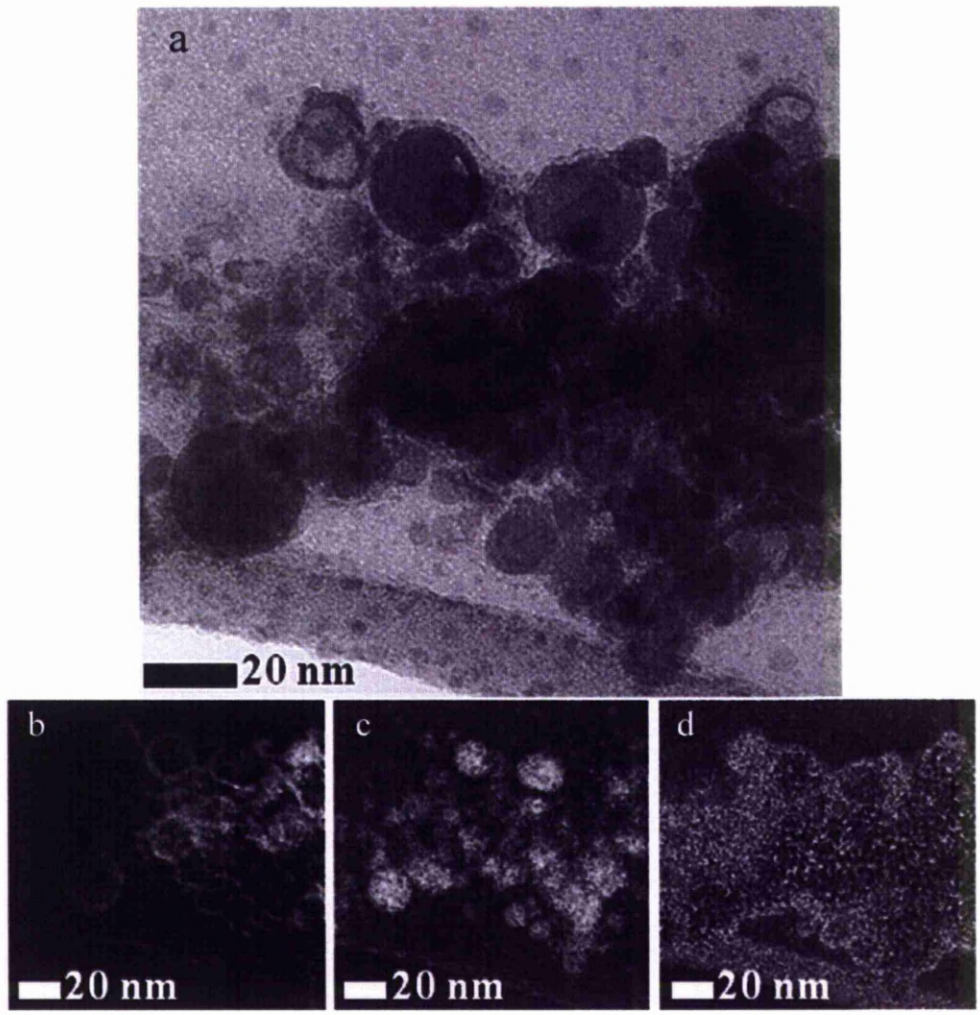


*Figure 5-18: Low magnification EDX mapping. (a) Original STEM image and separate (b) tantalum, (c) copper and (d) oxygen maps*

Higher magnification STEM, focusing in a single particle showed similar results. Figure 5-19 illustrates a STEM image of two core-shell particles. EDX mapping was applied to the left particle (~ 25 nm diameter) to investigate its chemical composition. The scanning step was 1 nm. Indeed, the dominant elements found correspond to tantalum, copper, oxygen and carbon (due to the amorphous carbon grid). The tantalum map shows significant concentration along the periphery of the NP in contrast with the Copper map which shows that Cu is localised in the core.

Oxygen is uniformly distributed along the particle proving the oxidized nature of this structure.

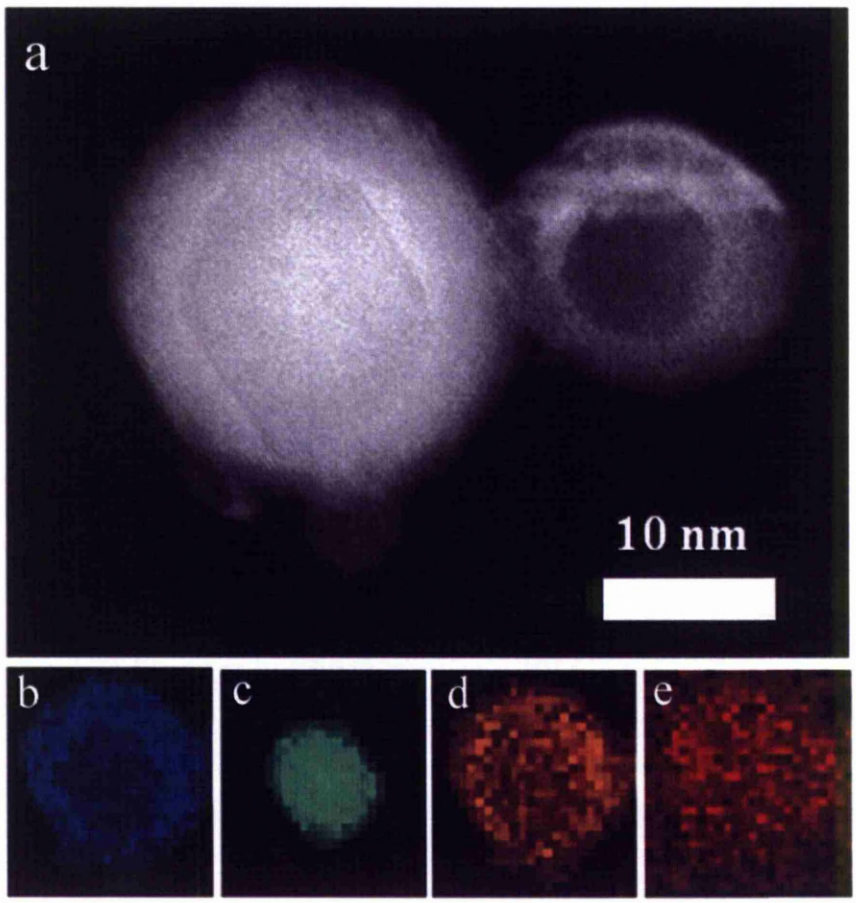


*Figure 5-19: STEM micrograph of two core-shell particles. EDX mapping on the left particle illustrating the placement of the elements (b. tantalum, c. copper, d. oxygen and e. carbon).*

### 5.4.3. X-RAY DIFFRACTION

The crystallographic identity of the nano-powder was determined by XRD examination. This method shows interesting results since this core/shell structure has never been reported in the past. The XRD spectrum of the nanoparticle powder is presented in Figure 5-20. After detailed investigation, the peaks identified in the spectrum correspond to two different materials: CuO and $Ta_2O_5$ (marked as "C" and "T" in the spectrum) further enhancing the findings of HRTEM and STEM microscopy characterization methods mentioned above. All different combinations of Cu-Ta-O chemical types were compared before reaching this conclusion but there was no match.

Comparing this graph with the pure $Ta_2O_5$ produced by the same method, the same peaks were present with additional peaks which correspond to CuO. The hypothesis of already known composite oxide in nanoparticle form was further confirmed by the XPS analysis (see section 3.3.4 below).

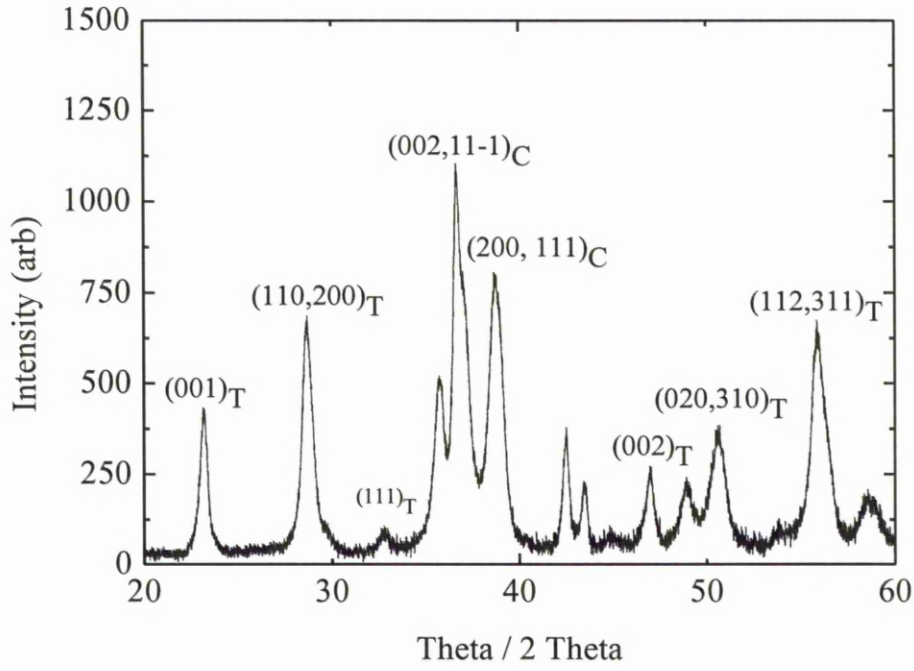


*Figure 5-20: XRD spectrum of the produced composite powder. The indentified "C" peaks correspond to CuO and the "T" peaks to $Ta_2O_5$.*

### 5.4.4. X-RAY PHOTOELECTRON SPECTROSCOPY (XPS)

The composite powder was also examined by means of XPS analysis. Figure 5-21 (a) shows the recorded spectrum at a wide scan recorder configuration from the copper/tantalum sample, where the features detected are the XPS core level peaks Ta4f, C1s, Ta4d, O1s and Cu2p as well as the x-ray induced Auger peaks Cu(LMM) and O(KVV).

The C1s peak appears to have a very low signal indicating that only traces of carbon exist on the sample's surface (Figure 5-21 (b)). The feature at binding energy (BE) 284.7 eV is attributed to residual carbon usually in the graphitic form.

The Ta4f spectrum was analyzed into two doublets [Spin orbit splitting (S.O.S) = 1.8 eV, branching ratio BR = 4:3]. The $Ta4f_{7/2}$ component of the first Ta4f doublet appears at binding energy (BE) = 25.5 eV and of the second at BE = 29.4 eV (Figure 5-21 (c)). The explanation for these binding energy values is not straightforward. The first one could originate from Ta sub-oxides but the second is too high and it can only appear when Ta is bonded to something very electronegative such as F.

Figure 5-21 (d) shows the $Cu2p_{3/2}$ core level spectrum which is analyzed into three components. The first at BE=932.6 eV is attributed to Cu atoms in the metallic state, while the second at BE = 936.8 eV corresponds to $Cu^{2+}$. Finally the third peak is an energy-loss satellite which appears always at the Cu2p spectrum of oxidized Cu.

The O1s peak is wide and has been analyzed into two components which are also wide (full width at half maximum, w = 3.9 eV) indicating that each one of them includes the contribution of more than one chemical species. The first component is at BE = 529.8 eV and includes the contribution of oxygen atoms attached to Ta or Cu or even in mixed Cu-O-Ta bonds. The second component at BE = 533.5 eV is attributed to oxygen atoms in water molecules.

Quantitative analysis was performed, using the photoelectron peak intensities, corrected by the corresponding relative sensitivity factors [13]. From the calculations of the binding energy, the intensities and the surface atomic ratios, the surface concentration of each element was: Ta: 14.3 %, Cu: 7.9 %, O: 67.4 % and C: 10%. The resultant atomic concentration is consistent CuO - $Ta_2O_5$ which is in some agreement with findings from XRD. The 10 % carbon found in the composite was all on the surface participating in C-C bonds, suggesting material contamination.

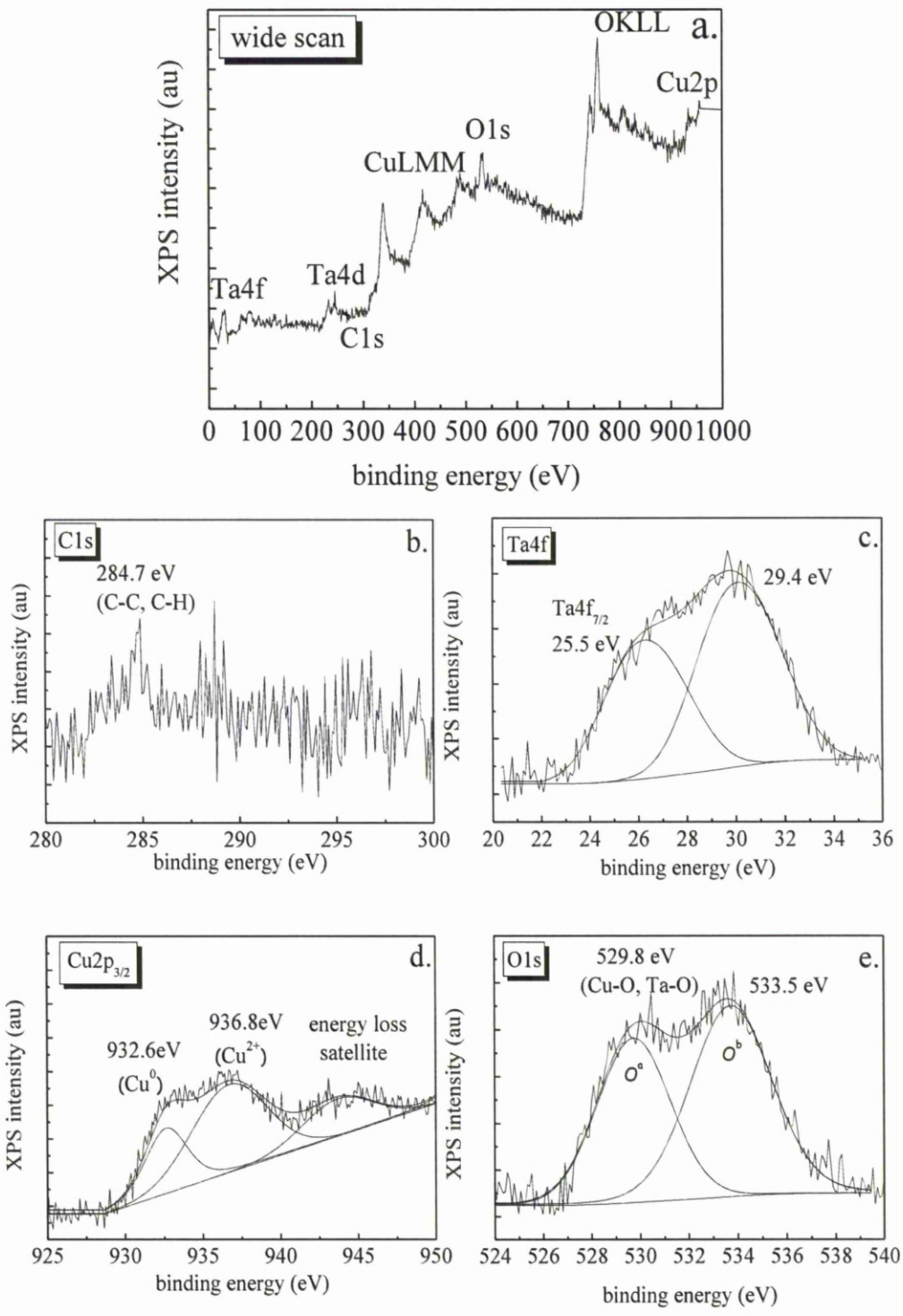


*Figure 5-21: **(a) XPS wide scan of Copper/ Tantalum nanopowder. (b) C1s core level peak.** (c) Ta4f and (d) Cu2p3/2 core level spectra. (e) O1s core level peak.*

## 5.5. PRODUCTION MECHANISM

Speculation is made here regarding the likely formation mechanism; more detailed in-situ plasma characterisation currently aims at a deeper understanding of process evolution. Arc in liquids is a widespread method for creating (mainly carbon) nanoparticles [14-25]. The leading view is that the electric arc is responsible for vaporising the anode due to the high density electron current. As this vapor is fed with more material it expands within the liquid to form a bubble. The bubble, or parts of it, eventually starts floating toward the water surface. While the bubble is inside the liquid, the vapor in touch with the liquid condenses to form nanoparticles. The use of a composite anode toward the formation of core-shell nanoparticles has so far been limited to metal-carbon composites which yield carbon encapsulated metal nanoparticles (mainly ferromagnets such as Co and Ni) [26-30]. Since these metals are known to be good catalysts for nanotube growth, the assumption was that as the metal particles are formed in the plasma, graphitic carbon forms on their surface by carbon absorption into the metal and subsequent segregation out of the metal at the surface of the particle. The formation of the intermediate carbide form ($Ni_3C$ or $Co_3C$) in vacuum arcs with composite electrodes has also been observed.

There are also reports for the formation core-shell $MoS_2$ nanoparticles [31] by arc in water, where a pure $MoS_2$ anode was used. The nanoparticles consisted of a $Mo_xS_y$ solid core and a shell adopting the characteristic fullerene-like $MoS_2$ layered structure. In this case, the core-shell formation is attributed to $MoS_2$ particle formation during the arc, according to the standard mechanism described above, with subsequent modification (melting and re-condensation) of the surface layer of the nanoparticles into the more stable fullerene-like microstructure. In the current work however the formation of CuO-$Ta_2O_5$ core-shell nanoparticles cannot be explained by adopting the formation mechanism proposed for carbon encapsulated metal or $MoS_2$ nanoparticles. On one hand, even though CuO is a known catalyst for the electrochemical decomposition of water into hydrogen, it is not known to catalyse the formation of any solid materials, let alone $Ta_2O_5$. On the other hand, unlike $MoS_2$ core-shell nanoparticles, in the CuO-$Ta_2O_5$ particles formed here the shell and core are made of different materials. Therefore, a fresh approach to the formation mechanism of core-shell particles by arc in liquids is needed; one that might also lead to reconsidering previous results.

The common factor between heterogeneous core-shell particles (carbon encapsulated metals and CuO-$Ta_2O_5$) is that the shell material has a much higher 5 melting/vapourising temperature than the core. As the arc establishes itself the composite anode evaporates much like for the high current e-beam evaporation. As the anode temperature increases, the material with the lowest melting point (Cu) starts evaporating first. As the first CuO particles start forming (dissociation of water is the source of oxygen) via vapour condensation, the high melting point material (Ta) starts evaporating from the anode. During Ta condensation into $Ta_2O_5$ the existing CuO particles act as seeds. CuO and $Ta_2O_5$ nanoparticles have been detected also, so the above process does not prohibit independent condensation of Cu and Ta, perhaps also reflecting possible composition inhomogeneities on the anode. However, the fact that the vast majority of nanoparticles are core-shell suggests that condensation of $Ta_2O_5$ around an existing nanoparticle is to a great degree preferred more than condensation into pure $Ta_2O_5$particles. In addition, if the amount of Cu in the anode is decreased, the percentage of core-shell nanoparticles decreases. This also shows that $Ta_2O_5$ will condense into pure $Ta_2O_5$ particles if there are no CuO nucleation seeds to utilize. After all, $Ta_2O_5$ dielectric nanoparticles can be produced by using a pure Ta anode [32]. Due to the complexity of the anode, apart from core-shell structures, other NP morphologies were observed such as uniformed crystalline NPs and at some extent even hollow spheres. However, the vast majority of the produced material was proven to be CuO-$Ta_2O_5$ core-shell NPs after several different characterization techniques and numerous amount of examined samples. Ways of increasing the quality of the nanoproduct are discussed in the next chapter.

## 5.6. ELECTRICAL CHARACTERIZATION OF COPPER OXIDE /TANTALUM OXIDE CORE/SHELL NANOPARTICLES

The electrical properties of the core/shell nanopowder was a significant part of this study in order to fully characterize this novel material. Broadband Dielectric Spectroscopy (DBS) was applied by measuring the frequency dependence of the complex dielectric constant $\varepsilon^*$ (where $\varepsilon^* = \varepsilon' - i\varepsilon''$) and of the loss factor $tan\delta$, (where $tan\delta = \varepsilon''/\varepsilon'$) as a function of temperature.

Core/shell powder was heated to sufficiently high temperature (~300 °C) in order to exclude any volatile contamination. It should be noted that XPS analysis revealed the presence of $H_2O$. Consequently, the powder was placed in an Alpha-N Frequency Response Analyzer in a parallel plate liquid sample cell configuration (Novocontrol BDS1308). This sample cell would apply controllable low pressure to the powder to ensure the repeatability and reliability of the measurements. Each sample was placed between two external electrodes and the powder was confined using a teflon ring with a diameter 20 mm as shown in Figure 5-22.

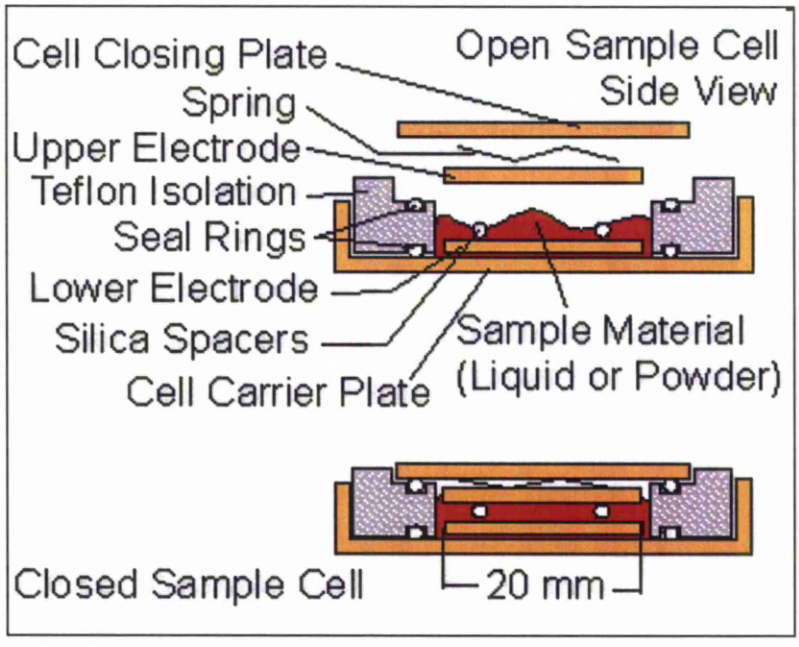


*Figure 5-22: Sample cell for powders (liquids)*

The measurements included a wide range of temperatures (-120 °C to +150 °C), with a temperature step of 10 °C and frequencies between 0.1 Hz and 1 MHz. Figure 5-23 shows the frequency dependence of the electrical permittivity for various temperatures.

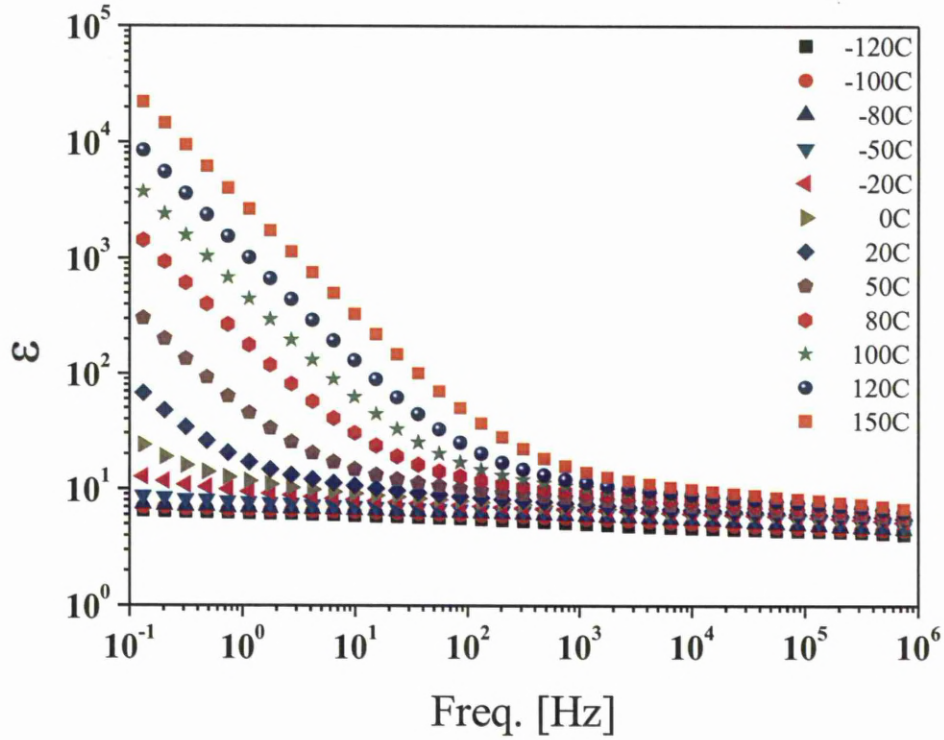


*Figure 5-23: Frequency dependence of the electrical permittivity, for CuO / $Ta_2O_5$ core shell nanopowder, in the temperature range from -120 °C to 150 °C.*

It is clear that the electrical permittivity remains almost constant (~ 10) in the low temperature region (-120 °C to 0 °C), whereas for higher temperatures an increase of the permittivity is observed at low frequencies (below 1 kHz). The tendency of the electrical permittivity to high values is attributed to the DC conductivity, which makes a contribution to the apparent dielectric loss measurements [33, 34]. As a result the abrupt increase of the permittivity should not be considered as a true dielectric response but rather as an effective one. The loss factor tanδ was also measured in the

same range of frequency and temperature (Figure 5-24). In the low temperatures region the loss factor tanδ exhibits low values (~ $10^{-2}$) indicating low energy dissipation mechanism(s). The corresponding relaxation mechanism is also discussed in Figure 5-27. At temperatures above -50 °C and in the low frequency region tanδ exhibits higher values, indicating the existence of a high dissipation energy mechanism. This mechanism must be related to the DC conductivity, present at high temperatures and low frequencies.

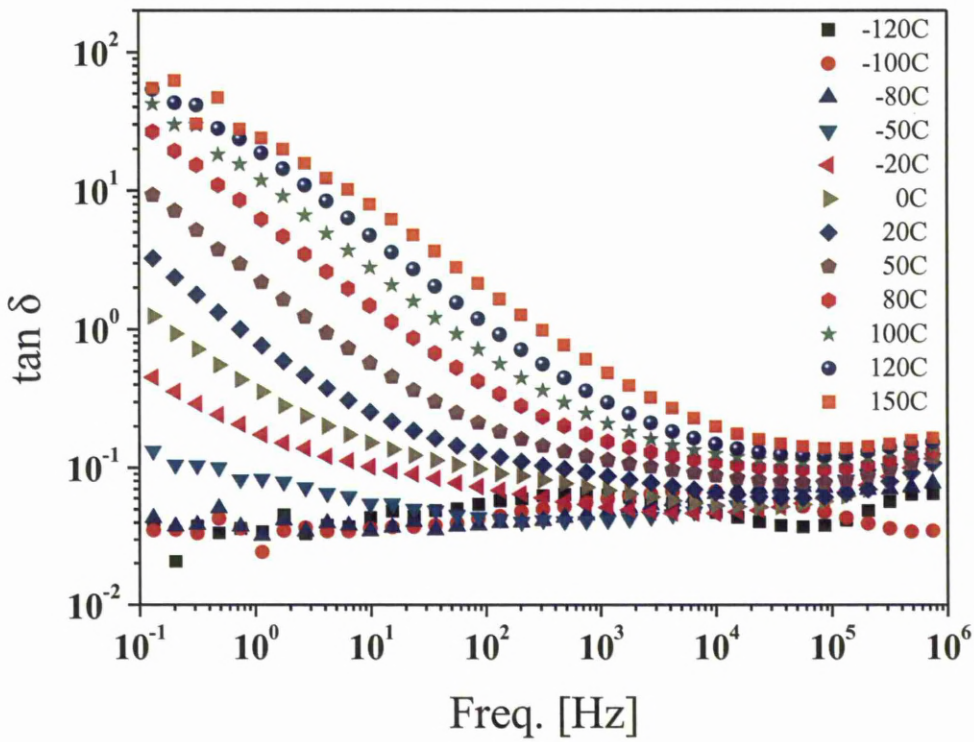


*Figure 5-24: Frequency dependence of the loss factor tanδ, for $CuO/Ta_2O_5$ core shell nanopowder, in the temperature range from -120°C to 150 °C.*

Measuring the real part of the conductivity σ′ the frequency (Figure 5-25) it is observed that in the temperature range from -10 °C to +150 °C the dependence of σ′ with frequency can be divided into two distinct regions: In the high frequency region σ′ increases with increasing frequency following the universal dielectric response law [35], $\sigma' = A\omega^n$, where $n$ is calculated to be very close to unity, in the whole frequency

range, characteristic of a capacitive behaviour. In the low frequency region the electrical conductivity exhibits a levelling off and is practically frequency independent. Thus, it can be considered as the DC conductivity of the specimen. It is obvious that the DC conductivity increases significantly with increasing temperature. At temperatures below -50 °C, σ′ exhibits a typical dielectric behavior.

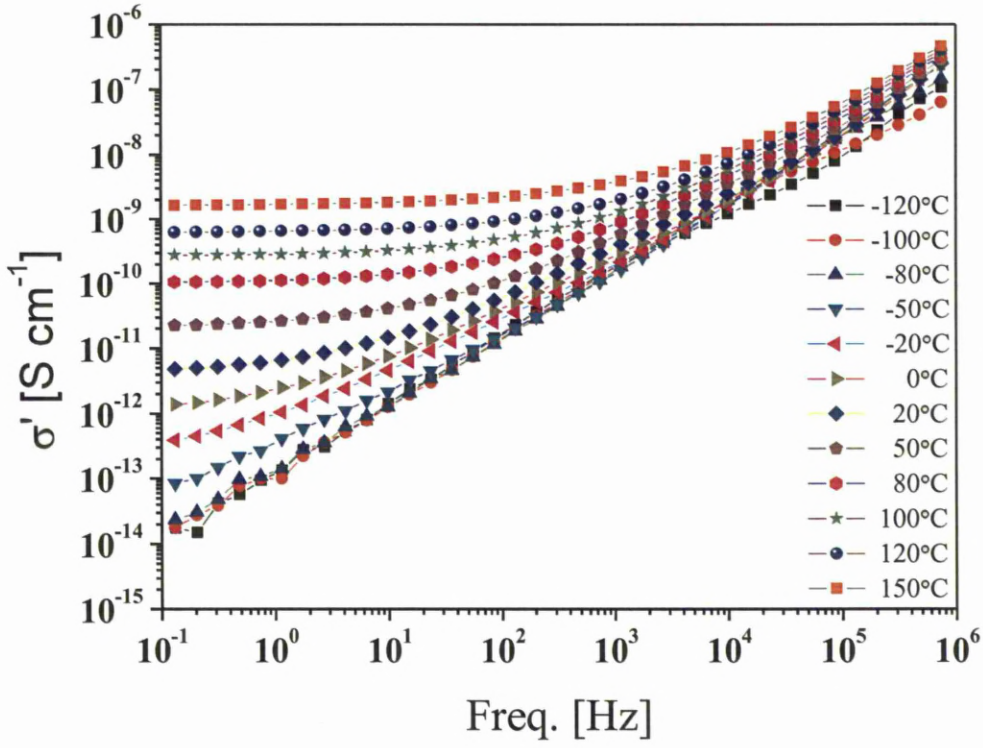


*Figure 5-25: Frequency dependence of the real part of the electrical conductivity σ′, as a function of temperature for CuO/ $Ta_2O_5$ core shell nanopowder.*

DC conductivity ($\sigma_{DC}$) values as a function of reciprocal temperature is also plotted in Figure 5-26. The activation energy can be computed following the Arrhenius equation, $\sigma_{DC}=\sigma_0 \exp(-\Delta E/kT)$, where $\sigma_0$ is a pre-exponential factor, k the Boltzmann constant, $\Delta E$ the activation energy and T the absolute temperature. The solid line presents the theoretical fitting to the Arrhenius equation and the calculated activation energy is 0.51 eV (Figure 5-26).

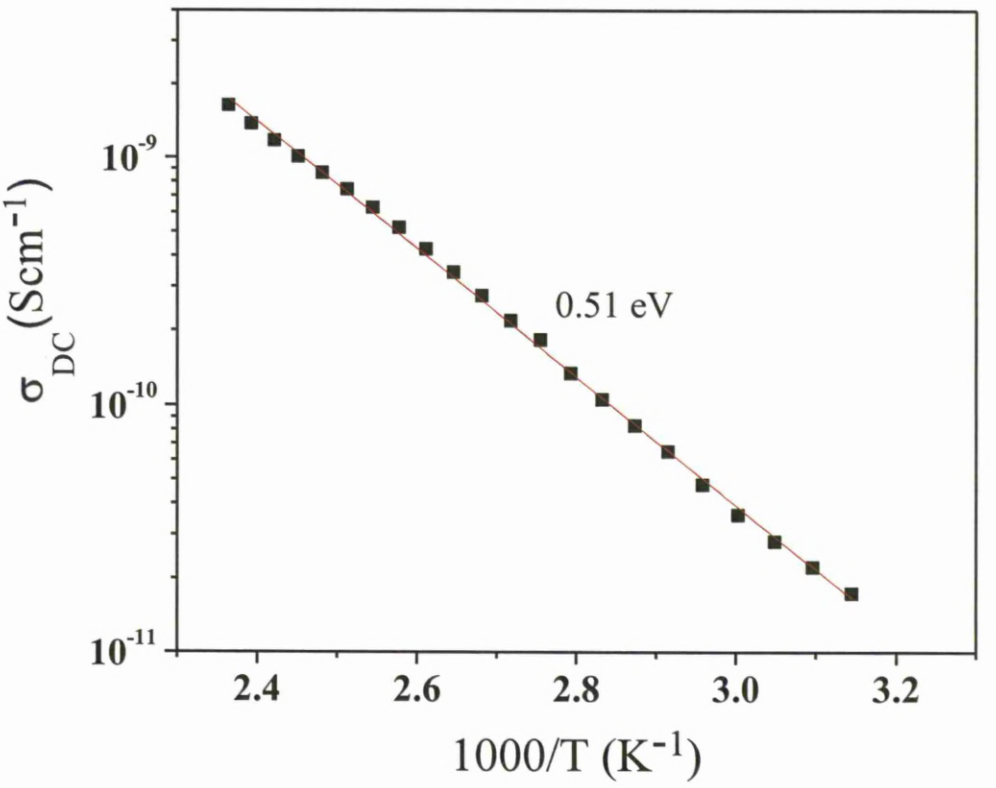


*Figure 5-26: Arrhenius plot: $\sigma_{DC}$ ($\sigma'$@ 0.1 Hz) as a function of reciprocal temperature.*

Focusing on the low temperature region (-120 °C to -80 °C), where low values of the loss factor (tanδ) are obtained, the evolution of a relaxation mechanism is also observed in the dielectric spectra (Figure 5-27). Taking into account that CuO is a wide band semiconductor and that $Ta_2O_5$ is an insulating material, the above observed relaxation mechanism should be related to the electrical heterogeneity of the nanoparticles constituents and should be considered as an interfacial polarization effect [36].

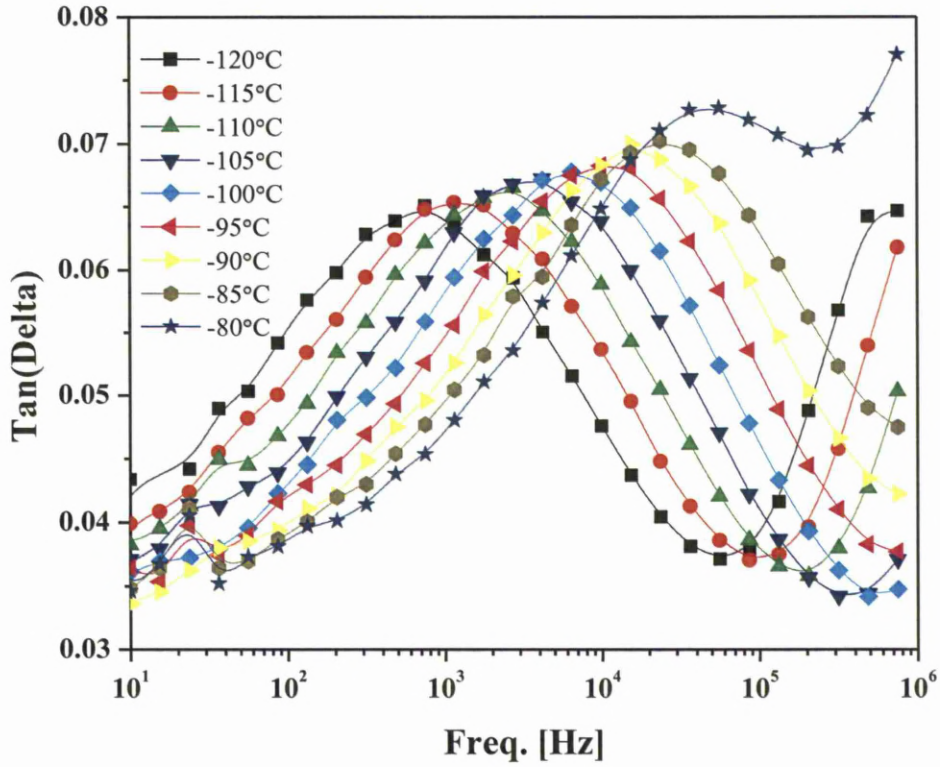


*Figure 5-27: tanδ versus frequency in the low temperature region.*

Finally, the frequency at maximum loss as a function of reciprocal temperature for the low temperature relaxation mechanism was measured (Figure 5-28). The solid line presents the theoretical fitting to the Arrhenius equation. The activation energy is evaluated through the Arrhenius equation, $f_{max}=f_0 \exp(-\Delta E/kT)$, where $f_0$ is a pre-exponential factor, k the Boltzmann constant, $\Delta E$ the activation energy and T the absolute temperature. The calculated activation energy is 0.27 eV.

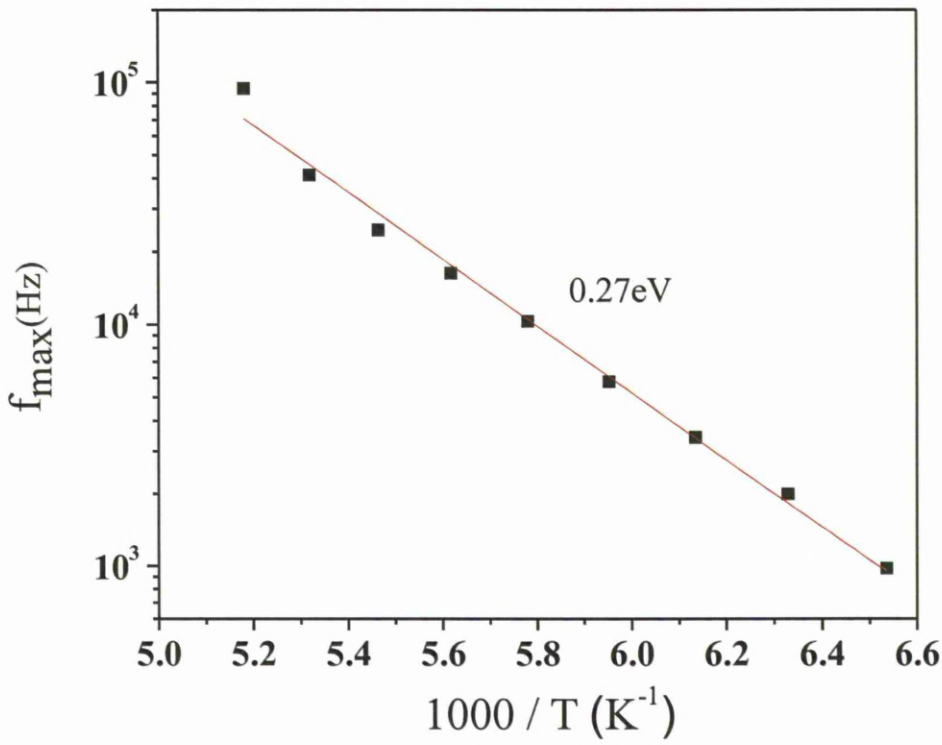


*Figure 5-28: Arrhenius plot: $f_{max}$ as a function of reciprocal temperature.*

## 5.7. SUMMARY

In conclusion, the spontaneous formation of novel core/shell nanoparticles in an immersed arc discharge has been demonstrated. Various diagnostic techniques were applied during the arc discharge to understand the production mechanism of these particles. High speed imaging has shown that the plasma behaves in a similar manner to previous experiments of arc discharges using aluminium and tantalum electrodes. The average arc time was approximately 10 seconds. OES depicted energetic species of the anode, copper and tantalum atoms, and other products like carbon, oxygen and hydrogen. Electron microscopy illustrated core/shell particles with average diameter ~ 20 nm. An EDX line scan and mapping confirmed a rich Cu

core and Ta:O shell showed the chemical composition of these particles. CuO encapsulated by a thin layer of $Ta_2O_5$ was proven to be the structure of the produced particles. XRD and XPS analysis confirmed the crystalline structure of these particles as well as binding energies which correspond to the mentioned structure. Since this material has not been reported before, the dielectric properties were studied in detail. BDS was applied in various frequency and temperature regimes showing the dielectric behaviour of the nanopowder. The measurements showed a capacitive behaviour in the low temperature range, however, significant losses appear in the low frequency and high temperature range due to DC conductivity. The powder produced is a potential applicant for devices where nano-composite dielectrics are required.

## 5.8. REFERENCES


[1] J.H. Lee, K. Koh, N. I. Lee, M. H. Cho, Y. K. Ki, J. S. Jeon, K. H. Cho, H. S. Shin, M. H. Kim, K. Fujihara, H. K. Kang, J. T. Moon, *IEDM Technical Digest. International*, 5, 645 (2000).

[2] J. Lin, N. Masaaki, A.Tsukune, M. Yamada, *Appl. Phys. Lett.* 74, 2370 (1999).

[3] M. Cernea, J. Optoelectron. Adv. M. 7, 6 (2005).

[4] B. Renner, P. Lunkenheimer, M. Schetter, A. Loidl, A. Reller, and S. G. Ebbinghaus, *J. Appl. Phys.* 96, 8 (2004).

[5] National Institute of Standards and Technology (NIST), Atomic Spectra Database.

[6] T. Nakano, N. Ohnuki and S. Baba, *Vacuum,* 59, 581 (2000).

[7] H. J. Kim, J. H. Lee, M Y. Kim, T. Cserfalvi and P. Mezei, *Spectrochimica Acta Part B*, 55, 823 (2000).

[8] Y. Ushirozawa and K. Wagatsuma, *Anal. Sci*, 22, (2006).

[9] C. G. Parigger, M. Dackman, and J. O. Hornkohl, *Appl. Opt.*, 47, G1 (2008).

[10] J. Musil, J. Matouš, and A. Rajskú, *Czech. J. Phys.*, 43, 533 (1993).

[11] R. Khalid, K. Yaqub, S. Yaseen, S. Javeed, A. Ashraf, S. A. Janjua, and S. Ahmad, *Nucl. Instrum. Methods Phys. Res. B*, 263, 497 (2007).

[12] H.J. Engelmann and E. Zschech: Proc. Int. Conf. Characterization and Metrology for ULSI
Technology, Gaithersburg USA (2001) Paper No CP550, p.491.

[13] D. Briggs and M.P. Seah (second ed.), *Practical Surface Analysis* vol. 1, Wiley, New York (1990).

[14] P. Muthakarn, N. Sano, T. Charinpanitkul, W. Tanthapanichakoon, and T. Kanki, J. *Phys. Chem. B* 110, 18299 (2006).

[15] H. W. Zhu, X. S. Li, B. Jiang, C. L. Xu, Y. F. Zhu, D. H. Wu, and X. H. Chen, *Chem. Phys. Lett.* 366, 664 (2002).

[16] I. Alexandrou, H. Wang, N. Sano, and G. A. J. Amaratunga, *J. Chem. Phys.* 120, 1055 (2004).

[17] S.-D. Wang, M.-H. Chang, K. M.-D. Lan, C.-C. Wu, J.-J. Cheng, and H.-K. Chang, *Carbon* 43, 1778 (2005).

[18] N. Sano, J. Nakano, and T. Kanki, *Carbon* 42, 667 (2004).

[19] M. Bystrzejewski, H. Lange, A. Huczko, M. Ruemmeli, T. Gemming, and T. Pichler, *Fuller. Nanotub. Car. N.* 14, 207 (2006).

[20] S. Akita, H. Ashihara, and Y. Nakayama, *Jpn. J. Appl. Phys* 39, 4939 (2000).

[21] H. Lange, M. Sioda, A. Huczko, Y. Zhu, H. W. Kroto, and D. R. M. Walton, *Carbon* 41, 1617 (2003).

[22] L. P. Bir´o, Z. E. Horv´ath, L. Szalm´as, K. Kert´esz, F. W´eber, G. Juh´asz, G. Radn´oczi, and J. Gyulai, *Chem. Phys. Lett.* 372, 399 (2003).

[23] G. Xing, S. li Jia, and Z. Q. Shi, *New. Car. Mater.* 22, 337 (2007).

[24] N. Sano, Y. Kimura, and T. Suzuki, *J. Mater. Chem.* 18, 1555 (2008).

[25] N. Sano, H. Wang, I. Alexandrou, M. Chhowalla, K. B. K. Teo, G. A. J. Amaratunga, and K. Iimura, *J. Appl. Phys.* 92, 2783 (2002).

[26] M. E. McHenry, S. A. Majetich, J. O. Artman, M. DeGraef, and S. W. Staley, *Phys. Rev. B* 49, 11358 (1994).

[27] J. Qiua, Y. Lia, Y. Wanga, Z. Zhao, Y. Zhou, and Y. Wang, *Fuel* 83, 615 (2001).

[28] Y. Saito, T. Yoshikawa, M. Okuda, N. Fujimoto, S. Yamamuro, K. Wakoh, K. Sumiyama, K. Suzuki, A. Kasuya, and Y. Nishina, *J. Appl. Phys.* 75, 134 (1994).

[29] K. H. Ang, I. Alexandrou, N. D. Mathur, G. A. J. Amaratunga, and S. Haq, *Nanotechnology* 15, 520 (2004).

[30] K. H. Ang, I. Alexandrou, N. D. Mathur, R. Lacerda, I. Y. Y. Bu, G. A. J. Amaratunga, and S. Haq, *J. Metast. Nanocryst. Mater.* 23, 87 (2005).

[31] N. Sano, H. Wang, M. Chhowalla, I. Alexandrou, G. A. J. Amaratunga, M. Naito, and T. Kanki, *Chem. Phys. Lett.,* 368, 331 (2003).

[32] D. Delaportas, P. Svarnas, and I. Alexandrou, *J. Electrochem. Soc.* (2010).

[33] A. Soulintzis, G.A. Kontos, P.K. Karahaliou, G.C. Psarras, S.N. Georga, C.A. Krontiras, *J. Polym. Sci. B-Polym. Phys.* 47, 445 (2009).

[34] G.A. Kontos, A. Soulintzis, P.K. Karahaliou, G.C. Psarras, S.N. Georga, C.A. Krontiras, M.N. Pisanias, *Express Polymer Letters* 1, 781 (2007).

[35] A.K. Jonscher, *Dielectric relaxation in solids*, Chelsea Dielectric Press (London 1983).

[36] Yuanhua Lin, Lei Jiang, Rongjuan Zhao, Gang Liu and Ce-Wen Nan, *J. Phys. D: Appl. Phys.* 38, 1615 (2005).

# 6. CONCLUSIONS AND SUGGESTIONS FOR FUTURE WORK

The similarities and differences between $Al_2O_3$, $Ta_2O_5$ and core-shell CuO-$Ta_2O_5$ NPs produced in this work are summarized and compared, not only in terms of nanoparticle characterization but also in terms of method characterization and production mechanism of each nanopowder. Approaches to improving the yield and efficiency of the fabrication process and the quality of the nanoparticles are suggested. Finally, ideas are introduced about new materials that could be created using the technique of arc-discharge in water, for use in electronic applications.

## 6.1. ARC-DISCHARGE IN WATER METHOD

In previous chapters, the arc-discharge technique was applied using anode materials chosen for the formation of specific metal oxide nanoparticles. Aluminium, a well known material for its oxidization properties was firstly used to test if the product of the arc discharge results in native oxide nanoparticles. An aluminium rod was used as an anode and a carbon rod as a cathode. Both electrodes were immersed in a three litre beaker filled with de-ionized water. The discharge was produced by bringing the electrodes into contact using a manual 2D translation and the discharge was fed by a DC power supply.

Three different current densities were tested, 15 A, 35 A and 60 A. TEM examination showed that in all cases nanoparticles were formed. However, 15 A current density was very low and it was difficult to hold the discharge stable for a significant amount of time, more than 1-2 s, resulting in the need of continuous manual electrode adjustment. Moreover, TEM micrographs showed that the particles were not well defined since the presence of amorphous aluminium blending with the particles was very common. On the other hand, when the current was increased to 60 A the intensity of the plasma caused serious damage to the anode electrode, detaching large pieces that ultimately fell to the bottom of the glass beaker. Because of the high intensity of the discharge, the particle size distribution showed a wide range. This can be explained since the anode, apart from being evaporated, was breaking in

milli/micrometer sized pieces and not following the regular metal oxide nanoparticle production mechanism that has been described previously. Low magnification TEM imaging showed that 35 A current produced spherical crystalline particles with an average diameter of 40 nm. Additionally, the average self-sustained arc-time was longer, approximately 8-10 s, compared to 15 and 60 A. Finally, anode mass reduction rate measurements showed the highest production rate at 35 A.

Optical Emission Spectra were recorded in-situ from 200-850 nm wavelength ranges, further justifying the presence of $Al_I$, due to evaporation of the anode, $C_2$, due mainly to emission from the hot cathode and trace evaporation of it, $O_I$, and H arising from electrolysis of the water. The densities of these products varied significantly in every arc discharge so the process was reproducable. The vapours emitting from plasma, created during the process escaped to the water surface as bubbles. Several arc-runs were captured by high speed imaging from the ignition till the extinction, with a frame rate of 125 fps, illustrating its dynamic and unstable character. Plasma propagation and hydrodynamic phenomena in the surrounding liquid were observed.

After a few arc-runs the glass container was filled with suspended particles. The particle cloud covers the upper half of the water volume. The NP/water mixture was de-canned to another glass beaker and the product was heated at ~ 100 °C to evaporate the water. The particles were then collected in powder form.

Structural analysis from HRTEM images, using FFTs to derive the DDPs of particles, XRD as well as XPS spectra, revealed that the material produced was $Al_2O_3$. Crystallographic as well as chemical data derived from these techniques proved the presence of high purity, over 92 %, gamma phase alumina.

Since arc discharge in water using an aluminium rod led to $Al_2O_3$ NPs, the question was whether other metals would respond in the same manner to form metal oxide NPs. Tantalum pentoxide is a well known dielectric material with a relative permittivity of ~ 25, compared to 10 for aluminium oxide. The melting point between these two metals differs significantly, Ta = 3017 °C and Al = 660 °C. However, the localized temperatures within the plasma are considered to be much higher, so tantalum was expected to be evaporated.

The experimental set-up was the same as in the previous experiment, in order to compare both procedures. Similar conclusions were derived for the optimum current density of the plasma. Low magnification TEM revealed that particles at 35 A

had uniform shape and a narrow size distribution, in contrast with the product of the process with arc current of 15 or 60 A. It is worth mentioning that the arc, when using a tantalum rod, was self-sustained for up to 5 minutes; compared to ~10 s when the aluminium anode was used. This better structural integrity of the Ta helped make the arc self-sustainable for longer periods, presumably due to the higher melting point of Ta compared to Al. No manual adjustment was needed after the initial contact of electrodes and the discharge stopped only due to the electrode gap increasing to a few mm. After the extinction of each discharge the only manual adjustment required was to bring the tantalum rod in contact with the carbon rod. This allowed a continuous process until the full evaporation of the anode. In the case of the aluminum rod, the surface of the anode, after a few arc-runs, showed serious deformation and an oxidized layer was deposited on it, forbidding the current to pass through the electrodes. Consequently, this layer needed to be removed from the anode in order to start the discharge again, a fact which rendered the procedure time-consuming and consequently unsuitable for industrial production.

OES was applied for species identification; tantalum, carbon, oxygen and hydrogen were found to have been created during the plasma plasma. Hence, water molecules were split feeding the vapour with oxygen and hydrogen. High speed imaging showed that gas bubbles were continuously formed and escaped towards the water surface. The tantalum arc behaved in a similar manner to the aluminium arc.

High-resolution TEM showed that the nano-product was formed of crystalline spherical particles with diameters ranging from 5-100 nm and a mean average size of 40 nm. The DDPs derived from the TEM micrographs were compared with crystallographic databases and matched with the $Ta_2O_5$ structure. The X-ray diffraction spectrum was nicely matched with a room temperature stable phase of tantalum pentoxide commonly referred to as "*L-$Ta_2O_5$*". The XPS analysis detected tantalum and oxygen peaks at characteristic energies for $TaO_x$ bonding. Carbon traces were found in a ~ 10 % atomic concentration however, they can be attributed to post-fabrication contamination since there was no carbon or other impurities introduced to the chemical structure of the particles.

Comparing the electrode mass reduction rate between the aluminium and tantalum arc, the cathode remains almost constant depending only on the current density and not on the anode electrode. An oxidized layer formed gradually on the

aluminium electrode surface during the life of the plasma is proposed to be the reason why Ta shows a higher rate; 4.7 and 1 mgr/s for tantalum and aluminium at 35 A, respectively. The carbon electrode was observed to be macroscopically unaffected except for deposition of Al or Ta on its surface due to welding. It is the latter that adds to the mass of the cathode and thus the negative reduction rate. The anode mass reduction rate versus the current increases exponentially, however, the tantalum arc showed higher rate, presumably due to its stabilized nature. These measurements suggest an anodic arc-discharge.

The experiments using aluminium and tantalum anode proved that arc-discharge in water method is a cost-efficient and relatively simple way of producing high-purity, crystalline, metal oxide, high-*k* dielectric nanoparticles. However, single-metal oxides cannot show dielectric constants much higher than the one of tantalum pentoxide. Several composite metal oxides have been reported recently with dielectric constants of a few hundreds or even thousands. Taking into account the reported work so far, copper and tantalum powder grains were mixed and compressed to form a tablet and used as an anode in the arc-discharge in water process. $Cu_2Ta_4O_{12}$ is known to have a dielectric constant that reaches values of ~ 10000 at frequencies below 5 MHz [1]. The motivation for choosing these two materials stems from two facts. First of all, this is a material that has shown promise in recent studies, but has not attracted too much attention from the industry and secondly, the detailed studies on the tantalum arc, provided evidence for the feasibility of the process and hence motivation for investigating other metals.

High-purity powder grains, 1-5 μm in diameter, were mixed in a wt = 66.6 % Ta and placed in a U-shaped stainless steel holder. The mixture was compressed into a solid tablet at 100 kN (~ $3.5 \times 10^7$ $N/m^2$) using a mechanical press. The metal holder with its content was used as the anode and a carbon rod as a cathode to create plasma by bringing the electrodes in contact in a de-ionized water environment. The current generator was set at value of 15 A, 35 A, and 60 A to test which current density is the most appropriate for this particular set up. 15 A was not intense enough to create continuous plasma and 60 A was too intense resulting in severe damage to the anode surface. The 35 A current level shoed the creation of discharges with an average lifetime of 8-10 s, without breaking the tablet. Electrical characterization of the arc discharge showed that the current remained almost constant though out its duration.

Low magnification TEM examination revealed particles with an average size of 20 nm with a anomalus structure. The NPs appeared to have different contrast between the core and the shell suggesting either a core-shell or hollow sphere structure. HRTEM and HAADF imaging illustrated crystalline structure in both core and shell proving the core-shell nature of these nanoparticles. Additionally, the shell showed stronger HAADF contrast. It should be noted that the contrast in HAADF images depends on the element size. The higher the atomic number of an element the brighter the contrast it reflects on an image. Tantalum is heavier than copper, atomic numbers 73 and 29 respectively, so an assumption that the shell mainly consists of tantalum and the core of copper was made.

To further justify this assumption EDX element maps and line scans were applied in single particles. The results showed that tantalum appears only in the outer layer of the particles whereas copper in the inner part. Oxygen was detected in all the volume of the particles suggesting that both metals were oxidized.

XPS wide scan detected core level peaks of Ta4f, C1s, Ta4d, O1s and Cu2p, as well as the X-ray induced Auger peaks Cu(LMM) and O(KVV). Once again, it was found that the NPs predominantly consist of Cu, O, and Ta. Quantitative analyses were performed using the photoelectron peak intensities corrected by the corresponding relative sensitivity factors [2]. The surface atomic ratios were estimated by probing powder from many batches and they are equal to (ratio uncertainty for each batch 5%): Ta/Cu=1.8-2.35, O/Cu=6.7-8.5, O/Ta=2.85-4.7, C/Ta=0.72-1.26. Carbon was present usually in the graphite form and should be attributed to the unavoidable surface contamination of the sample under test. The XRD pattern from the specimen was identified as a superposition of crystalline CuO [3] and $Ta_2O_5$ [4]. This atomic ratio O:Ta:Cu = 6:2:1 agreed quite well with the findings suggested by XPS. Thus, the combined results led to the identification of the novel material, that is a powder of $CuO/Ta_2O_5$ core/shell NPs.

Broadband dielectric spectroscopy was finally employed to complete the classification of this new nanopowder. The powder was placed between 20 mm diameter metal electrodes and the same pressure was applied in all the measurements. The frequency dependence of the complex dielectric constant as well as the real part of the electrical conductivity and the loss factor were measured to derive the dielectric behavior of the nano-composite powder. The measurements were conducted over the

temperatures ranges from -120 to +150 °C, for a frequency range between 0.1 Hz – 1MHz. The results shown that the electrical permittivity remains almost constant in the low temperature region, with a dielectric constant ~ 10, whereas for temperatures greater than 0°C and low frequencies, below 1 kHz, the apparent permittivity increased rapidly, probably due to DC leakage. Studying the loss factor results, several low energy dissipation mechanisms were observed, presumably due to the fact that CuO is a wide band semiconductor and $Ta_2O_5$ is an insulating material. The relaxation mechanisms are related to the electrical heterogeneity of the nanoparticles constituents and should be considered as an interfacial polarization effect [5].

## 6.2. SUGGESTIONS FOR FUTURE WORK

The work in this thesis indicates that the technique of arc discharge in water is an effective method to produce metal oxides with useful dielectric properties. However, adjustments and modifications to the experimental set up could be introduced to increase both the production rate as well as the quality of the product.

In order to render this method attractive for the industry, an automated electronic control system can be added. As described in previous sections, during arc discharge a very bright light is always present. This light was recorded by a photomultiplier (PMT), pointing in the core of the plasma, to study the plasma behaviour. Experiments have shown that by monitoring the light intensity, the user knows when the discharge occurs. A simple electronic circuit could be designed using a stepper-motor, connected to the 2D translator, to lower the electrode a few millimeters every time the light becomes lower than a preset value. Thus, the discharge can be made continuous without any need for manual adjustment. Alternatively, instead of a PMT, current or voltage measurements can be used to serve the same purpose.

This idea presupposes that there is no oxidised layer formed in the anode surface so that manual electrode cleaning is not required. A prime candidate for this application would be Ta anode where the arc-duration lasts minutes and no layer is formed. A combination of recorded voltage/current along with light intensity would provide higher security in this procedure.

Additionally, a water cooling system could be added to lower the water temperature. After several arc-runs, the temperature of the surrounding water increases because of the plasma energy, dissipated during the arc. While this is happening, it is necessary to change the water in order to maintain room temperature operation and so avoid any damage to the water tank. A cooling system would enable the arc to run without changing the water. Moreover, a cooler environment, theoretically, causes more rapid quenching.

A nanoparticle production-collection system can also be easily incorporated. The water beaker can be connected to another tank through a pipe. Taking into account that the particles are floating in the upper half of the water tank, the pipe should be connected a few centimeters below the water surface. During discharge, a valve would be open to allow the water, along with the produced nanoparticles, to flow to the second tank. The second tank could be seated on a hotplate to allow evaporation of the water and to collect the nano-powder without interrupting the process. In this case, another tank would be needed to keep the water level constant in the original beaker. Re-filling with water would also serve as an indirect cooling process.

In terms of material purification, acid washing followed by high-temperature hydrogen treatment has proven to remove any amorphous carbon surrounding the particles and metals where present [6]. In the case of metal oxide dielectric materials this is very important. If small anode fragments are added in the nano-powder product then the dielectric properties of the material will be influenced significantly in a negative way because of the conductive paths introduced within the powder.

Finally, this work has shown that new, interesting structures can be fabricated using the arc discharge in water method. The formation of core/shell $Ta_2O_5$/CuO nanoparticles proves the fact that various metals can be blended together with oxygen to create metal oxide particles. This conclusion gives rise to new experiments with metals like barium, strontium or titanium aiming to the formation of composite metal oxides such a $BaTiO_3$ and $SrTiO_3$, with known dielectric constants of ~ 1300 and ~ 300 respectively. For instance, barium and titanium have significantly lower melting point difference, 727 °C and 1668 °C respectively, than tantalum and copper. It would be interesting to see how these metals respond to plasma.

Arc-discharge in water has proven to be a method that exploits very efficiently physical processes to produce metal oxides. Equipment as well as consumables of low cost is considered to be an asset not only for industrial use, but also for academic experimental purposes.

## 6.3. REFERENCES

[1] B. Renner, P. Lunkenheimer, M. Schetter, A. Loidl, A. Reller, and S. G. Ebbinghaus, *J. Appl. Phys.* 96, 8 (2004).

[2] D. Briggs and M. P. Seah, *Practical Surface Analysis*, 2nd Ed., Wiley, New York.,1, (1990).

[3] A. Stergiou, I. Kerasiotis, C. Stergiou, *J. Optoelectron. Adv. Mater.* 9, 1772 (2007).

[4] K. Lehovec, *J. Less-Common Met.*,7, 397 (1964).

[5] Y. Lin, L. Jiang, R. Zhao, G. Liu and C. -W. Nan, *J. Phys. D: Appl. Phys.* 38, 1615 (2005).

[6] S. R. C. Vivekchand, A. Govindaraj, Md. Motin Seikh, and C. N. R. Rao, *J. Phys. Chem. B*, 108, 6935 (2004).

# 7. APPENDIX

Below, the operation of a home-made electronic circuit is described which was built in order to synchronize the in-situ measurements of the arc discharge in water.

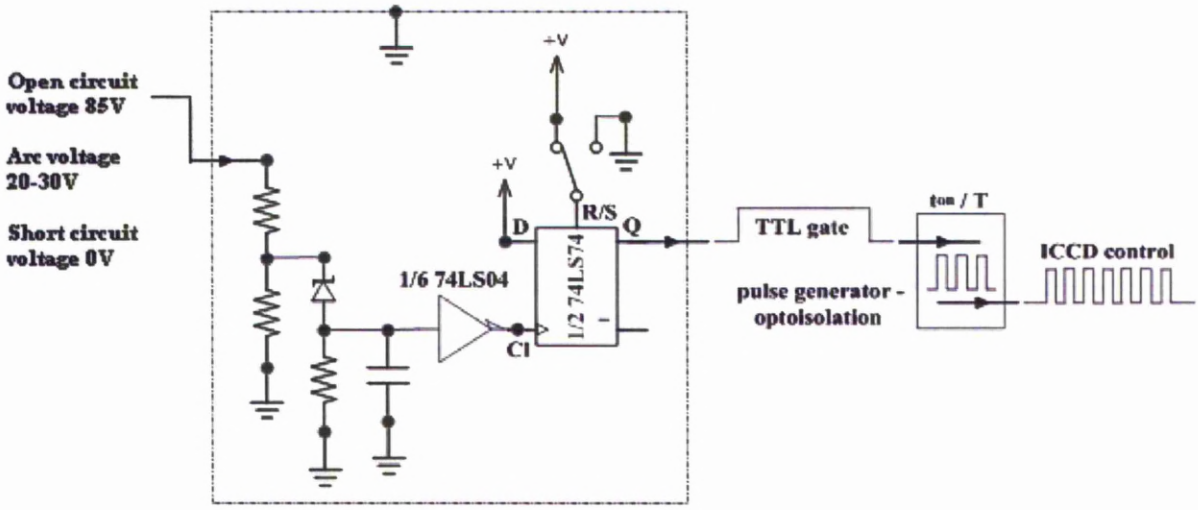


The open-circuit voltage of the high current power supply that delivers energy to the arc is about +85 V. When the two electrodes are brought into contact manually, the electrical arc is ignited and a sudden voltage drop takes place from +85 V to a much lower voltage, typically ~ 20 V (arc voltage, see arc electrical signals). This basic electronic circuit is triggered by the negative-edge slope of this "pulse" and controls the output of the pulse generator unit. Briefly:

The arc voltage is divided to a lower level by the resistive probe formed by the two left resistors. The two resistors (1 KOhm) are selected so that the +85 V are divided to a voltage approximately 2-3 V higher than the zener diode nominal voltage, i.e. ~ 6 V. Thus, the diode is initially conducting and the 74ls04 input is brought at the logic level "1" (~ 1.5-5 V). The current through the diode is limited by the small value resistor connected in series with the diode. The Clock of the 74ls74 IC is at the low level "0" due to the inverter 74ls04. For the 74ls74 IC, information on the data input is transferred to the Q output on the low-to-high transition of the Clock pulse.

Consequently, when the arc voltage falls, the voltage across the zener diode is not sufficient to make this conductive. The input of the 74ls04 passes thus to the low-logic level "0" (ground) and the 74ls74 is triggered by the positive edge of the pulse created on the Clock input. The flip-flop is set and a TTL gate Q opens and controls the output of the optoisolated pulse generator. Pulses at the pre-selected frequency/period drive the ICCD as far as the gate remains at the high level. The gate closes by the user from the switch R/S when the arc is extinguished.

The ICCD software is programmed to provide an OES spectrum file corresponding to each triggering pulse. As reference is used the first file and all the next files are acquired with a time difference of T (preselected). The time-resolved pattern is produced by plotting the OES files (OES intensity vs wavelength) with a time distance T. Similarly for the fast photography technique.